

A Snowball in Hell: The Potential Steam Atmosphere of TOI-1266c

C. E. HARMAN ¹, RAVI KUMAR KOPPARAPU ², GUÐMUNDUR STEFÁNSSON ^{3,4}, ANDREA S.J. LIN ^{5,6},
SUVRATH MAHADEVAN ^{5,6}, CHRISTINA HEDGES ^{7,8} AND NATASHA E. BATALHA ¹

¹Planetary Systems Branch, Space Science and Astrobiology Division, NASA Ames Research Center, Moffett Field, CA 94035, USA

²Planetary Environments Laboratory, NASA Goddard Space Flight Center, Greenbelt, MD 20771, USA

³Princeton University, Princeton, NJ 08540, USA

⁴Henry Norris Russell Fellow

⁵Department of Astronomy & Astrophysics, The Pennsylvania State University, University Park, PA 16802, USA

⁶Center for Exoplanets and Habitable Worlds, The Pennsylvania State University, University Park, PA 16802, USA

⁷Bay Area Environmental Research Institute, Moffett Field, CA 94035, USA

⁸Astrophysics Branch, Space Science and Astrobiology Division, NASA Ames Research Center, Moffett Field, CA 94035, USA

(Received June 18, 2021; Revised September 13, 2021)

Submitted to PSJ

ABSTRACT

TOI-1266c is a recently discovered super-Venus in the radius valley orbiting an early M dwarf. However, its notional bulk density ($\sim 2.2 \text{ g cm}^{-3}$) is consistent with a large volatile fraction, suggesting that it might have volatile reservoirs that have survived billions of years at more than twice the Earth's insolation. On the other hand, the upper mass limit paints a picture of a cool super Mercury dominated by $>50\%$ iron core ($\sim 9.2 \text{ g cm}^{-3}$) that has tiptoed up to the collisional stripping limit and into the radius gap. Here, we examine several hypothetical states for TOI-1266c using a combination of new and updated open-source atmospheric escape, radiative-convective, and photochemical models. We find that water-rich atmospheres with trace amounts of H_2 and CO_2 are potentially detectable ($\text{SNR} > \sim 5$) in less than 20 hours of JWST observing time. We also find that water vapor spectral features are not substantially impacted by the presence of high-altitude water or ice clouds due the presence of a significant amount of water above the cloud-deck, although further work with self-consistent cloud models is needed. Regardless of its mass, however, TOI-1266c represents a unique proving ground for several hypotheses related to the evolution of sub-Neptunes and Venus-like worlds, particularly those near the radius valley.

Keywords: Exoplanet atmospheres (487), Hot Neptunes (754), Extrasolar ice giants (2024), Extrasolar rocky planets (511), Exoplanets (498), Star-planet interactions (2177), Super Earths (1655), Exoplanet atmospheric composition (2021)

1. INTRODUCTION

The list of exoplanet detections from space-based observatories like the Kepler Space Telescope (e.g., Borucki et al. 2010; Twicken et al. 2016) and the Transiting Exoplanet Survey Satellite (TESS; Ricker et al. 2014; Barclay et al. 2018), as well as ground-based endeavors such as WASP (e.g. Pollacco et al. 2006), HATNet (e.g.

Bakos et al. 2004; Hellier et al. 2012), TRAPPIST (Jehin et al. 2011; Gillon et al. 2017; Delrez et al. 2018), and the Habitable-zone Planet Finder (HPF) Spectrograph (Mahadevan et al. 2012, 2014), is rapidly growing. These detections enhance our understanding of planetary occurrence rates (Batalha 2014) as well as enable robust statistical insights into planet populations (e.g., Dressing & Charbonneau 2013; Burke et al. 2015; Fulton et al. 2017; Hardegree-Ullman et al. 2019). In particular, the presence of a gap in the radius distribution of planets (Rogers 2015; Fulton et al. 2017; Fulton & Petigura 2018) highlights the cumulative effects of a

planet’s host star (e.g., Owen & Jackson 2012; Owen & Wu 2017), formation (e.g., Lee et al. 2014; Lee & Chiang 2016; Ginzburg et al. 2018; Gupta & Schlichting 2020), and/or evolution (e.g., Luger et al. 2015), although disentangling these effects will likely require more sensitive observations (Lloyd et al. 2020).

The recent discovery of two planets orbiting TOI-1266 (Stefansson et al. 2020; Demory et al. 2020) offers a rare opportunity to begin connecting some of these planetary processes through observations. The outer planet, c ($1.673 R_{\oplus}$) is smaller than the inner planet, b ($2.458 R_{\oplus}$) (see Table 1 for the reported uncertainties and a comparison between the Stefansson et al. and Demory et al. values). This puts TOI-1266c in the ‘radius valley’ (Fulton et al. 2017; Fulton & Petigura 2018). This type of ‘straddler’ planetary system (Owen & Campos Estrada 2020) can be leveraged to constrain the temporal evolution of host star’s EUV flux. However, the fact that the smaller planet is outside of the larger one (Weiss et al. 2018) hints at significant migration that may defeat first-order attempts to reproduce their present-day bulk compositions through atmospheric escape alone (Bean et al. 2021).

The bulk composition of TOI-1266c is poorly constrained because the mass measurement has large $1\text{-}\sigma$ uncertainties: $1.9^{+2.3}_{-1.3} M_{\oplus}$ from Stefansson et al. using radial velocity constraints, and $2.2^{+2.0}_{-1.7} M_{\oplus}$ from Demory et al. based on an analysis of the transit timing variations. This broad range of possible planet masses covers several different planet types including both rocky terrestrials and gas-dominated sub-Neptunes. Currently, compositional constraints are insufficient to rule out significant volatile inventories for small exoplanets under even higher instellation than what planet c receives (Dai et al. 2019). Formation models suggest that sub-Neptunes/super-Earths like TOI-1266b and c can end up as part of distinct water- or silicate-rich populations if planet embryos aggregate material from a more well-sampled protoplanetary disk (e.g. Liu et al. 2019). It may also be easier to form volatile-rich mini-Neptunes if additional gas sources, such as envelope enrichment sourced from various accreted ices, are considered (e.g. Venturini & Helled 2017). Taken together, TOI-1266c could be a rare example of a volatile-rich super-Earth, contrasting with the more well-populated family of volatile-poor, rocky super-Earths such as LHS 3844b (Kane et al. 2020) and TOI-849b (Armstrong et al. 2020).

In this paper, we explore the potential states of the planet by focusing on the H-C-O chemistry of three families of scenarios, all dominated by water: $\text{H}_2+\text{H}_2\text{O}$, $\text{H}_2+\text{CO}_2+\text{H}_2\text{O}$, and $\text{O}_2+\text{H}_2\text{O}$. This encompasses two

Property	Stefansson et al.	Demory et al.
TOI-1266:		
Spectral type	M2	M3
Mass [M_{\odot}]	0.437 ± 0.021	0.45 ± 0.03
Radius [R_{\odot}]	$0.4232^{+0.0077}_{-0.0079}$	0.42 ± 0.02
Temperature [K]	3563 ± 77	3600 ± 150
Age [Gyr]	$7.9^{+4.2}_{-5.2}$	~ 5
Luminosity [L_{\odot}]	$0.02629^{+0.00071}_{-0.00075}$	—
Planet b:		
Mass [M_{\oplus}]	$6.9^{+5.5}_{-4.0}$	$13.5^{+11.0}_{-9.0}$
Radius [R_{\oplus}]	$2.458^{+0.083}_{-0.073}$	$2.37^{+0.16}_{-0.12}$
Semi-major axis [au]	$0.0745^{+0.0046}_{-0.0069}$	$0.0736^{+0.0016}_{-0.0017}$
Instellation [S_{\oplus}]	$4.72^{+1.0}_{-0.66}$	$4.9^{+1.0}_{-0.8}$
Equilibrium temp.* [K]	$410.0^{+21.0}_{-15.0}$	413 ± 20
Planet c:		
Mass [M_{\oplus}]	$1.9^{+2.3}_{-1.3}$	$2.2^{+2.0}_{-1.5}$
Radius [R_{\oplus}]	$1.673^{+0.087}_{-0.110}$	$1.56^{+0.15}_{-0.13}$
Semi-major axis [au]	$0.1037^{+0.0026}_{-0.0025}$	$0.1058^{+0.0023}_{-0.0024}$
Instellation [S_{\oplus}]	$2.42^{+0.23}_{-0.22}$	$2.3^{+0.5}_{-0.4}$
Equilibrium temp.* [K]	$347.1^{+7.9}_{-8.0}$	344 ± 16

Table 1. We use the Stefansson et al. stellar and planetary parameters as the default in this study, and include values for planet b. The planet mass is reported with the $1\text{-}\sigma$ error. Equilibrium temperature is calculated assuming an albedo of 0. We also include the values reported by Demory et al. (2020) for reference, which agree within error.

potential intermediate states (as we describe below) as well as a hypothetical super-Venus transitional state, in which CO_2 begins to represent a significant portion of the envelope mass. We omit two other classes of atmospheres (Venus-like and sub-Neptune) for the sake of brevity. Simulations of exo-Venus atmospheres (Schaefer & Fegley Jr 2011; Lincowski et al. 2018; Lustig-Yaeger et al. 2019a) largely resemble Venus’ CO_2 -dominated atmosphere at present or with smaller CO_2 inventories earlier in its history (e.g. Way & Del Genio 2020). For exo-Venuses in particular, more exploration is warranted to cover the expected diversity of planetary conditions and composition (see the review by Madhusudhan et al. 2016). A number of studies on the diversity of sub-Neptune atmospheres (e.g., Lavvas et al. 2019; Chouqar et al. 2020) and retrievals (e.g., Benneke et al. 2019; Mikal-Evans et al. 2020) can be found in the literature; see also the review by Bean et al. (2021).

1.1. Motivating the ‘snowball’ scenario

The current mass of TOI-1266c affords a variety of different possible compositions that largely fork into two

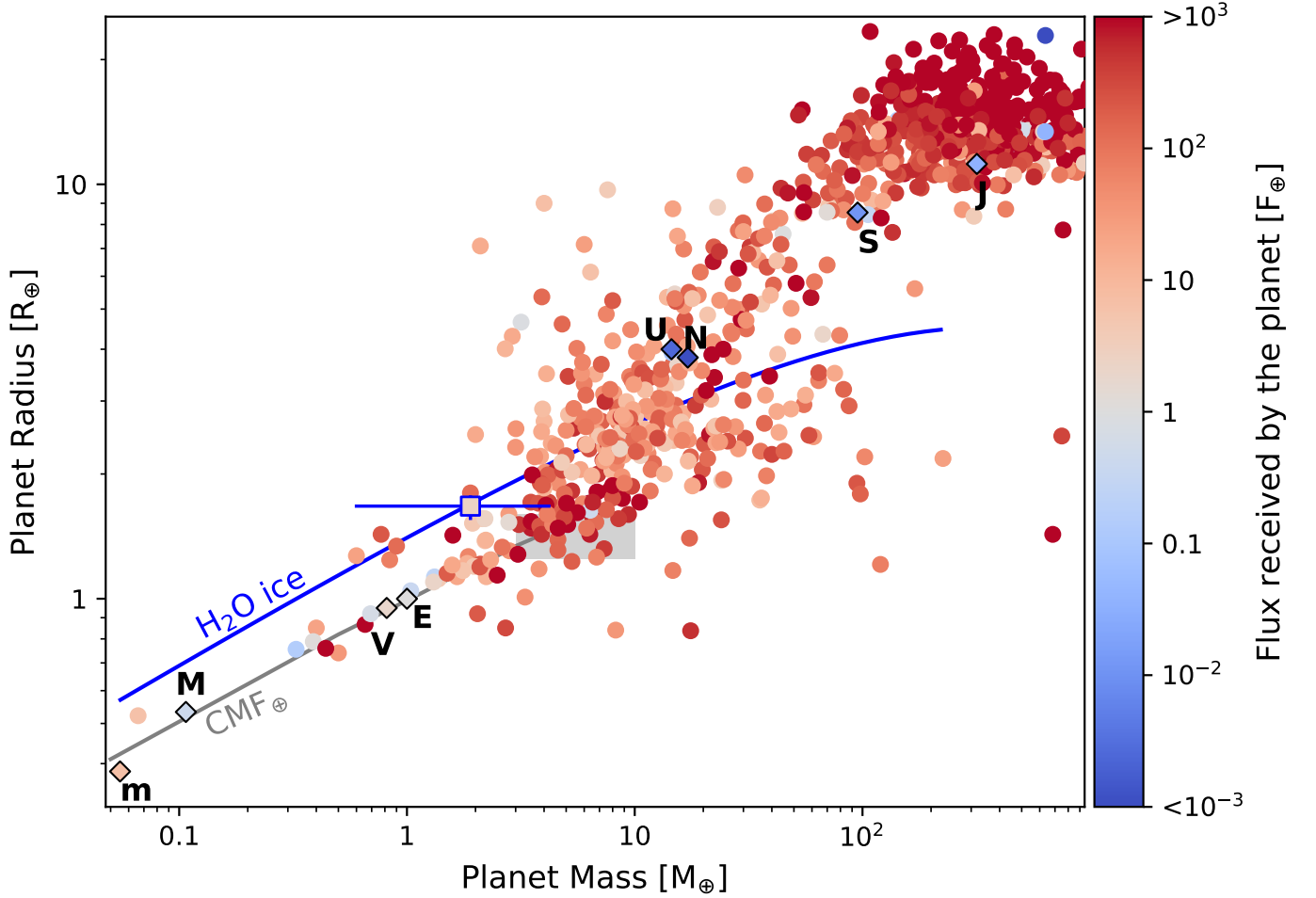


Figure 1. A mass-radius diagram for currently known exoplanets (small circles), the solar system planets (diamonds with letter designations), and TOI-1266c (square). Error bars for the mass and radius of TOI-1266c are also shown. The symbols are colored by instellation normalized to what the Earth receives ($\sim 1367 \text{ W/m}^2$). The gray shaded region denotes the commonly accepted mass-radius regime for super-Earths. Two compositional trends are identified on the plot: the mass-radius relationship for a pure water ice planet ($\text{'H}_2\text{O ice'}$; Seager et al. 2007), and for a planet with the same core mass fraction as the Earth ('CMF_\oplus '; Unterborn et al. 2016).

main solutions: a water-rich steam world, and a dense Mercury-like planet. As shown by Stefansson et al. (2020), TOI-1266c is broadly consistent with a water-dominated planet (Fig. 1; see also Aguichine et al. 2021). This can be seen when comparing to modeled mass-radius relationships for more complex compositions. For example, an Earth-like planet surrounded by up to 50 wt% (percent water by mass) can have radii of up to $1.47 R_\oplus$ (Fu et al. 2009), which is 12% smaller than the observed radius for TOI-1266c (though this is still within 2σ). The model grid from Zeng et al. (2019) includes several 50% water/Earth-like rocky core planets with isothermal pure- H_2O atmospheres that roughly match TOI-1266c’s mass and radius. More generalized formulations for ice/rock/iron fractional compositions suggest that TOI-1266c is $\sim 60\%$ water ice (Fortney et al. 2007) or $\gtrsim 77\%$ liquid water (Noack et al.

2016) by mass. These estimates are comparable to the maximum ice content expected for planets formed beyond the ice line (e.g. Mordasini et al. 2009), suggesting that in this scenario, both planet b and c migrated inwards to their present locations. However, none of these mass-radius relationships have self-consistent atmospheres, which can lead to underestimates in the estimated radius (e.g., Turbet et al. 2020).

Steam atmospheres are often discussed within the context of the loss of water either during the magma ocean phase of a planet, immediately following accretion (e.g., Zahnle et al. 1988; Schaefer & Fegley Jr 2010; Hamano et al. 2013; Katyal et al. 2019) or as a result of stellar brightening inducing a runaway greenhouse state (e.g. Kasting 1988). However, abundant water (and other heavy gases) could also be accreted (Kral et al. 2020) or outgassed later in a planet’s life (Kite et al. 2020; Kite

& Barnett 2020; Kite & Schaefer 2021), potentially setting up a scenario in which the runaway state is entered much later in the planet’s life.

One unavoidable consequence of a potentially water-dominated planet receiving slightly more irradiation than Venus is atmospheric escape. Venus is thought to have lost its water at some point in its history (e.g., Kasting 1988; Way & Del Genio 2020) due to high temperatures allowing significant amounts of water in the upper atmosphere, where it could be photolyzed and create hydrogen atoms that then escape the atmosphere (e.g., Kasting & Pollack 1983). A high hydrogen escape flux would also drag along oxygen (e.g., Zahnle & Kasting 1986; Schaefer et al. 2016; Luger & Barnes 2015; Tian 2015). Of particular note for M dwarfs is their prolonged pre-main sequence lifetimes, during which they are 10-100 times brighter than their main sequence luminosities (Luger & Barnes 2015; Luger et al. 2015). As a result, planets like TOI-1266c have multiple avenues by which their atmospheric composition can evolve in time, even to the extent that the planet loses its atmosphere entirely (e.g. Kreidberg et al. 2019; Poppenhaeger et al. 2020). A second issue is that planets orbiting M dwarfs may be volatile-poor due to the high impact velocities during formation (e.g., Lissauer 2007). However, if the planet began with larger initial volatile inventories (e.g. Luger et al. 2015), replenished its atmospheric volatiles through regassing from the interior (e.g. Moore & Cowan 2020), or experienced slower than expected atmospheric escape, TOI-1266c may still have a substantial envelope today.

On the other extreme, the $2\text{-}\sigma$ upper mass limit of $6.4 M_{\oplus}$ for TOI-1266c would indicate that the planet is $>50\%$ iron core (following the mass-radius relationship given by Noack et al. 2016), near the size limit driven by collisional stripping from impacts during accretion (Marcus et al. 2010). TOI-1266c would then represent a super Mercury at less than half of Mercury’s instellation, which would have implications for the composition of its atmosphere. At lower planetary masses, TOI-1266c would likely still have an iron core but could also have a modest H_2 -He envelope, on the order of 0.2-0.5% of the total planet mass (Lopez & Fortney 2014; Zeng et al. 2019).

However, several theoretical arguments make it difficult to form an iron core with a substantial H_2 -He fraction. First, a gas-rich initial composition is inconsistent with rocky planet formation models, which suggest that substantial accumulation of H_2 and He from the protoplanetary disk requires a minimum core mass $\gtrsim 5\text{--}20 M_{\oplus}$ (e.g., Rafikov 2006, 2011). Planets with small rocky cores are also subject to atmospheric ‘boil-off’ sup-

ported by the planet’s inability to cool rapidly enough (Owen & Wu 2016), potentially followed by loss driven by the cooling of the core (e.g. Misener & Schlichting 2021) and/or photo-evaporation (e.g. Owen & Wu 2017). Boil-off would prevent the accumulation of more than a few tenths of a percent H_2 , even if the planet began with $>10\%$ by mass H_2 (Owen & Wu 2016). Core-powered mass loss and photoevaporation would further reduce the amount of H_2 , ultimately leaving behind an evaporated core (Luger et al. 2015) that would be inconsistent with current mass and radius constraints for TOI-1266c. These arguments effectively rule out a H_2 -dominated state, although it is important to note that more complex models of the mass and radius evolution of volatile-rich planets still suggest a peak for planets with $\sim 1\%$ H_2/He atmospheres (Chen & Rogers 2016). Additionally, secondary loss processes like ion pickup could further modify the atmosphere (see Gronoff et al. 2020, for an overview), although the stellar wind for TOI-1266 is only modest at present ($\lesssim 4 \times 10^{-14} M_{\odot}/\text{yr}$, based on rotation constraints) (Johnstone et al. 2015a).

We can combine this with the limited information we have about the solar system giants. Uranus and Neptune have interior ‘high-metallicity’ (elements heavier than He) components ranging from 75-90% of the their total mass, depending on whether silicates and/or ices are assumed to be the ‘metal’ (e.g., Hubbard 1981; Helled et al. 2010). This is consistent with other estimates regarding the internal composition of sub-Neptune-sized exoplanets (e.g., Wolfgang & Lopez 2015). This translates to roughly 11-13 and 13-15 M_{\oplus} for Uranus and Neptune, respectively (Helled et al. 2010; Dodson-Robinson & Bodenheimer 2010), larger than the $2\text{-}\sigma$ upper bound on TOI-1266c’s mass estimate. The ice component (thought to be the majority of the core; Hubbard 1981) is expected to be of supersolar metallicity (Lodders & Fegley Jr 1994), with Neptune having a higher oxygen-to-hydrogen fraction (corresponding to a higher water ice fraction). This could also push the C/O ratio to higher values, approaching ~ 1 (Ali-Dib et al. 2014, see also the review by Mousis et al., 2020a). Several studies have motivated C/O ratios closer to 0.5 and a modest amount of ammonia ice (Nettelmann et al. 2016), which would be physically consistent with protoplanetary material that experienced full clathration (Mousis et al. 2020a). This is further complicated by the fact that assumptions about atmospheric structure and what type of adiabat the temperature profile follows (ranging from dry to wet) shift the retrieved atmospheric metallicity by a factor of a few (Cavalié et al. 2017).

Taken together, there is a compelling case to assume that TOI-1266c is volatile-rich, and may even be an

eroded sub-Neptune core. We take CO_2 as the major carbon-bearing species, as the CO/CH_4 transition and the CO_2 fraction peak at intermediate temperatures and pressures for higher-metallicity atmospheres (Lodders & Fegley Jr 2002; Venot et al. 2014); likewise, N_2 dominates over NH_3 (Burrows & Sharp 1999).

2. METHODS

We use a one-dimensional radiative-convective cloud-free model from Kopparapu et al. (2013, 2014), which was updated from the original version (Kasting 1988; Kasting et al. 1993) with new H_2O and CO_2 absorption coefficients. We employ inverse climate calculations in which the vertical temperature profile is specified, and radiative fluxes from the planet are back-calculated to determine the equivalent incident stellar flux. The atmosphere is divided into 101 layers. The model uses a moist pseudoadiabatic extending from the “surface” (assumed to be at 100 bar) up to an isothermal stratosphere of 200 K. The surface temperature is varied until the effective solar flux (S_{eff}) matches the observed incident flux on the planet. S_{eff} is calculated from the ratio between the net outgoing IR flux (F_{IR}) and the net incident solar flux (F_{sol}), both evaluated at the top of the atmosphere. Essentially, by changing the surface temperature to match the incident stellar flux in our model, we are making sure that energy balance is maintained. The model top pressure is set to 10 μbar . Short-wave and long-wave fluxes are calculated using a δ -2-stream approximation (Toon et al. 1989) using separate eight-term, correlated-k coefficients for H_2O .

We also use a one-dimensional photochemical model that is a fork of Atmos¹ (Arney et al. 2017) with a modified version of the C-H-O photochemical network from VULCAN² (Tsai et al. 2017, see Appendix A). We deliberately set aside nitrogen chemistry for this study because of the additional complexity necessary to include it in our model, and because of the uncertainties associated with speciation (we will return to this briefly in Section 4.1). Initial tests with a 0-dimensional chemical equilibrium model suggest that in the relatively oxidizing water-dominated scenarios we explore here, nitrogen is largely present as N_2 , which would contribute to a higher mean molecular weight for the atmosphere but have few other practical impacts. The atmosphere is assumed to be well-mixed below the ‘surface’ at 100 bars. The model also includes newly-measured water vapor photolysis cross sections (Ranjan et al. 2020). We use the ultraviolet through near-infrared spectra for GJ

581 (France et al. 2016; Youngblood et al. 2016; Loyd et al. 2016) as a proxy for TOI-1266, as they have comparable effective temperatures, luminosities, and ages, within uncertainties (Selsis et al. 2007; Dragomir et al. 2012; Gaia Collaboration et al. 2018). GJ 581 is technically a variable star, but its brightness variations are $<1\%$ (Dragomir et al. 2012).

In our photochemical simulations, we ensure that the total mixing ratio is unity by using He as the remainder of the atmosphere. The amount of He added is generally $\lesssim 1\%$ by volume. As an aside, He abundances could be reduced by drag-off if escape fluxes are high, but we find using another gas (such as Ar) for this purpose has no qualitative impact on our photochemical results. We have also chosen a vertical eddy diffusion parameter $K_{\text{zz}} = 10^{10} \text{ cm}^2/\text{s}$ consistent with other preliminary studies of hot Jupiters (e.g., Venot et al. 2014), noting that we have no constraints on the internal heat flux, rotation rate, and magnetic field strengths in order to constrain this value (e.g., Visscher et al. 2010, and references therein). We explore the effect of differing K_{zz} later, but to first order, lower values of K_{zz} decrease the vertical extent of the well-mixed region of the atmosphere, but do not significantly impact the results described below.

Given TOI-1266c’s current equilibrium temperature (see Table 1), it is unlikely that there is a substantial supercritical water component, and instead, TOI-1266c is ‘liquid’ water-dominated (Brugger et al. 2017; Mousis et al. 2020b). While the lower atmospheres in all of the cases we present here are above the critical temperature of water, the upper atmosphere passes through the temperature range where water would normally condense. We include in our calculations an updated H_2O saturation vapor pressure over water and ice (Meyer et al. 1983; Haar et al. 1984), and moderate the condensation loss frequency to ensure that the atmosphere is not substantially supersaturated where liquid water can condense ($\geq 233 \text{ K}$), and below this the condensation over ice is allowed to decrease, reflecting higher possible supersaturations (Wallace & Hobbs 2006; Korolev & Mazin 2003), consistent with observations of cirrus clouds on Earth (e.g., Krämer et al. 2009). This is in keeping with other studies of temperate water-dominated atmospheres (e.g., Piette & Madhusudhan 2020). We do not, however, include either aerosols to serve as cloud condensation nuclei nor the necessary microphysical models to capture cloud formation processes, nor the radiative effects of clouds, and caution that the estimated cloud properties are solely illustrative. We return to this later in the Section 4.

¹ Atmos on GitHub

² VULCAN on GitHub

One additional constraint on the composition of the atmosphere is the cumulative impact of historic X-ray (X) and extreme ultraviolet (EUV) radiation-driven mass loss (the sum is represented as XUV). To do this, we have developed a simple model of atmospheric loss³ separate from the other two models. The escape model interpolates the BaSTI luminosity evolution grid⁴ of [Hidalgo et al. \(2018\)](#) to the observed mass and luminosity of the host star (see [Fig. 2](#), top panel), similar to [Barnes et al. \(2020\)](#). The stellar luminosity evolution of [Hidalgo et al.](#) agrees with other stellar evolution models ([Baraffe et al. 2015](#)) from ~ 0.01 -10 Gyr (the interval for the [Baraffe et al.](#) grid), and include time points back to 0.01 Myr and out to the end of the main sequence, even if this is beyond the age of the universe. Given the large uncertainty in the age of TOI-1266, this larger stellar age range allows for a more complete uncertainty analysis. We then use the X-ray and EUV scaling relationships from [Peacock et al. \(2020\)](#) (see [Fig. 2](#), bottom panel), rather than the empirical scaling with respect to the bolometric luminosity (L_{bol}) from [Sanz-Forcada et al. \(2011\)](#), for two reasons. First, the EUV luminosity (L_{EUV}) from [Sanz-Forcada et al.](#) is above 1% of L_{bol} for ~ 0.2 Gyr, and above 0.1% for over 1 Gyr, due to the lack of an EUV saturation threshold for younger stars. The second issue with using the parameterizations of [Sanz-Forcada et al.](#) is that for a dimmer star like TOI-1266, there is a discontinuity in the calculated X-ray luminosity (L_X) saturation timescale ($\tau_i \sim 0.33$ Gyr) using their Equation 5, such that the post-saturation L_X is briefly higher than it is in the saturated regime. During our initial tests, we chose to empirically set the saturation timescale to when the time-dependent X-ray luminosity falls below the saturated value, resulting in $\tau_i \sim 0.47$ Gyr, which produced a negligible change in the total mass lost. We instead chose to use the X-ray and EUV scaling relationships from [Peacock et al. \(2020\)](#) in order to address these two discrepancies. [Peacock et al.](#) note a saturation of $\sim 10^{-2} F_{\text{EUV}}/F_{\text{bol}}$ in their simulations of $\sim 0.4 M_{\odot}$ stars, slightly higher in magnitude but qualitatively consistent with work for larger stars (e.g., [King & Wheatley 2020](#)). Additionally, the log-linear dependence on age after the saturated period is comparable with other early M dwarf studies (e.g., [Stelzer et al. 2013](#)). These specific values from [Peacock et al. \(2020\)](#) are converted from flux ratios to luminosity ratios using the luminosity, distance, and 2MASS J-band magnitude listed in [Stefansson et al. \(2020\)](#), assuming

that the J-band fluxes are proportional to the bolometric luminosity⁵.

Our escape model also takes advantage of the parameterizations available to distinguish between the radiation/recombination-, energy-, photon-, and diffusion-limited escape regimes ([Murray-Clay et al. 2009](#); [Owen & Alvarez 2016](#); [Lopez 2017](#)). This is not strictly necessary, as the XUV fluxes at TOI-1266c are much less than those experienced by hot Jupiters thought to be undergoing radiation/recombination-limited escape. ([Murray-Clay et al. 2009](#)). However, depending on our choices for the mass loss efficiency (a.k.a., the heating efficiency), atmospheric composition, and XUV luminosity saturation, the atmosphere transitions between the energy-, photon-, and diffusion-limited escape regimes at different times.

We also assume that our escape calculations are largely insensitive to exospheric temperature, except for across the critical XUV flux identified for hot Jupiters ([Koskinen et al. 2007](#)). This is motivated by the interesting coincidence of the critical XUV flux necessary to drag off atomic oxygen from a terrestrial planet's atmosphere (~ 40 times the XUV flux received by Earth today; [Luger & Barnes 2015](#)) and the XUV flux at which H_3^+ cooling becomes ineffective at moderating thermospheric temperatures for gas giants ([Koskinen et al. 2007](#)). For gas giants, this transition produces an order of magnitude increase in the thermospheric temperature and atmospheric scale heights ([Koskinen et al. 2007](#), their Fig. 1a). Temperature changes are accurately assessed as a secondary effect in the critical XUV flux relationship for planets in their host star's main sequence habitable zone shown by [Luger & Barnes \(2015\)](#), since the critical XUV flux goes as $T^{-1/4}$. However, including a $10\times$ change in temperature would cause the critical XUV flux to decrease by more than a factor of two (that is, the onset of oxygen drag-off would occur at lower fluxes). For habitable zone planets like those studied by [Luger & Barnes](#) and [Ramirez & Kaltenegger \(2014\)](#), this assumption does not introduce significant errors over the $\lesssim 1$ Gyr that these planets spend enduring the superluminous phase of their host stars. As we focus on water-dominated scenarios, the prevalence of molecular hydrogen and oxygen in the thermosphere suggests a closer resemblance to the upper atmosphere of Earth or Jupiter ($\sim 1,000$ -2,000 K) than the CO_2 -dominated atmospheres of Venus and Mars (~ 200 -300 K; [Mueller-Wodarg et al. 2008](#)), but under high instel-

³ GitHub repository for SNOWBALL

⁴ <http://basti-iac.oa-abruzzo.inaf.it/>

⁵ Changes in stellar effective temperature are $\lesssim 10\%$ for 0.4 - $0.5 M_{\odot}$ stars over their lifetimes ([Baraffe et al. 2015](#); [Hidalgo et al. 2018](#)), which would shift the wavelength peak by < 50 nm.

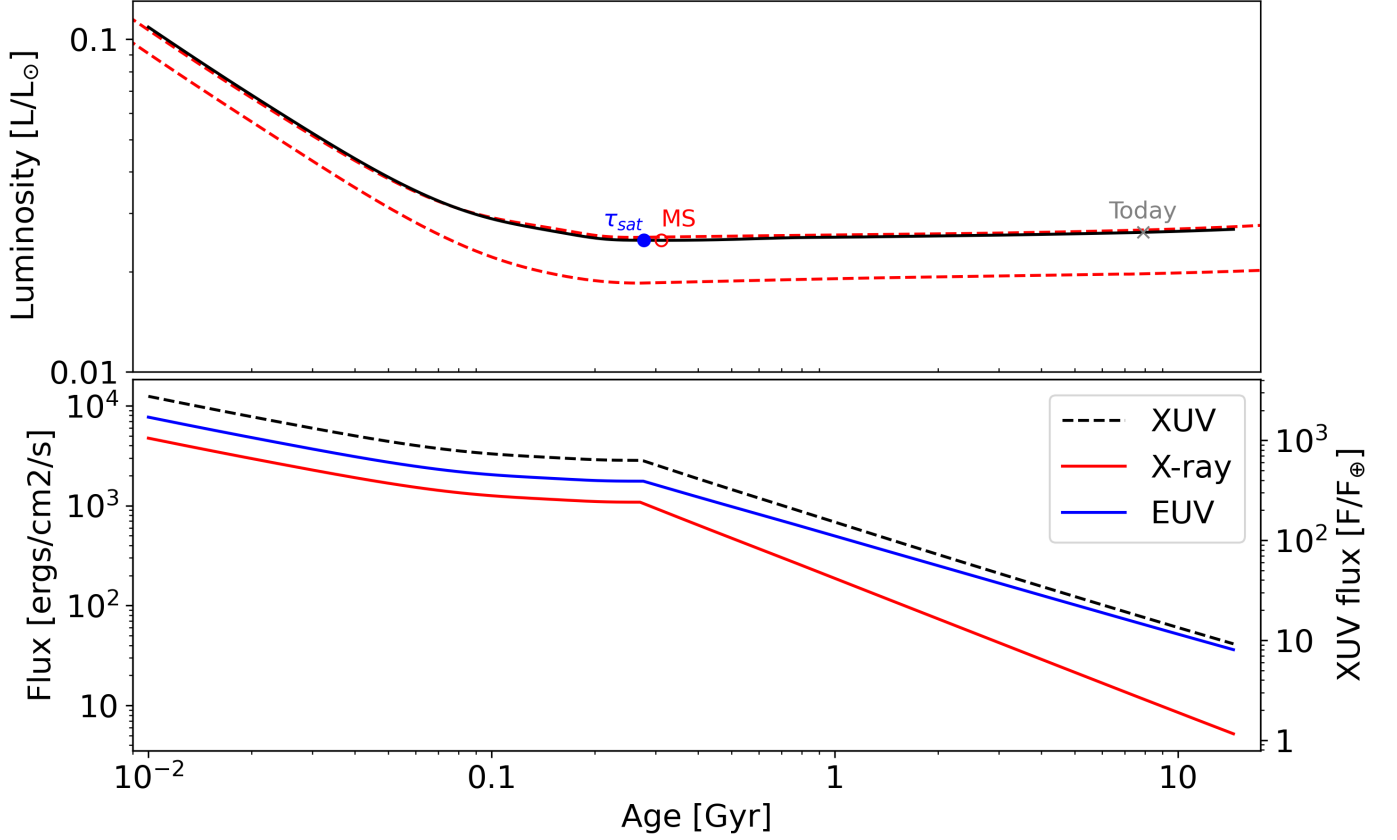


Figure 2. Top panel: The notional luminosity evolution of TOI-1266 (black curve). The two red dashed curves denote the 0.4 and 0.45 M_{\odot} stellar evolution tracks of [Hidalgo et al. \(2018\)](#), which have been interpolated and normalized to match the observed luminosity at the current age estimate (denoted with the gray X and labeled ‘Today’) for TOI-1266. The XUV saturation time is denoted as τ_{sat} , and the start of the main sequence with ‘MS’. Bottom panel: The X-ray (red), EUV (blue), and total XUV (black dashed) reflect the combination of both the evolving luminosity (top panel) and the saturation parameterizations from [Peacock et al. \(2020\)](#). For reference, the XUV flux is shown on the right-hand axis as normalized to what the Earth receives ($\sim 4.5 \text{ erg/cm}^2/\text{s}$).

lation, even CO_2 -dominated thermospheres are $\gtrsim 10,000$ K ([Tian 2009](#)). This, combined with the potential for Lyman- α cooling at high XUV fluxes (e.g., [Murray-Clay et al. 2009](#)), suggests that above $\sim 180 \text{ erg cm}^{-2} \text{ s}^{-1}$ the exospheric temperature is $\sim 10,000$ K, and $\sim 1,000$ K below this flux threshold. Since TOI-1266c receives $>180 \text{ erg cm}^{-2} \text{ s}^{-1}$ for nearly 3.5 Gyr, we find that escape of atomic oxygen continues for 2 Gyr longer than if we were to adopt the critical XUV flux suggested by [Luger & Barnes](#) of $\sim 400 \text{ erg cm}^{-2} \text{ s}^{-1}$ for a planet with TOI-1266c’s current mass and radius. This results in lower potential for accumulated oxygen abundances in nearly every scenario for TOI-1266c, consistent with prior work that demonstrated oxygen accumulation and escape self-consistently for XUV fluxes 10-100 times larger than what the Earth receives today ([Fig. 2](#); e.g., [Zahnle & Kasting 1986](#)).

We assume mass loss efficiencies (η_{XUV}) in line with other authors, including $\eta_{\text{XUV}} \sim 0.1\text{--}0.15$ for X-ray-dominated H_2 escape for a planet of comparable size to

TOI-1266c ([Owen & Jackson 2012](#); [Bolmont et al. 2017](#)), and $\eta_{\text{XUV}} \sim 0.01$ for H_2O following [Lopez \(2017\)](#), based on protoplanetary disk photoevaporation studies ([Ercolano & Clarke 2010](#)). These are meant only as order-of-magnitude approximations, since the efficiency is dependent on planetary mass, radius, and envelope composition and its radiative properties, as well as the flux of high-energy radiation from its host star, and as such will evolve (e.g., [Murray-Clay et al. 2009](#); [Owen & Wu 2013](#)). A planned next step is to use the flux-dependent efficiencies of [Bolmont et al. \(2017\)](#), noting that there is still some uncertainty when comparing these to efficiencies for close-in giant planets (e.g., [Koskinen et al. 2014](#)).

Because of the inherent uncertainties associated with almost every aspect of the atmospheric escape as well as the planet’s mass and composition, we employ a Monte Carlo approach and perform a suite of escape simulations over the range of parameter uncertainties set out in [Table 2](#). The atmospheric composition values are drawn

from a log-uniform distribution, whereas all other values are drawn from linear uniform ranges. Values are generated using the Latin Hypercube sampling (LHS) method in the *Surrogate Modeling Toolbox* (Bouhlel et al. 2019), which leverages the Enhanced Stochastic Evolutionary algorithm (Jin et al. 2003) to optimize the *Design of Experiments Toolbox* (pyDOE) implementation. One important caveat is that this set of simulations assumes the maximum amount of water available for a given mass and radius, following the relationships derived by Noack et al. (2016). We note that the mass-radius relationships from Noack et al. (2016) do not include an atmosphere, but in our simulations the vertical extent of the region between 1 bar and ~ 10 mbars is ~ 400 – 600 km, which would change the apparent radius by less than the reported uncertainty. The Noack et al. mass-radius relationship places a physically-motivated lower limit for the planet’s mass of $\sim 1.6 M_{\oplus}$ from the lower bound on the planet’s radius, where the planet would be 100% water. If future observational constraints on the planet’s mass are below this threshold, the planet must have a non-negligible amount of H_2 at present. More complex compositional mixes are beyond the scope of the present work, but abundant H_2 in TOI-1266c’s atmosphere would most likely eliminate the possibility of oxygen accumulation from hydrogen loss, as well as posing an interesting conundrum for the formation and evolution mechanisms highlighted above that would remove an H_2 -dominated atmosphere.

Lastly, we use the Planetary Spectrum Generator⁶ (PSG; Villanueva et al. 2018) to produce synthetic transmission spectra for the scenarios outlined here. PSG is an online radiative transfer suite that integrates the latest radiative transfer methods and spectroscopic parameterizations, and includes a realistic treatment of multiple scattering in layer-by-layer spherical geometry. It can synthesize planetary spectra (atmospheres and surfaces) for a broad range of wavelengths for any given observatory. We validate these results with PandExo (Batalha et al. 2017b).

3. RESULTS

3.1. Atmospheric Escape

We begin by estimating the atmospheric lifetime for TOI-1266c, assuming the observed mass and radius for the present day (Fig. 3). A pure-water atmosphere experiences substantial water loss over its lifetime, as can be seen in the top panel of Fig. 3, but still retains abundant H_2O through ~ 8 Gyr (vertical dashed

Property [units]	Default Value	Tested Range
Stellar age [Gyr]	7.9 Gyr	2.7–12.1
Current luminosity [L_{\odot}]	0.02629	0.02554–0.027
Planet mass [M_{\oplus}]	1.9	1.6–6.4
Planet radius [R_{\oplus}]	1.673	1.563–1.76
Atm. mass [M_{\oplus}]	—	<i>see note [1]</i>
Atm. composition [vmr]		
H_2	—	10^{-6} –1
He	—	10^{-6} –1 [2]
H_2O	—	10^{-6} –1
CO_2	—	10^{-6} –1
Escape efficiency		
H_2	0.1	0.01–0.4
H_2O	0.01	0.01–0.4
CO_2, O_2	0.01	0.01–0.1

Table 2. Monte Carlo test ranges for the variables in the atmospheric escape simulations. [1] The planetary volatile abundance was set to the maximum water abundance allowed for the selected mass and radius given by Noack et al. (2016). [2] The helium abundance in the escape simulations was set by scaling the solar He: H_2 ratio (0.3367) by the value drawn from the stated range, given the selected H_2 abundance. The atmospheric composition was normalized as a final step.

line). That said, the volatile inventory is roughly one-third oxygen by the present day (assuming the oxygen is not absorbed by the planet’s interior), resulting in spectroscopically-detectable oxygen (we will return to observations later). A second test, which includes a modest amount of hydrogen, can be seen in the bottom panel of Fig. 3. This scenario demonstrates that a relatively minor amount of H_2 ($\sim 0.4\%$ of the planet’s initial mass) can prevent significant loss of water and the commensurate accumulation of O_2 , as the H_2 combines with any free oxygen to replenish H_2O (this is an explicit prescription in our model). This amount of H_2 is broadly consistent with what might remain following atmospheric boil-off (Owen & Wu 2016). In both of these cases, the mass of the total volatile inventory does not substantially change throughout the planet’s life, and in total the mass changes by $\sim 1\%$ and the radius by ~ 0.3 – 0.5% over this same interval. However, it is important to note that this is equivalent to losing ~ 100 Earth oceans, substantially more than the initial water reservoirs explored in other work (e.g., Luger & Barnes 2015). These evolutionary tracks are useful for illustrating the behavior of individual scenarios near the boundaries between regimes, but given the large uncertainties in some critical parameters, it is important to fully explore the impact of atmospheric escape on the present state of TOI-1266c.

⁶ <https://psg.gsfc.nasa.gov/index.php>

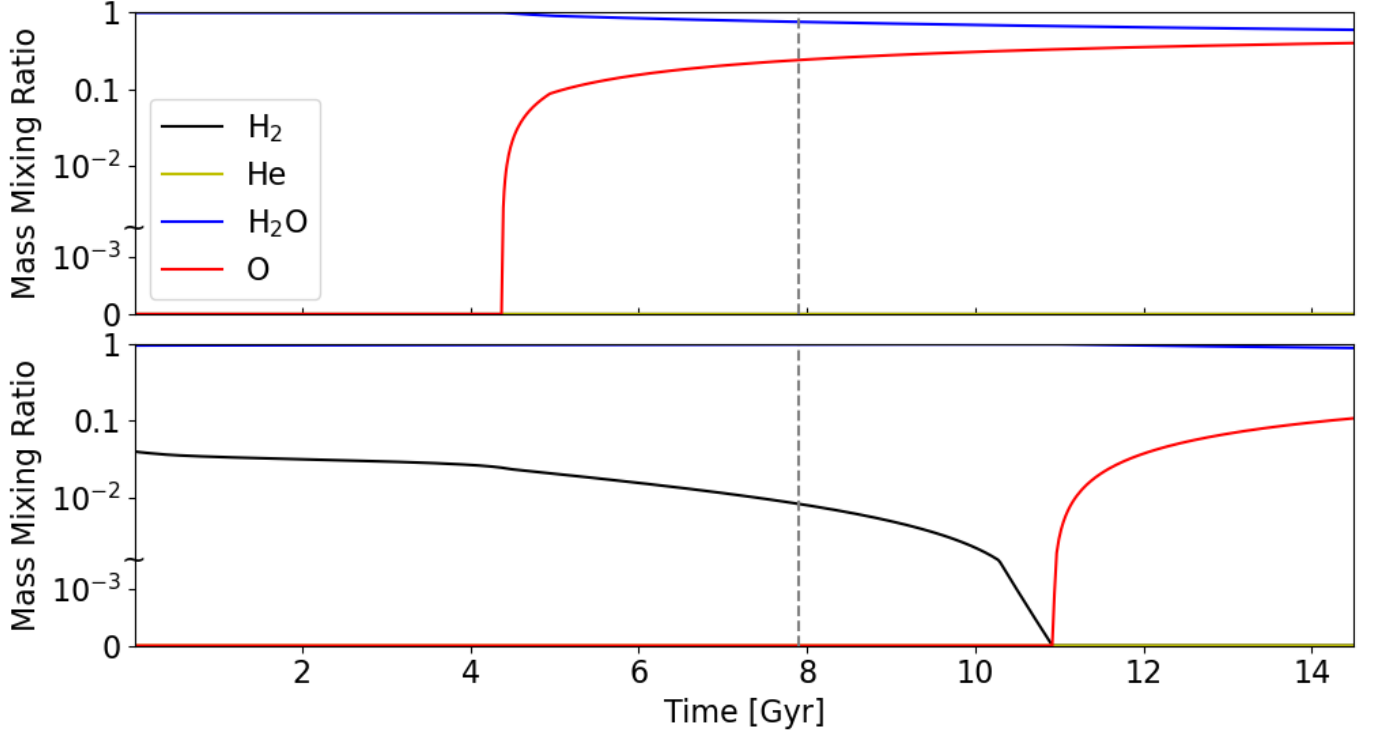


Figure 3. An example of one planetary evolution simulation, starting at $\sim 2 M_{\oplus}$ and $\sim 1.7 R_{\oplus}$, which ultimately evolves to match TOI-1266c’s observed mass and radius at TOI-1266’s estimated age (vertical dashed line). Top panel: 10% H_2O by mass; bottom panel: 9.6% H_2O and 0.4% H_2 by mass. Note that the vertical axis is logarithmic above the tilde and linear below it.

As such, we ran a suite of 10,000 atmospheric escape simulations covering the stated uncertainty ranges in Table 2. Several common-sense interpretations of this initial exploration can be gleaned from Fig. 4, namely 1) smaller initial planet masses for the same planetary radius correspond to larger potential water (volatile) inventories (denoted by the size of the points), which is a natural consequence of our experimental design; 2) larger volatile inventories are more difficult to lose completely, and suppress substantial accumulated oxygen mass fractions; and 3) it is unlikely that a planet more massive than $\sim 3.5 M_{\oplus}$ would have any remaining H_2O because of the small initial volatile inventories, and consequently, could have large oxygen mass fractions. The apparent gulf spanning intermediate oxygen mass fractions from 3.5-6.5 M_{\oplus} reflects complete desiccation of initially hydrogen- and water-dominated states that are pulled up to the 100% oxygen mass fraction state, barring a few simulations with escape efficiencies at the bottom of the tested range and/or young stellar ages. The remainder of the scenarios have small initial water fractions that do directly correspond to the oxygen mass fraction, but do not group up in the same way. There is also no significant trend with H_2 escape efficiency (Fig. 13) for the planet parameters and atmospheric compo-

sitions tested here, although this may not be the case for other regions of the parameter space.

3.2. Initial Temperature/Pressure and Water Profiles

The initial water vapor profiles produced by the radiative-convective model were used to initialize the photochemical simulations. All of the following simulations assume the nominal radius and mass for TOI-1266c ($1.673 R_{\oplus}$ and $1.9 M_{\oplus}$; Stefansson et al. 2020), as well as a water-dominated atmosphere. As an aside, the climatological and photochemical water vapor profiles for the same temperature/pressure conditions differ slightly. This is largely due to the combination of photolysis and vertical mixing (via both parameterized advection and molecular diffusion) in the photochemical model that modifies the water profiles in the upper atmosphere (above ~ 10 mbar) by a factor of a few (Fig. 15). For the atmospheric compositions explored here, this results in transmission spectra uniformly decreased by a few parts per million at all wavelengths between the climatological water profiles and the photochemical water profiles as a result of the change in mean molecular weight (not shown). This may not be the case for every scenario, however, particularly if water is more efficiently segregated to the lower atmosphere (for example, through weaker vertical mixing or efficient scavenging processes).

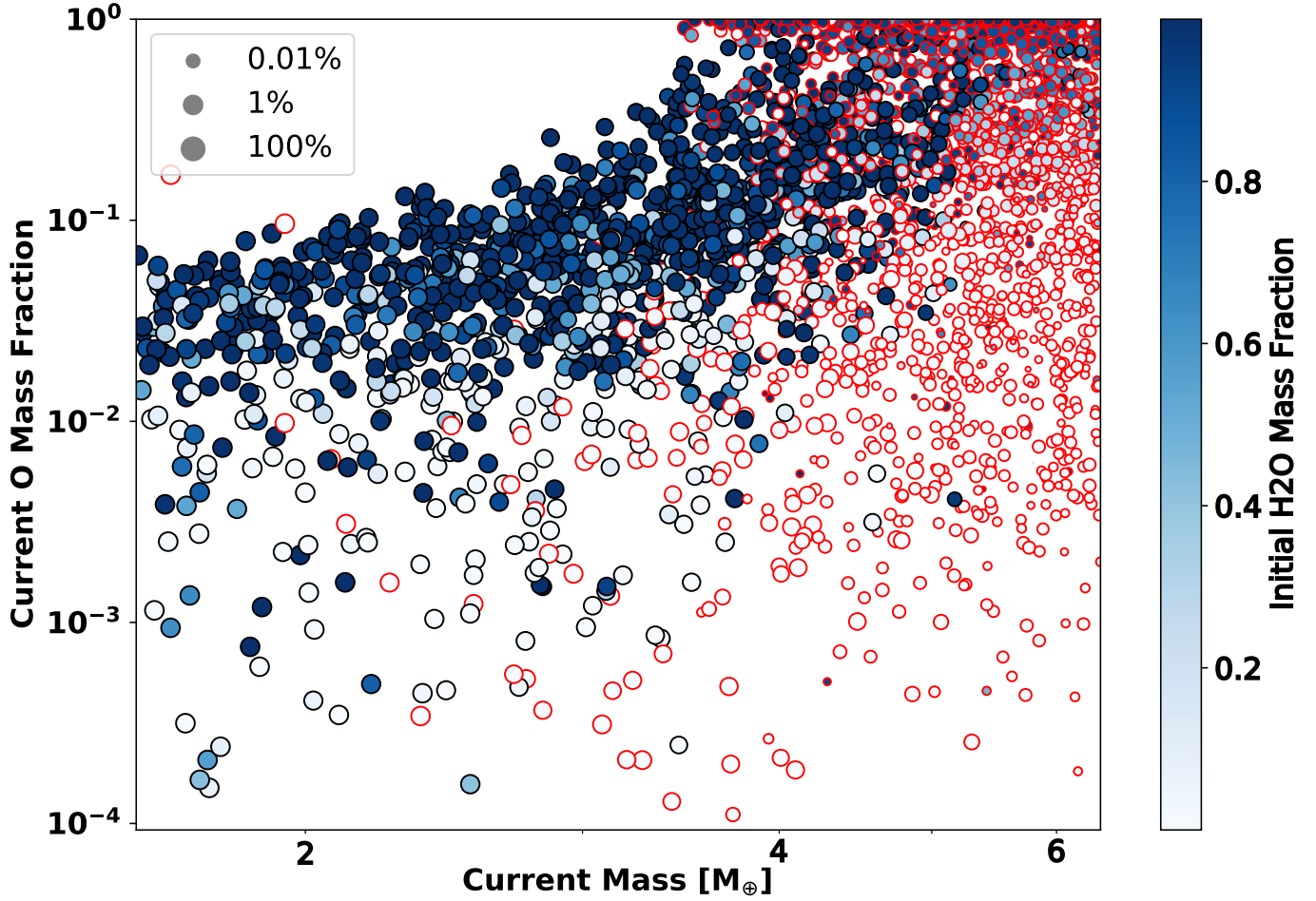


Figure 4. Water loss ensemble results calculated based on the range of planet parameter uncertainties from Table 2, plotted as a function of the current planet mass and the current envelope mass fraction of free oxygen. Symbols are colored by the initial envelope mass fraction of H_2O , and the size is scaled based on the fraction of the planet initially designated as envelope (taken to be the maximum water abundance permitted by the mass-radius relationship of Noack et al. (2016)). A red edge color for a given symbol denotes a scenario with less than 1 Earth ocean at present day, which would likely be short-lived (Kasting & Pollack 1983).

The three families of atmospheres ($\text{H}_2+\text{H}_2\text{O}$; $\text{H}_2+\text{CO}_2+\text{H}_2\text{O}$; $\text{O}_2+\text{H}_2\text{O}$) have some shared attributes, including the same general pressure ranges for the condensation of water (Fig. 5, left panel). Of the O_2 -bearing scenarios, only the intermediate-concentration cases (0.1% and 1% O_2) have water vapor profiles with higher upper atmospheric concentrations than the case with the highest water fraction. This is in contrast to both the H_2 and CO_2+H_2 scenarios, which have more saturated upper atmospheres for higher mixing ratios of the diluting species. The CO_2 scenarios are warmer in the deep atmosphere because of CO_2 's efficacy as a greenhouse gas, while H_2 is more effective than O_2 as a collisional broadening partner, resulting in intermediate temperatures.

3.3. Atmospheric Chemistry

Our photochemical modeling is informed by the atmospheric escape and radiative-convective simulations of TOI-1266c, focusing here on an initial exploration limited to H-C-O chemistry (future work will include other species). Each of the three families of water-dominated atmospheres have lesser amounts of H_2 , H_2+CO_2 , or O_2 which drive the chemistry of trace species. As we discuss later, many of these changes are not visible in the integrated planetary spectra, but they are integral to accurately capturing the major species. The Appendix has a collection of figures that highlight how each species changes with different major species' concentrations, but we will only focus on those that may be potentially observable (e.g., O_2 , O_3 , H_2O , CO_2 , and CO). The water-dominated scenarios we focus on here are too oxidizing for substantial amounts of CH_4 , C_2H_6 , or other reduced carbon compounds, which likely precludes a hydrocar-

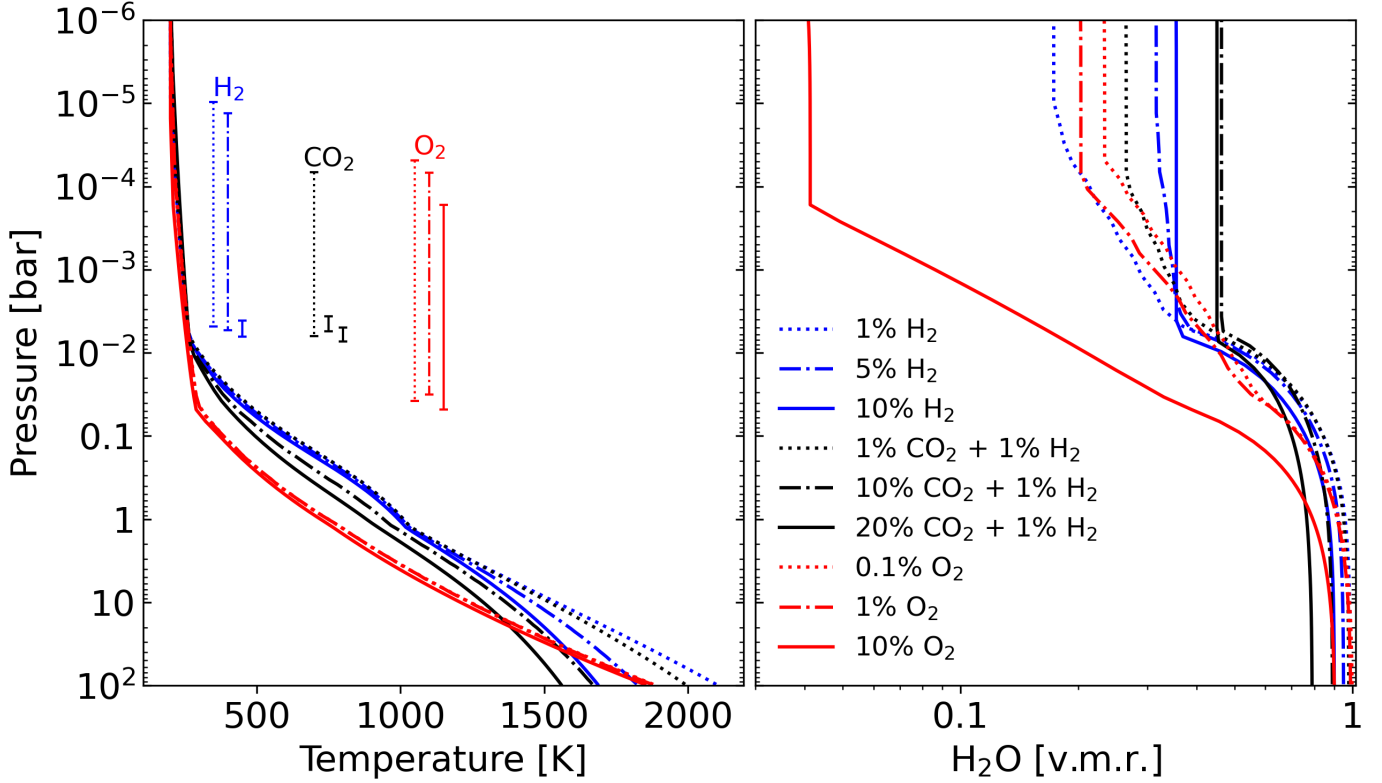


Figure 5. Temperature (left) and water vapor volume mixing ratio (v.m.r; right) profiles for the cases outlined in the text. The onset of water vapor condensation (vertical range in the left panel) occurs just above the ‘knee’ in the water profiles, consistently around ~ 1 -10 mbar.

bon haze. Of the species that are likely to be observable, only O_3 and CO are essentially free to respond to instellation and compositional changes, while O_2 , H_2O , and CO_2 are given fixed concentrations at the 100-bar pressure level that are then subject to dynamical and thermo- and photochemical processes. CO (Fig. 6, left panel) is largely produced by photolysis of CO_2 in the upper atmosphere and then mixed downwards into the deeper atmosphere, where the background CO concentration is set by thermochemical reactions.

Ozone, much like CO , is dependent on the concentration of another species (O_2), and secondary trace species and photolysis reactions that rapidly convert atoms between these two reservoirs. In terrestrial photochemical studies (e.g. Segura et al. 2003), the typical threshold to establish a robust O_3 layer is $\sim 1\%$ of Earth’s present atmospheric level of O_2 (i.e., $\sim 2\%$ by volume O_2). On Earth, the ozone layer is maintained by photochemistry at roughly ppm concentrations between ~ 0.5 -50 mbar. This pressure range is comparable to the scenarios with more abundant O_3 in Fig. 6 (right panel), but the mixing ratios are lower by a factor of $\sim 10^3$. The lower concentration of O_3 for these scenarios is driven by the higher abundance of OH radicals in the upper atmosphere derived from water vapor photolysis (see Ap-

pendix A), in line with earlier work that demonstrated a reduction in O_3 with warmer atmospheres and high OH abundances (Chen et al. 2019). Because all of the scenarios explored here have non-negligible H_2O abundances, increasing the O_2 abundance beyond 10% by volume produces a roughly linear increase in the peak O_3 mixing ratio (not shown), still much less than the maximum ozone mixing ratio in Earth’s atmosphere. We will return to remote detectability later.

4. DISCUSSION

The atmospheric escape calculations showcase a number of evolutionary pathways that are in line with other estimates for super-Earths and sub-Neptunes (e.g. Estrela et al. 2020), and TOI-1266c sits at the nexus of the potential states, although it would constitute a low-instellation terrestrial planet following Estrela et al.. One possible outcome is that TOI-1266c was (and remains) a rocky planet composed of predominantly silicates and iron. TOI-1266c would then most resemble a super-Venus (Barclay et al. 2013; Kane et al. 2013), but even among Venus-like planets some variation is expected (e.g. Schaefer & Fegley Jr 2011; Kane et al. 2018). Barring the potentially brief steam atmospheres immediately following formation and/or a later transi-

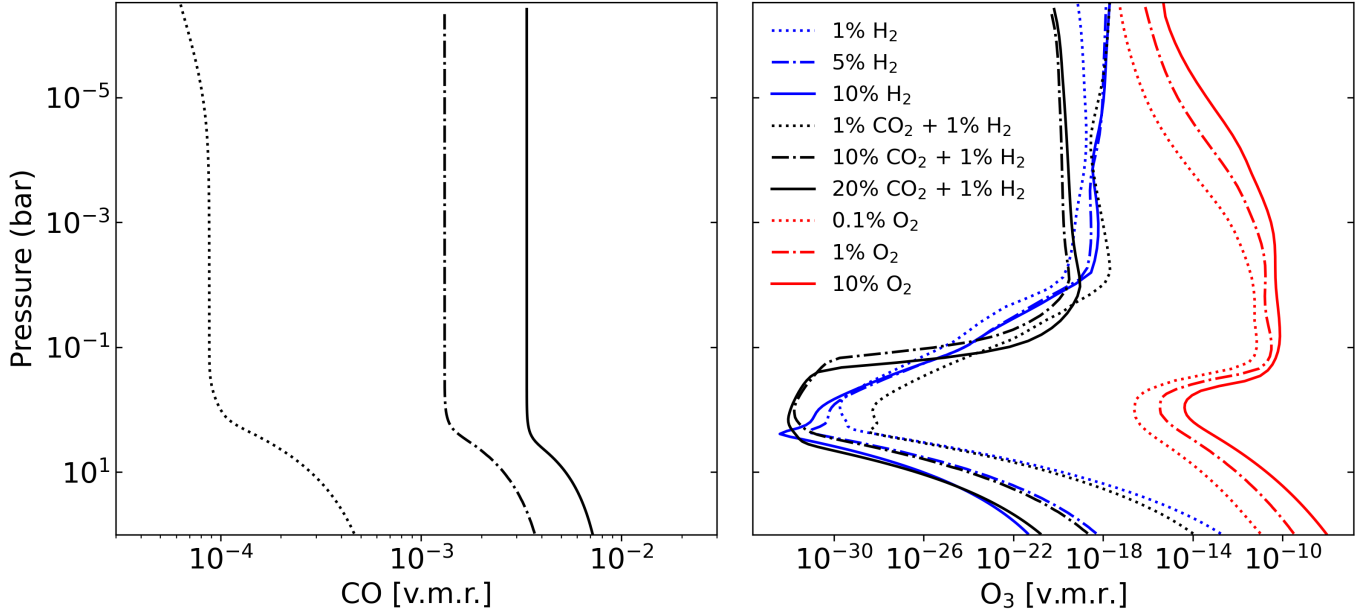


Figure 6. Left panel: CO mixing ratio profiles for the three atmospheres that contain CO₂ in significant abundance. Right panel: O₃ mixing ratio profiles for the nine principle scenarios included in this study.

tion into the moist and runaway regimes (e.g. Hamano et al. 2013; Driscoll & Bercovici 2013; Way et al. 2016), however, the lack of a substantial volatile inventory results in dry, rocky super-Venuses. On the other end of the compositional spectrum, hydrogen-dominated sub-Neptunes boast larger spectroscopic features requiring fewer transits to obtain sufficient signal-to-noise (e.g. Chouqar et al. 2020, see also Fig. 10). For strongly irradiated objects, however, the impact of atmospheric escape should be considered when estimating atmospheric and bulk composition, much like how we have chosen to consider largely H₂O-dominated scenarios for TOI-1266c.

4.1. Chemical considerations

The carbon speciation is dependent on temperature (Lodders & Fegley Jr 2002), so while we have used the conjectured water and methane ice fractions from the Uranus and Neptune as a starting point, the equilibrium speciation heavily favors CO₂ over CH₄ at the lower boundary. If the planet starts out as more reduced, CO₂ would shift towards CO and ultimately CH₄; however, even trace amounts of water vapor are able to rapidly convert photochemically-produced CO back into CO₂ such that the upper atmosphere would have a smaller abundance of CO than would be predicted solely from thermochemistry. The assumed ‘surface’ pressure also affects the abundances of trace species (Yu et al. 2021), but we have not tested this explicitly in our simulations. Beyond this, other factors, such as the choice of K_{zz} , can further modify the concentrations of trace species.

We have explored the sensitivity of atmospheric composition to changes in K_{zz} by decreasing it from our default value of 10^{10} cm²/s down to 2×10^7 cm²/s. Below this value, our photochemical model has difficulty converging. This appears to be due to the descent of the homopause (also called the turbopause) into the warmer, denser parts of the atmosphere below the isothermal stratosphere (note the sharp decrease in concentration at the upper boundary in Fig. 14). Lower K_{zz} values affect our chemical profiles in much the same way as they affect other models (e.g. Visscher & Moses 2011; Venot et al. 2014; Gao et al. 2018). Additionally, we find no significant deflection in the location of the water condensation region, which would have a much stronger effect on the observations (e.g., Fig. 7, top panel) than the variations in species’ concentrations with K_{zz} . Uranus and Neptune have K_{zz} values closer to $\sim 10^8$ cm²/s (Cavalié et al. 2017). Stronger mixing and/or different temperature profiles can give the appearance of lower metallicities (ibid.). Mixing length theory (e.g., Visscher et al. 2010) suggests that $K_{zz} \sim 10^6$ – 10^8 cm²/s throughout the model domain if the internal heat flux is 50–50,000 erg/cm²/s, comparable to modern Earth and Jupiter, respectively (Gando et al. 2011; Pearl & Conrath 1991).

For this initial work, we have neglected species that could play an important role in modifying the atmospheric structure and evolution. For example, sulfur chemistry has been shown to significantly modify the thermal profile of hot Jupiters (Zahnle et al. 2009), while sulfuric acid aerosols have been suggested as an alternative way to form a cold trap (Walker 1975), given

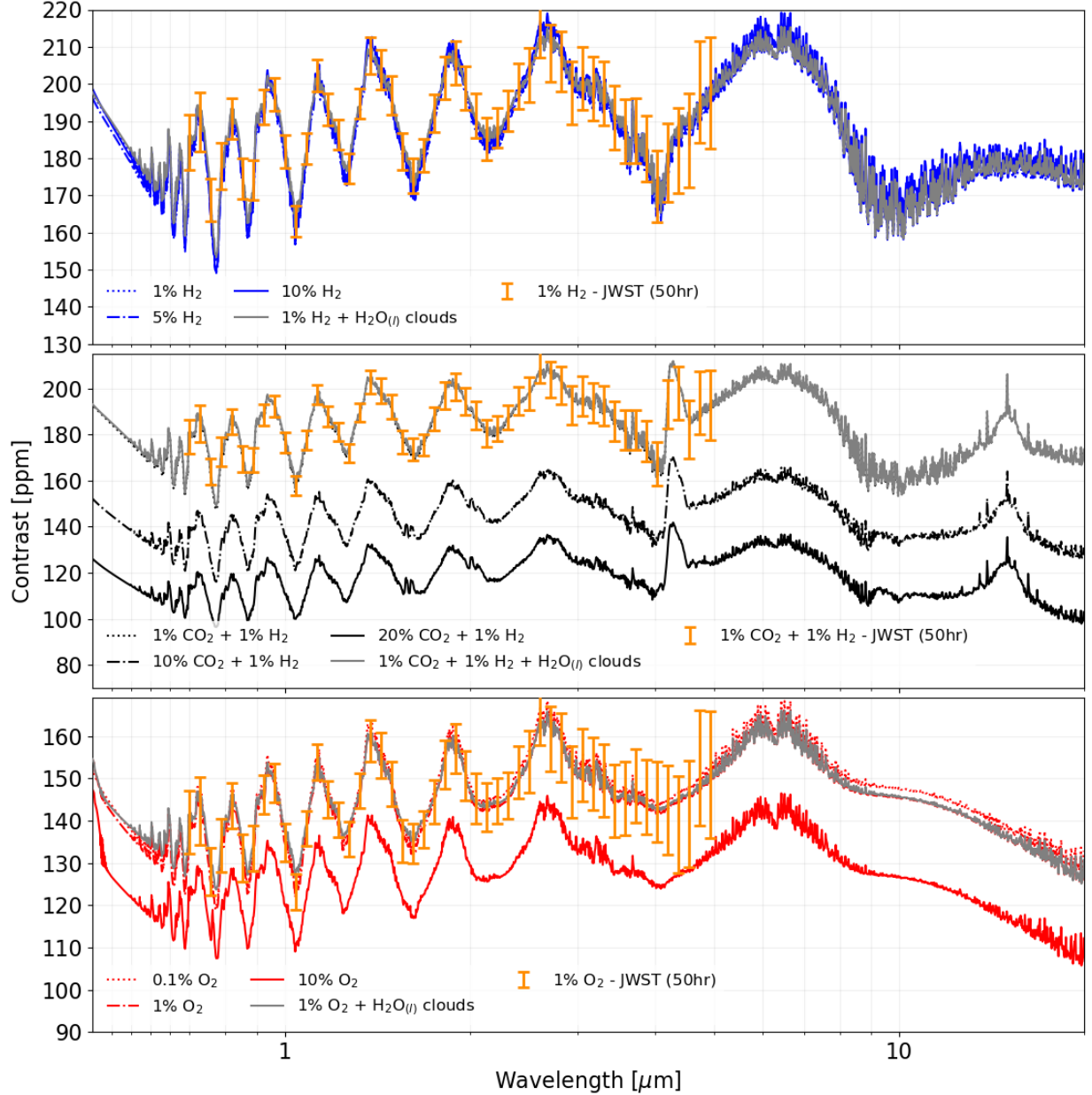


Figure 7. Synthetic spectra ($R=500$) of the nine cases highlighted previously. The panels are divided into families based on the gas mixture of interest: $\text{H}_2+\text{H}_2\text{O}$ (top panel), $\text{CO}_2+\text{H}_2+\text{H}_2\text{O}$ (middle panel), and $\text{O}_2+\text{H}_2\text{O}$ (bottom panel). A zoomed-in view of the $4.3\text{-}\mu\text{m}$ CO_2 feature can be found in Fig. 8, while Fig. 9 focuses on key O_2 and O_3 features. For each 1% mixture, we overplot two other spectra. The orange error bars are for a simulated observation using JWST’s NIRSpec-Prism ($R=100$, but plotting only every fourth point). We also overplot a cloudy scenario, assuming $14\text{-}\mu\text{m}$ liquid water droplets with a volume mixing ratio of 0.1 ppm (Kopparapu et al. 2021) are distributed throughout the pressure range identified in Fig. 5.

their hygroscopic tendencies in Venus’ modern atmosphere (e.g., Krasnopolsky & Pollack 1994; Yung et al. 2009; Tsang et al. 2010). Additionally, if NH_3 is a substantial component for ice giant cores (e.g., Nettelmann et al. 2016), then NH_3 could be present in the gas phase and contribute to the total reducing power available to the atmosphere. Particularly for the scenarios where TOI-1266c loses most of its hydrogen, nitrogen could

oxidize into NO_x compounds, analogous to NO_x derived from persistent lightning storms (e.g., Ardaseva et al. 2017). However, the temperature profiles used here all lie above the N_2/NH_3 equal-abundance pressure-temperature curve (e.g. Fortney et al. 2021), suggesting that ammonia incorporated as ice may affect the total atmospheric pressure (as N_2) and act as a source of reducing power by equilibrating to form H_2 at depth

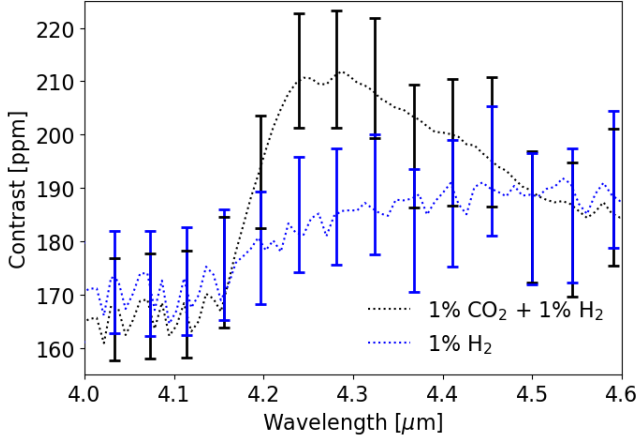


Figure 8. Synthetic spectra ($R=500$) for just the 1% $\text{CO}_2+\text{H}_2+\text{H}_2\text{O}$ and 1% $\text{O}_2+\text{H}_2\text{O}$ mixtures from Fig. 7, focusing on the $4.3\text{-}\mu\text{m}$ CO_2 absorption feature. The corresponding error bars are for the simulated 50-hour observation using JWST’s NIRSpec-Prism ($R=100$), and indicate that these two cases would be distinct from one another with JWST.

without NH_3 necessarily becoming a major constituent in the atmosphere. Lastly, if TOI-1266c has a silicate core, then moderately volatile elements like Na and Cl could contribute to atmospheric composition either directly (that is, there may be a rock vapor atmosphere) or indirectly (e.g., through catalytic and secondary reactions with the major species).

Hazes, either driven by condensation or by photochemistry, represent significant hurdles for characterizing exoplanetary atmospheres. Here, we have only considered water and a few other potentially major species, but the presence of sulfuric acid clouds on Venus (Kawabata et al. 1980) or other sulfur-based aerosols (e.g., Zahnle et al. 2009, 2016; Gao et al. 2017) are possible if sulfur is present in trace amounts. This could lead to observational degeneracies between a solid surface or a highly reflective cloud top (e.g., Lustig-Yaeger et al. 2019b). Similarly, abundant carbon could lead to the formation of organic aerosols, but the relatively water-rich and lower temperature scenarios tested here largely prevent carbon-carbon chemistry. Even with the uncertainties in TOI-1266c’s mass allowing for a predominantly silicate composition, a modest amount of water loss would produce enough free oxygen to effectively preclude organic aerosols (e.g., Hörst et al. 2018), unless the oxygen left over from water loss were absorbed by the solid planet (e.g. Luger & Barnes 2015). However, if the planet started out relatively water-poor, or more diverse haze formation pathways are considered, hazes seem likely (Moran et al. 2020; Reed et al. 2020; Vuitton et al. 2021), and could be of various compositions with

distinct optical properties (e.g. He et al. 2018, 2020a,b). Spectroscopic characterization, in combination with better mass constraints, would effectively narrow down the possibilities, much like it would for the TRAPPIST-1 system (Moran et al. 2018). Other secondary condensate species could be present, such as potassium chloride (KCl) (e.g., Gao et al. 2018), which could enhance the effectiveness of (or serve in their own right as) cloud condensation nuclei (CCN) for water clouds.

4.2. Redox considerations

As a super-Earth, TOI-1266c’s size requires that we use caution with regards to the common assumptions about the atmospheric composition and evolution of warm Neptunes (e.g., Hu & Seager 2014; Moses et al. 2020). As mentioned previously, TOI-1266c may be rocky, and if so, may have started out with a relatively H_2 - and He-poor composition before subsequently losing the H_2 and He over its lifetime. In our Monte Carlo simulations, the average scenario lost $\lesssim 1\%$ of the planet’s mass by the present day, but at the same time, the mean envelope fraction declined by $\sim 20\%$ of its initial value. This makes intuitive sense – the largest impact of atmospheric escape is seen in those cases where the atmosphere is initially only a small fraction of the planet’s mass. Studies suggest that more massive planets under higher instellation have comparable mass losses for higher H_2 mass fractions, which would produce larger variations in the planet’s present-day radius (Estrela et al. 2020).

Alternatively, if TOI-1266c is more massive, then water may be sequestered into and later outgassed from a magma ocean, preserving a relatively high water mass fraction (Kite & Schaefer 2021). If TOI-1266c started with a water-dominated atmosphere without a sufficient buffer of H_2 , then the persistent loss of H, derived from water vapor photolysis, would fundamentally alter the redox of the planet through the accumulation of oxygen. Since we have hypothesized scenarios in which TOI-1266c has substantial amounts of water at present, this build-up of oxidants would still be happening today. These oxidants could react with a magma ocean and drive chemical alteration, or they could be sequestered through incorporation into high-pressure ice phases. Transport via convection through high-pressure ice layers has been studied for icy satellites (e.g., Deschamps & Sotin 2001) and water-dominated super-Earths (Fu et al. 2009; Noack et al. 2016), and would allow for both a supply of reducing gases from the interior and redox evolution of the interior driven by atmospherically-derived oxidants.

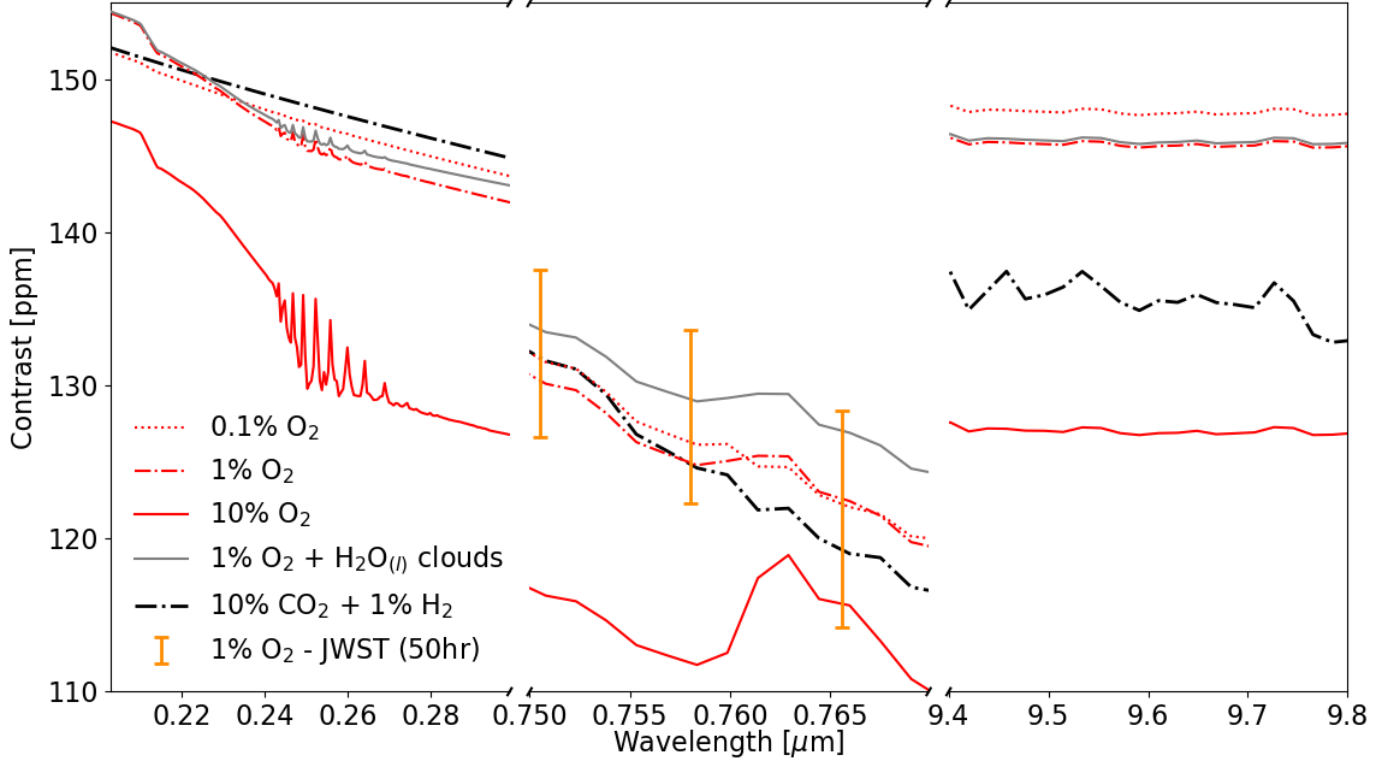


Figure 9. Synthetic spectra ($R=500$) for just the O_2+H_2O mixtures from Fig. 7, compared with the 10% CO_2 mixture. Note the O_2 A-band feature at $0.76 \mu m$ increases to ~ 10 ppm at 10% O_2 . However, the $0.2-0.3 \mu m$ and $9.6 \mu m$ ozone features are absent due to the lack of a substantial O_3 column abundance (the $0.2-0.3 \mu m$ region has O_2 features from the Herzberg continuum, but no contributions from O_3). Variations between the spectra in this region are due to the increasing atmospheric mean molecular weight at higher O_2 abundances. The orange error bars are for a simulated observation using JWST’s NIRSpec-Prism ($R=100$). We also overplot a cloudy scenario, assuming $14\text{-}\mu m$ liquid water droplets with a volume mixing ratio of 0.1 ppm (Kopparapu et al. 2021) are distributed throughout the pressure range identified in Fig. 5.

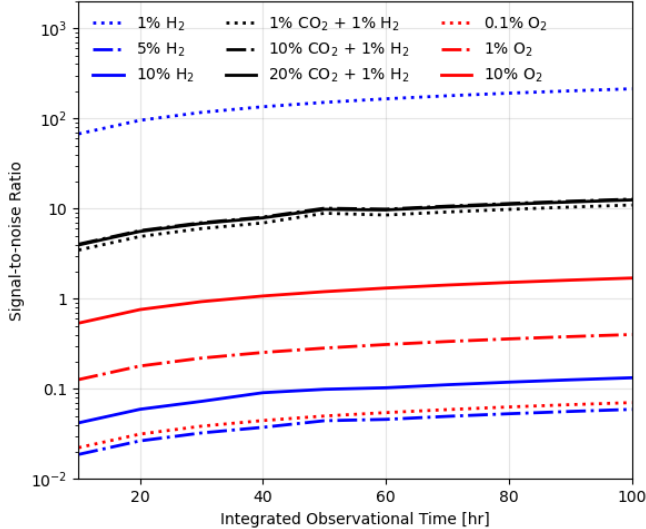


Figure 10. Signal-to-noise ratio for observations with JWST at $0.7-5 \mu m$. The composition is dominated by H_2O , and has secondary constituents denoted by the label.

4.3. Other factors affecting atmospheric loss

Uranus and Neptune’s water-dominated interiors have adiabats that likely pass through the superionic portion of the high-pressure and high-temperature water phase diagram (Redmer et al. 2011; Knudson et al. 2012; Millot et al. 2018). This may explain why Uranus and Neptune are the only planets with multipolar rather than dipolar fields (Schubert & Soderlund 2011). If TOI-1266c is more water-dominated than the ice giants, then the pressure-temperature profile does not cross through the superionic regime, which could result in a weaker planetary magnetic field dominated by the dipolar component (e.g., Tian & Stanley 2013). We note, however, that our temperature-pressure profiles for TOI-1266c are incompatible with those of Tian & Stanley (2013) because we have assumed that the H_2 and H_2O are well-mixed. Additional components like ammonia or methane further complicate the conductivity of the high-pressure ice layers, but carbon and nitrogen may precipitate out together (e.g., Chau et al. 2011).

In terms of uncertainties related to the host star, our assumed stellar luminosity evolution is based on the grid of Hidalgo et al. (2018), which includes luminosity evo-

lution data for 0.4 and 0.45 M_{\odot} stars. Given that TOI-1266 is $\sim 0.44 M_{\odot}$, we could reasonably assume that it follows the 0.45- M_{\odot} stellar evolution. However, the observed luminosity for TOI-1266 and 0.45- M_{\odot} luminosity are different by $\sim +3\%$ at 7.9 Gyr (TOI-1266’s notional age). Taking the mass-weighted logarithmic mean of the [Hidalgo et al.](#) evolutionary tracks results in a $\sim 6\%$ discrepancy between observed and estimated present-day luminosities. Normalizing the luminosity to match both the observed stellar mass and luminosity has the unintended side effect of producing higher fluxes than the 0.45- M_{\odot} track early in the star’s history ([Fig. 2](#)). It is not immediately clear which approach is appropriate, but we find that using both the normalization and a weighted mean of the luminosities accurately reproduces the generic luminosity estimate derived from the stellar mass within $\sim 5\%$ ([Cuntz & Wang 2018](#)), as opposed to $\sim 12\%$ when using the 0.45- M_{\odot} evolution data (we use the [Cuntz & Wang](#) generic mass-luminosity relationship because TOI-1266’s mass estimate is on the cusp of where older formulations have a discontinuity [Kutner](#) (e.g., [2003](#)). Uncertainties in mass and luminosity have knock-on effects for when the star enters the main sequence and on the estimated atmospheric loss. Our methodology for the luminosity interpolation should be viewed with skepticism, and would improve with stronger constraints on stellar properties.

Additionally, the age uncertainties for TOI-1266 suggest that longer-term persistent atmospheric loss processes like interactions with the stellar wind (e.g., [Cohen et al. 2015](#); [Tilley et al. 2019](#); [Gronoff et al. 2020](#)) could either play a major role in the current state of TOI-1266c if the star is older, or still represent a small fraction of the total loss when compared to the loss estimates from the pre-main sequence super-luminous phase. While no observations of flaring for TOI-1266 have been reported at this time, stellar flares can further contribute to atmospheric erosion. Losses due to flaring are typically smaller than the baseline XUV-driven escape rates (e.g., [Atri & Mogan 2021](#)), although this may not be universal, particularly for stars that flare more frequently (e.g., [France et al. 2020](#)). Magnetohydrodynamical models of H_2 (e.g., [Johnstone et al. 2015b](#)) and H_2O (e.g., [Johnstone 2020](#)) loss, as well as generically H-dominated super-Earth loss rates ([Kislyakova et al. 2013](#)), suggest that loss is a certainty, even if the magnitude and dominant mechanisms remain open questions.

Another potential factor is the communication between the interior of the planet and its atmosphere. If, for example, TOI-1266c is water- or hydrogen-dominated, then the core component may effectively supply material to the escaping envelope (e.g., [Wilson &](#)

[Militzer 2011](#)), especially if H_2 is effectively incorporated into water ices ([Soubiran & Militzer 2015](#)) or separates out slowly over the course of the planet’s lifetime ([Bailey & Stevenson 2019](#)). However, if H_2 is ultimately immiscible (e.g., [Bailey & Stevenson 2019](#), and references therein), then the H_2 stranded in the atmosphere would be lost preferentially to H_2O , as discussed previously, leaving behind an ice-dominated core.

4.4. Spectral signatures and observations

In terms of differentiating the scenarios discussed here, CO_2 has a strong absorption feature at $\sim 4.3 \mu m$ (~ 40 ppm; [Fig. 8](#)) even for 1% CO_2 in a cloud-free atmosphere. This is broadly consistent with simulated retrievals of warm sub-Neptunes with *JWST* (e.g. [Greene et al. 2016](#)). The $4.3 \mu m$ feature would likely not be significantly impacted by the presence of haze (e.g., [Kemp-ton et al. 2017](#)). The O_2 features in the ultraviolet are relatively small ([Fig. 9](#)), while the $0.76\text{-}\mu m$ feature provides a relatively wide ~ 15 ppm signal in comparison. Because of the abundant water vapor and the modest O_2 mixing ratios, O_2 - O_2 dimer spectral features ([Misra et al. 2014](#); [Fauchez et al. 2020](#)) are unlikely to be present or observable. From [Fig. 9](#), and more broadly [Fig. 10](#), it is clear that *JWST* will be unable to positively identify oxygen without a substantial investment of observational time, even for the relatively extended, warm atmospheres we consider here.

CO and O_3 , derived from CO_2 and O_2 , also have spectroscopic features that can help in distinguishing these scenarios. CO has weak features at 1.6, 2.3, and $4.7 \mu m$ ([Wang et al. 2016](#); [Schwieterman et al. 2019](#)), but these are subsumed by strong H_2O and CO_2 features at those wavelengths. Interestingly, the appearance of the O_2 A-band at $\sim 0.76 \mu m$ ([Fig. 7](#)) does not result in the commensurate rise of an O_3 feature at $9.6 \mu m$ that is expected for temperate, O_2 -rich atmospheres (e.g. [Segura et al. 2003, 2005](#); [Rugheimer et al. 2013](#); [Rugheimer & Kaltenegger 2018](#); [Meadows et al. 2018](#)). This was noted by [Chen et al. \(2019\)](#) as a result of OH reducing the O_3 concentrations, but here is comparable to the results first shown by [Pidhorodetska et al. \(2021\)](#), where high temperatures force the rapid thermal decomposition of O_3 (the back reaction of Reaction #309 in the Appendix). As a result, there is a 10^3 -fold reduction in O_3 , with O_3 being entirely absent from the integrated transmission spectra ([Fig. 9](#), $9.4\text{--}9.8 \mu m$).

The possibility of clouds at temperate conditions (230–290 K; $\sim 0.5\text{--}5$ mbar) acts in two ways to obscure spectral features ([Fauchez et al. 2019](#)): first, by limiting transmission through the deeper, warmer parts of the atmosphere, and by introducing strong intermediate-

temperature water features. This pressure range for condensation is in keeping with those reported in other studies of steam atmospheres. For example, Nikolaou et al. (2019) report much lower pressures as an upper bound, although those experiments have substantially more CO_2 than the cases described here. Water clouds may also appear in the atmospheres of more temperate massive planets (Charnay et al. 2020), again at around 10 mbar. However, some scenarios featuring clouds work to enhance spectroscopic features (e.g. Kawashima & Rugheimer 2019), which makes determining self-consistent cloud, climate, and photochemistry a critical next step. We have attempted to include the impact of clouds by assuming the clouds are composed of $\sim 14\text{-}\mu\text{m}$ droplets with a volume mixing ratio of 10^{-7} or ice clouds composed of $25\text{-}\mu\text{m}$ crystals with a mixing ratio of 10^{-9} . In both cases, the clouds do not appear to substantially impact the water spectral features (Fig. 7, gray curves), with ice clouds having a smaller effect, largely due to their smaller abundance. The smaller reduction, as compared to more temperate atmospheres (Fauchez et al. 2019), is likely due to the presence of water-vapor above the cloud-deck in a water-rich atmosphere that minimizes the impact of clouds on spectral features. A self-consistent cloud modeling effort is necessary to further this work.

TOI-1266c could be characterized by *JWST* in the future, which could effectively distinguish between some of these cases. The signal-to-noise ratio of a series of observations of TOI-1266c in transit is shown in Fig. 10. We calculate signal-to-noise as the difference between two synthetic spectra, one of which ignores the spectral contributions from the chief secondary species (e.g., H_2 , O_2 , or CO_2), dividing by the simulated noise. The counter-intuitive reduction in signal-to-noise with increasing H_2 abundances stems from the decreasing apparent water column mass. The other compositions show the opposite trend, driven by those gases having distinct spectroscopic features of their own. Ultimately, CO_2 and H_2O in significant abundances could be identified in a few tens of hours, but oxygen to a sufficient signal-to-noise ratio may be beyond *JWST*'s capabilities. As mentioned previously, the $4.3\text{-}\mu\text{m}$ CO_2 band would not be substantially affected by hazes, although further tests are necessary.

Further investigations of the radius gap have the potential to provide key insights into the processes that shape planets over their lifetimes. As the community continues to find more transitional objects, it is becoming increasingly clear that some of the exoplanets that are likely to be characterized in the near future may not be precisely what we expect them to

be. Volatile-depleted sub-Neptune cores masquerading as super-Earths could inadvertently skew our perspectives on habitability, such as if a water-dominated sub-Neptune is incorrectly classified as a terrestrial planet, since the large water fraction would suggest oceans so deep that they would suppress volatile exchange and plate tectonics (Kite et al. 2009).

5. CONCLUSIONS AND FUTURE WORK

The potential to observe a Venus analogue, particularly if it remains in a steam-dominated runaway greenhouse at present, offers an unparalleled window into the history and evolution of a unique terrestrial planet as well as one of the first few steam atmospheres accessible with *JWST*. Data about water-dominated atmospheres are also relevant to the bounds of habitability for terrestrial planets, particularly those that form around low-mass host stars (Luger & Barnes 2015) and orbit older stars (e.g. Rushby et al. 2013; Lehmer et al. 2020). Lastly, observations of exoplanets that may have accumulated oxygen derived from water loss are important to establishing a baseline for larger planet sample size analyses, particularly in the context of biosignatures (e.g. Bixel & Apai 2020).

Estimating the composition and any potential observables for TOI-1266c remains difficult. The degeneracies in relating bulk composition, atmosphere-to-solid planet fraction, and mean density (e.g. Rogers & Seager 2010; Dorn et al. 2015; Welbanks & Madhusudhan 2019) pose significant challenges in predicting the atmospheres of exoplanets even if the mass and radius are well constrained, and even spectroscopic observations of the planet may not necessarily break this degeneracy (Batalha et al. 2017a). Additional radial velocity observations—such as precision RVs with HPF (Mahadevan et al. 2012, 2014), NEID or CARMENES—are required to constrain the planet's mass, which will narrow the range of possible compositions (e.g. Valencia et al. 2013).

The modeling demonstrated here showcases the impact of dynamical, photochemical, and ancillary atmospheric processes on the disposition of some of the possible planetary states in the radius gap. These planets highlight the continuing need to understand the processes that shape highly-irradiated, volatile-rich planets in advance of observational campaigns with *JWST* and other future instruments. Follow-up observations are planned to better constrain TOI-1266c's mass (and by extension its possible composition). Regardless of whether or not TOI-1266c is the first such target to be observed, this class of objects requires additional capabilities beyond thermochemical equilibrium models and

assumptions about composition in terms of metallicity. In a future study, we plan to expand our photochemical scheme to include secondary species that were omitted in this work, as well as explore the feedbacks between climate, chemistry, and observability.

ACKNOWLEDGMENTS

Harman and Kopparapu acknowledge support from the GSFC Sellers Exoplanet Environments Collaboration (SEEC), which is supported by NASA’s Planetary Science Division’s Research Program. This work was performed as part of NASA’s Virtual Planetary Laboratory, supported by the National Aeronautics and Space Administration through the NASA Astrobiology Institute under solicitation NNH12ZDA002C and Cooperative Agreement Number NNA13AA93A, and by the NASA Astrobiology Program under grant 80NSSC18K0829 as part of the Nexus for Exoplanet System Science (NExSS) research coordination network.

Harman would like to thank James Kasting for his invaluable comments on the manuscript; Kevin Zahnle

for his help in hunting for technical issues during development, and both Mahmuda Afrin Badhan and Sandra Bastelberger for their work in improving and updating **Atmos**; Benjamin Drummond for his work in establishing an intercomparison of 1-D chemical kinetics codes, hosted as an ISSI International Team, which served as the nucleus of the code modifications used in this study, as well as Shami Tsai (also part of the Team) for his openness with **VULCAN** and insights on chemical kinetics. The authors would also like to thank the two anonymous reviewers for their comments, which improved the quality of the manuscript.

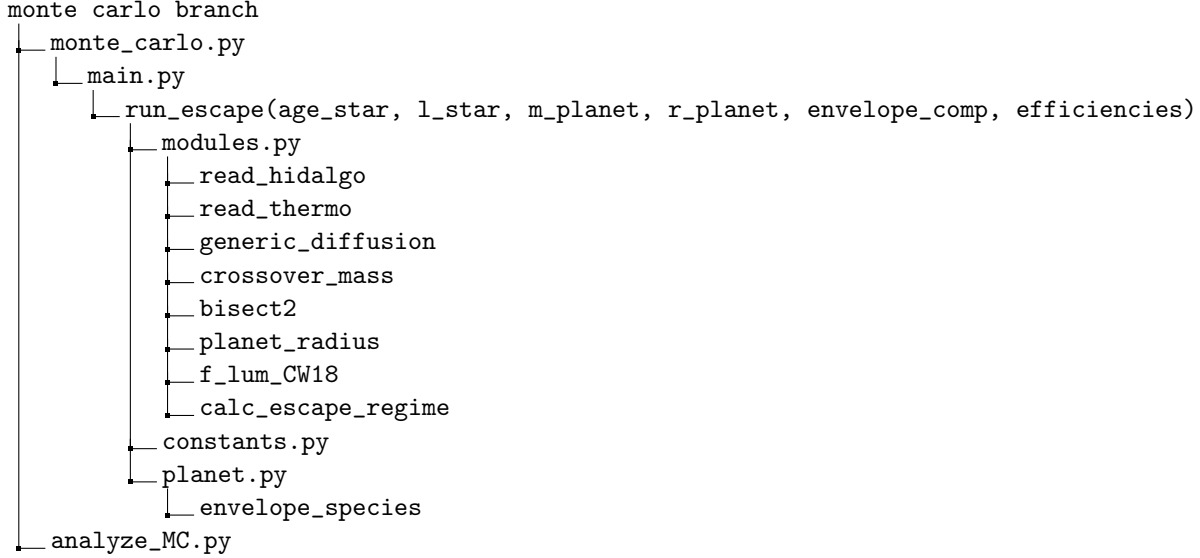
Software: **Atmos** (Arney et al. 2017), Planetary Spectrum Generator (PSG) (Villanueva et al. 2018)

APPENDIX

A. ATMOSPHERIC ESCAPE CODE DERIVATION AND DESCRIPTION

As described in the main text, our model for atmospheric escape is based on the stellar luminosity evolution models of [Hidalgo et al. \(2018\)](#) in conjunction with the escape flux parameterizations of [Murray-Clay et al. \(2009\)](#); [Owen & Wu \(2016\)](#); [Lopez \(2017\)](#). Here, we walk through the assumptions built into our model and how we implemented these processes.

The SNOWBALL repository has two branches – the `main` branch, and the `monte_carlo` branch. Both branches have largely the same code, save that the `monte_carlo` branch features a refactored `main.py` such that it can be called by the Monte Carlo generator program and return the results. Because the Monte Carlo application has additional assumptions, we will use that as the basis for the remainder of this discussion. The code is laid out in an attempt to compartmentalize individual physical concepts and processes, but because some are interconnected it is not always possible to completely separate some of them. Below is a partial dependency tree for how we calculate the escape regimes and fluxes (omitting generic and optional functions):



The program `monte_carlo.py` is responsible for calling the Latin Hypercube Sampling method ([Bouhlef et al. 2019](#); [Jin et al. 2003](#)) for the selected uncertainty ranges on the stellar age (`age_star`, in Gyr), present-day stellar luminosity (`l_star`, in terms of solar luminosity), initial planet mass (`m_planet`, in Earth masses), initial planet radius (`r_planet`, in Earth radii), initial volatile abundances for H₂, H₂O, He, and CO₂ (`envelope_comp`, as mass fractions of the initial envelope), and the escape efficiencies for H₂, H₂O, and the other gases (`efficiencies`). There are two caveats with respect to the volatile abundances. First, we set the helium mass fraction as being less than or equal to the solar He/H₂ ratio (24.85% He/73.8% H₂ by mass ~ 0.3367) by multiplying together the randomly-selected He ‘abundance’ fraction, the solar He/H₂ ratio, and the randomly-selected H₂ abundance. Second, because the ranges for the abundances can result in the combined mass fraction exceeding unity, we normalize the abundances following parameter sampling. All of the selected variables (age, luminosity, planet mass and radius, volatile abundances and escape efficiencies) are then passed in as arguments to `run_escape`.

The function `run_escape` initializes a given simulation, runs the scenario to the specified end time, and returns a number of diagnostic values to the parent `monte_carlo.py` program (`monte_carlo.py` then archives these values to a saved file on disk). We break down each of these steps below, and include the specific descriptions of function calls as they arise.

RUN_ESCAPE - SETUP STEP

The lion’s share of the setup deals with the stellar evolution track file read-in and interpolation. Initially, two evolution tracks for stars that bookend the given host star mass are identified, read in, and used to create two cubic interpolations for their luminosity evolution tracks as a function of stellar age. We then take the weighted logarithmic mean of the luminosities to represent the star in question – for example:

$$\log_{10}(L_*) = \frac{(M_* - M_i)}{(M_k - M_i)} * \log_{10}(L_i) + \frac{(M_k - M_*)}{(M_k - M_i)} * \log_{10}(L_k)$$

where M and L are the stellar mass and luminosity of each star, and the subscripts ‘*’ and i and k stand for the host star and two bookend stellar masses, respectively, such that $M_i < M_* < M_k$. As a second step, we then normalize the synthetic luminosity at the estimated stellar age to the observed present-day luminosity. This results in luminosities that are higher than those of the upper bookend stellar evolution track at ages less than 0.1 Gyr because the observed luminosity ($0.02629 L_\odot$; [Stefansson et al. 2020](#)) is higher than the interpolated luminosity ($\sim 0.0247 L_\odot$). This assumption is necessary, given our focus on matching the observables as closely as possible. Because of the higher present-day stellar luminosity, the planet experiences $\sim 3\%$ higher atmospheric mass loss over its lifetime, but this does not qualitatively change any of our conclusions. We next produce several diagnostics, including identifying the transition onto the main sequence, naïvely assuming that this corresponds to the global minimum in stellar luminosity. Lastly, we calculate the X-ray and EUV flux ratio with respect to the star’s evolving luminosity, with options available to use either the [Sanz-Forcada et al. \(2011\)](#) or the [Peacock et al. \(2020\)](#) relationships (as explained in the text, we have chosen the [Peacock et al.](#) parameterization). Once this is done, the other variables are initialized based on the values in the `planet.py` file. This file also has the options for specifying other choices for which luminosity evolution tracks are used ([Baraffe et al. \(2015\)](#) vs. [Hidalgo et al. \(2018\)](#)), whether the luminosity is normalized, and which UV scalings are applied.

One additional assumption we make, as described in the main text, is that for each set of randomly-sampled mass and radius, we construct an estimated envelope fraction based on the maximum possible water inventory using the composition-mass-radius relationship from [Noack et al. \(2016\)](#). We do this by iterating through the solution space starting with no iron core and checking to see if the planet radius falls between the 100% silicate and 100% water composition radii (using `bisect2` and `planet_radius`). If it is still too large, we slowly increasing the fraction of iron to shift the planet from a large initial volatile inventory and planet radius towards a solution that satisfies both the mass and radius.

RUN_ESCAPE - LOOP OVER TIME ARRAY

At each time point, several parameters can be derived from the stellar luminosity, the planet’s mass and radius, and the initial envelope composition. These include the:

- ‘Surface’ gravity $g = GM_p/R_p^2$ [m/s²]
- From [Lopez \(2017\)](#), the pressure where most of the XUV is absorbed $p_{XUV} \sim 8.8 \times 10^{-14} \times g$ [Pa]
- The atmospheric scale height $H = k_b T_{eq} / (\bar{m}_{atm} g)$ [m]
- From [Lopez \(2017\)](#), the radius of the exobase $R_{exobase} \sim R_p + H \times p_{photo}/p_{XUV}$ [R_\oplus]

where G is the gravitational constant, k_b is the Boltzmann constant, M_p is the planet mass, R_p is the planet radius, \bar{m}_{atm} is the mean molecular mass of the atmosphere, T_{eq} is the equilibrium temperature (assuming the planetary albedo = 0.), and p_{photo} is the transit radius pressure (20 mbar; [Lopez 2017](#)). The approximation of the exobase as the region in which XUV is predominantly absorbed is sensitive to the spectral distribution of incoming stellar radiation, as well as to the composition of the atmosphere. The atmospheric scale height equation is valid only when the atmosphere is largely hydrostatic, because otherwise the vertical velocity of the escaping component ‘stretches’ the scale height (e.g., [Hunten 1973](#)).

Following the determination of these quantities, we estimate the escape regime following ([Owen & Alvarez 2016](#)). In brief, there are three surfaces in stellar flux–planet mass–planet radius phase space that correspond to three different escape regimes: energy-limited, photon-limited, and recombination-limited. Briefly, these regimes correspond to situations in which the escape rate is limited by a particular phenomena ([Owen & Wu 2017](#); [Murray-Clay et al. 2009](#)). The energy-limited escape rate is determined by the plausible upper bound of the amount of energy that could be absorbed and converted into kinetic energy that then drives atmospheric escape. The photon-limited escape rate is derived from the need for ionizing radiation to break up molecules and atoms into smaller and/or charged particles that can then escape. Since the radiation arrives at the top of the atmosphere as a flux of photons that cannot be divided further, there can only be a certain amount of material available for escape at any one time. Lastly, the radiation-recombination limit is moderated by a thin, fully-ionized gas layer in the escaping flow that prevents the further absorption of more energy until some of the dissociated material is allowed to recombine. Generally, the larger the planet or the higher the incoming EUV flux, the more likely the planet is to be in the recombination-limited regime, while smaller planets or those experiencing low EUV fluxes fall into the photon-limited regime.

The individual escape rate parameterizations are taken from literature, and are most often defined in the context of uniform molecular or atomic hydrogen atmospheres, which may not be fully reflected by some of the scenarios described here. The photon-limited escape rate [in kg/s] is defined as:

$$\Phi_{\text{photon}} = \frac{\pi R_p^2 m_H \Phi_{XUV}}{h \bar{\nu}_h}, \quad (\text{A1})$$

where R_p is the planet radius [m], m_H is the mass of a hydrogen atom [kg], Φ_{XUV} is the XUV energy flux received by the planet [W/m^2], and $h \bar{\nu}_h$ is the mean photon energy for photons that heat the upper atmosphere [J/photon].

The radiation-recombination limit [in kg/s] is given by:

$$\Phi_{\text{recombination}} = 7.11 \times 10^4 \Phi_{XUV}^{0.5} R_p^{3/2}, \quad (\text{A2})$$

which comes from [Luger et al. \(2015\)](#), based on the 1-D photoevaporation modeling and resulting parameterization of hot Jupiter atmospheric escape by [Murray-Clay et al. \(2009\)](#) (see [Luger et al.](#) for the derivation). The leading co-factor includes an additional unit conversion to MKS units from CGS units, but is otherwise identical. The equation relates the escape limit to Φ_{XUV} , the XUV energy flux received by the planet [W/m^2], and includes an explicit dependence on the planet's radius (R_p , in meters).

The energy-limited escape rate [in kg/s] is:

$$\Phi_{\text{energy}} = \frac{\eta \Phi_{XUV} R_p R_{\text{exobase}}^2}{G M_p K_{\text{tide}}}, \quad (\text{A3})$$

using the formulation of [Luger & Barnes \(2015\)](#). In this equation, η is the escape efficiency parameter ($0 < \eta < 1$; unit-less), R_p is the radius of the planet [m], R_{exobase} is the radius of the exobase (in m; defined above, following [Lopez 2017](#)), G is the gravitational constant [$\text{m}^3/\text{kg}/\text{s}^2$], M_p is the mass of the planet [m], and K_{tide} is the non-dimensional tidal enhancement factor (taken from [Erkaev et al. 2007](#)), which depends on the Roche lobe radius ($R_{\text{Roche}} = a(M_p/(3M_*))^{1/3}$, in meters) and the planet radius (R_p , in meters) such that

$$K_{\text{tide}} = 1 - \frac{3R_p}{2R_{\text{Roche}}} + \frac{R_p^3}{2R_{\text{Roche}}^3}.$$

Note that this includes the assumption of [Luger & Barnes \(2015\)](#) where the location at which the XUV radiation is absorbed is approximately the planet radius.

We have also added the possibility of entering the diffusion-limited escape regime (e.g., [Kasting & Pollack 1983](#)) when the available hydrogen drops below 1% (assuming that this is the smaller flux of both the energy and diffusion limits; otherwise, we continue to use the energy limit). The threshold value of $\sim 1\%$ roughly corresponds to the transition region between diffusion- and energy-limited escape regimes when the XUV flux is 5-10 times higher than what is received by the Earth ([Kuramoto et al. 2013](#)). The diffusion limit can be a critical hurdle to the complete desiccation of a planet, limiting the supply of water and/or hydrogen to the upper atmosphere via the need to diffuse through the largely static, heavy background gases. The diffusion limit [molecules/ cm^2/s] is defined by [Hunten \(1973\)](#) as:

$$\Phi_{i,\text{diffusion}} = \frac{b_i \xi_i}{(1 + \xi_i)} \left(\frac{1}{H_{\text{heavy}}} - \frac{1}{H_i} \right), \quad (\text{A4})$$

or by expanding the scale height terms and including the dependence on the size of the escaping surface, we see that

$$\Phi'_{i,\text{diffusion}} = 4\pi R_p^2 m_H \frac{b_i g \xi_i (m_{\text{heavy}} - m_i)}{k_b T (1 + \xi_i)} \quad [\text{kg/s}] \quad (\text{A5})$$

This limit exists only when the escaping flux is sufficiently small (in terms of the magnitude of the escape flux) such that the flow does not exceed the crossover mass for other constituents in the atmosphere. Above this limit, the assumption of a stationary heavy gas component is not valid, as the heavy gas is drug off with the escaping component. Determining what additional species are included in the flow is often estimated with the crossover mass ([Hunten et al. 1987](#)):

$$m_c = m_H + \frac{k_b T \Phi_{\text{escape}}}{b g f_H} \quad (\text{A6})$$

where m_H is the mass of the hydrogen atom [kg], k_b is the Boltzmann constant [$\text{m}^2 \text{kg/s}^2/\text{K}$], T is the temperature [K] (taken to be the equilibrium temperature of the planet, a simplification used in lieu the homopause temperature), Φ_{escape} is the escape rate as calculated in the prior step [kg/s], g is the planet's 'surface' gravity [m/s^2], f_H is the total hydrogen atom fraction ($= \xi_{H_2} + 2/3 \times \xi_{H_2O}$, where ξ is the volume mixing ratio of a given species). The total hydrogen fraction calculation combines the assumption that XUV radiation is effective at breaking molecules down into their constituent atoms, and that the new volume mixing ratios of the constituent atoms reflect the composition of the original molecules. This is analogous to the convention defined by b is the generic binary diffusion coefficient for two species from [Banks & Kockarts \(1973\)](#):

$$b = 1.52 \times 10^{20} \left(\frac{m_H}{m_{\text{minor}}} + \frac{m_H}{m_{\text{major}}} \right)^{0.5} T^{0.5} \quad [/\text{m/s}], \quad (\text{A7})$$

where m_{minor} and m_{major} are the molecular masses of the minor (light) species and the major (heavy) species (noting that we assume the heavy species is the mean molecular mass of the species that are not escaping). The crossover mass and the diffusion limit are siblings, such that $\Phi_{\text{escape}} = \Phi_{\text{diffusion}}$ only when $m_c = m_{\text{heavy}}$. The crossover mass represents the upper limit on the 'lifting' action of hydrogen as it escapes, meaning that anything with a smaller atomic weight than the crossover mass can become entrained in the escaping hydrogen and ultimately removed from the planet.

Because the escaping component is not necessarily just hydrogen, the presence of heavier atoms and molecules changes the crossover mass and the flux of escaping material. The first step in our code assumes that the escaping material is atomic hydrogen, and the crossover mass in Eqn. A6 is calculated using just the mass of hydrogen. We then extend the formalism adopted in [Luger & Barnes \(2015, their Section 2.4.2\)](#), defining the flux of each species in relation to the flux of hydrogen and the crossover mass:

$$\Phi_x = \frac{\xi_x}{f_H} \Phi_H \left(\frac{m_c - m_x}{m_c - m_H} \right) \text{ if } m_c > m_x; = 0 \text{ otherwise.} \quad (\text{A8})$$

Note that an implicit assumption here is that there are sufficient photons to completely dissociate any hydrogen-bearing species, such that $\xi_H \cong f_H$. To calculate the flux of each species in the escaping flow, we can generalize Eqn. 6 of [Luger & Barnes \(2015\)](#):

$$m_H \Phi_H^{\text{ref}} = \sum_x^{m_x < m_c} m_x \Phi_x. \quad (\text{A9})$$

We can then follow the same derivation as [Luger & Barnes \(2015\)](#), which will result in a crossover mass that accommodates more than one other gas. Substituting Eqn. A8 into this relationship, we see that:

$$m_H \Phi_H^{\text{ref}} = \sum_x^{m_x < m_c} m_x \frac{\xi_x}{f_H} \Phi_H \left(\frac{m_c - m_x}{m_c - m_H} \right) \quad (\text{A10})$$

$$= \frac{\Phi_H}{(m_c - m_H) f_H} \sum_x^{m_x < m_c} m_x \xi_x (m_c - m_x) \quad (\text{A11})$$

$$\frac{\Phi_H}{m_H f_H} = \Phi_H^{\text{ref}} (m_c - m_H) \left[\sum_x^{m_x < m_c} m_x \xi_x (m_c - m_x) \right]^{-1} \quad (\text{A12})$$

If we substitute this expression back into Eqn. A6:

$$m_c = m_H + m_H \frac{k_b T \Phi_H^{\text{ref}}}{bg} (m_c - m_H) \left[\sum_x^{m_x < m_c} m_x \xi_x (m_c - m_x) \right]^{-1} \quad (\text{A13})$$

$$\frac{m_c - m_H}{m_H} = \frac{k_b T \Phi_H^{\text{ref}}}{bg} (m_c - m_H) \left[\sum_x^{m_x < m_c} m_x \xi_x (m_c - m_x) \right]^{-1} \quad (\text{A14})$$

$$\frac{1}{m_H} = \frac{k_b T \Phi_H^{\text{ref}}}{bg} \left[\sum_x^{m_x < m_c} m_x \xi_x (m_c - m_x) \right]^{-1} \quad (\text{A15})$$

$$\sum_x^{m_x < m_c} m_x \xi_x (m_c - m_x) = \frac{k_b T \Phi_H^{\text{ref}} m_H}{bg} \quad (\text{A16})$$

$$\sum_x^{m_x < m_c} m_x \xi_x m_c - \sum_x^{m_x < m_c} m_x \xi_x m_x = \frac{k_b T \Phi_H^{\text{ref}} m_H}{bg} \quad (\text{A17})$$

$$m_c \sum_x^{m_x < m_c} m_x \xi_x = \frac{k_b T \Phi_H^{\text{ref}} m_H}{bg} + \sum_x^{m_x < m_c} m_x \xi_x m_x \quad (\text{A18})$$

$$m_c = \left[\sum_x^{m_x < m_c} m_x \xi_x \right]^{-1} \left(\frac{k_b T \Phi_H^{\text{ref}} m_H}{bg} + \sum_x^{m_x < m_c} m_x \xi_x m_x \right) \quad (\text{A19})$$

As the sum of the mixing-ratio-weighted molecular masses gives the mean molecular mass, this expression simplifies to:

$$m_c = \frac{k_b T \Phi_H^{\text{ref}} m_H}{bg \bar{\mu}} + \frac{m_H}{\bar{\mu}} \sum_x^{m_x < m_c} m_x \xi_x \mu_x \quad (\text{A20})$$

In our code, we describe m_c in amu, not kg, which is the same as above once m_H has been divided out of both sides of the equation.

We estimate escape and the changing mean molecular weight of the flow by sequentially including each potential species in reverse order by mass (in our modeling, this would be helium, then atomic oxygen, then water, and so on). Each sequential addition forces us to check whether the new crossover mass (which has a slower relative flux but higher mean molecular weight) is still in excess of the molecular mass of the next-heaviest component, only exiting if this is not the case. Because the additional species is added before the crossover mass is calculated, the last loop exits without updating the crossover mass, ensuring that all the incorporated species are represented without adding a repeated term. Subsequent to this loop, the revised escape fluxes are computed (per Eqn. A8). Then the escaping mass is removed from the relevant inventories such that, if no hydrogen remains in the atmosphere, the hydrogen escape is subtracted from the water inventory (leaving behind the oxygen atoms), and any resulting negative inventories are instead set to zero and the remainder of the mass removed as hydrogen (using the same relationship in Eqn. A8).

DETERMINING THE ESCAPE REGIME

As noted by [Owen & Alvarez \(2016\)](#), there is no closed form of the equations governing which regime a planet would fall into, and so the boundaries of each regime must be solved for at each time step as a function of instellation and planet mass and radius. The three equations (#18, 19, and 20 from [Owen & Alvarez 2016](#)) are:

$$M_p = \eta \left(\frac{h \bar{\nu}_h}{4Gm_H} \right) R_p \quad (\text{A21})$$

$$W_0 \left[- \left(\frac{R_p}{R_s} \right)^{-4} \exp \left(3 - \frac{4R_s}{R_p} \right) \right] = \frac{-J_0 \alpha_B H}{4c_s^2} \quad (\text{A22})$$

$$W_0 \left[- \left(\frac{R_p}{R_s} \right)^{-4} \exp \left(3 - \frac{4R_s}{R_p} \right) \right] = \frac{-\eta J_0 \alpha_B H}{4c_s^2} \times \left(\frac{R_p h \bar{\nu}_h}{4GM_p m_H} \right) \quad (\text{A23})$$

where M_p is the planet mass, η is the escape efficiency parameter ($0 < \eta < 1$), $h\bar{\nu}_h$ is the mean photon energy for photons that heat the upper atmosphere, G is the gravitational constant, m_H is the mass of a hydrogen atom, R_p is the planet radius, W_0 is the Lambert W function (the Lambert W function is the set of solutions to $W(x)\exp(W(x)) = x$, and W_0 is the principal branch such that x and $W(x)$ are real numbers; we use the Python function `lambertw()` from the `scipy.special` library), R_s is the sonic point (given by $GM_p/(2c_s^2)$), J_0 is the ionizing photon flux, α_B is the case-B recombination coefficient ($= 2.6 \times 10^{-13} \text{ cm}^3 \text{ s}^{-1} (T/10^4)^{-0.7}$, taking T to be the exospheric temperature) acting as a stand-in for the recombination rate, H is the atmospheric scale height, and c_s is the sound speed ($c_s^2 = k_b T / (\bar{m}_{atm})$, with \bar{m}_{atm} defined as before to be the mean molecular mass of the atmosphere). Note that we include the additional parentheses to clarify exponentiation, following [Cranmer \(2004\)](#). The exospheric temperature, as described in the text, is set to either 10^4 K or 2000 K based on the incoming XUV flux, with a threshold of $\sim 180 \text{ erg cm}^{-2} \text{ s}^{-1}$ forcing a higher exospheric temperature when H_3^+ cooling becomes ineffective ([Koskinen et al. 2007](#); [Murray-Clay et al. 2009](#)).

Equation [A21](#) defines the boundary between the photon- and energy-limited escape regimes, while Equation [A22](#) is for the recombination- and photon-limited regimes, and Equation [A23](#) is for the recombination- and energy-limited regimes. Both Eqns. [A22](#) and [A23](#) have either two solutions or none, if describing the system in mass-radius space (as shown by [Owen & Alvarez 2016](#)), but since we have chosen a planet mass and radius as part of our initial conditions, this collapses the three equations down to one or no solution that is solely a function of the ionizing flux. We calculate J_0 by rearranging Eqns. [A22](#) and [A23](#) to solve for J_0 , which we then compare against the stellar XUV flux calculated in the setup step. The boundary between energy- and photon-limited escape is in the form of planet mass, such that a planet more massive than the threshold mass (the left-hand side of Eqn. [A21](#)) will be in the energy- or recombination-limited regime. If the planet's mass is instead below the threshold and the XUV flux is below the recombination- and photon-limited threshold flux, the escape is in the photon-limited regime.

RUN_ESCAPE - RETURNING VALUES TO MONTE_CARLO.PY

The code currently returns summary statistics for individual runs to `monte_carlo.py`, including the planet's mass, radius, core mass fraction, envelope fraction and composition, and total mass change over the duration of the simulation (this is always longer than the estimated age of the host star in this parameter sweep). Individual time evolution data is not returned, in an effort to provide manageable data volumes and run times; by default, the simulations have 3,000 points across the whole of the available stellar evolution data, and only returning 3 of each of the reported parameters is a thousand-fold reduction in data.

B. PHOTOCHEMICAL REACTION LIST AND THERMODYNAMIC DATA

Table 3. Reactions and rates.

Rxn #	Reaction	Rate	Notes
1	$\text{H} + \text{H}_2\text{O} \rightarrow \text{OH} + \text{H}_2$	$7.500 \times 10^{-16} \cdot T^{1.60} \cdot \exp(-9720/\text{T})$	1
3	$\text{O} + \text{H}_2 \rightarrow \text{OH} + \text{H}$	$8.520 \times 10^{-20} \cdot T^{2.67} \cdot \exp(-3160/\text{T})$	1
5	$\text{O} + \text{H}_2\text{O} \rightarrow \text{OH} + \text{OH}$	$8.200 \times 10^{-14} \cdot T^{0.95} \cdot \exp(-8570/\text{T})$	1
7	$\text{H} + \text{CH} \rightarrow \text{H}_2 + \text{C}$	$1.310 \times 10^{-10} \cdot \exp(-80/\text{T})$	1
9	$\text{H} + \text{CH}_2 \rightarrow \text{CH} + \text{H}_2$	$1.000 \times 10^{-11} \cdot \exp(900/\text{T})$	1
11	$\text{CH}_2 + \text{H}_2 \rightarrow \text{H} + \text{CH}_3$	$7.320 \times 10^{-19} \cdot T^{2.30} \cdot \exp(-3699/\text{T})$	1
13	$\text{H} + \text{CH}_4 \rightarrow \text{CH}_3 + \text{H}_2$	$2.200 \times 10^{-20} \cdot T^{3.00} \cdot \exp(-4040/\text{T})$	1
15	$\text{C} + \text{CH} \rightarrow \text{C}_2 + \text{H}$	$1.050 \times 10^{-12} \cdot T^{0.50}$	1
17	$\text{H}_2 + \text{C}_2\text{H} \rightarrow \text{H} + \text{C}_2\text{H}_2$	$9.200 \times 10^{-18} \cdot T^{2.17} \cdot \exp(-478/\text{T})$	1
19	$\text{CH} + \text{CH}_2 \rightarrow \text{H} + \text{C}_2\text{H}_2$	6.640×10^{-11}	1
21	$\text{H} + \text{C}_2\text{H}_3 \rightarrow \text{C}_2\text{H}_2 + \text{H}_2$	2.010×10^{-11}	1
23	$\text{H}_2 + \text{C}_2\text{H}_3 \rightarrow \text{H} + \text{C}_2\text{H}_4$	$5.000 \times 10^{-20} \cdot T^{2.63} \cdot \exp(-4300/\text{T})$	1
25	$\text{CH} + \text{CH}_4 \rightarrow \text{H} + \text{C}_2\text{H}_4$	$5.000 \times 10^{-11} \cdot \exp(200/\text{T})$	1
27	$\text{CH}_2 + \text{CH}_3 \rightarrow \text{H} + \text{C}_2\text{H}_4$	7.010×10^{-11}	1
29	$\text{H} + \text{C}_2\text{H}_5 \rightarrow \text{CH}_3 + \text{CH}_3$	5.990×10^{-11}	1
31	$\text{H} + \text{C}_2\text{H}_5 \rightarrow \text{C}_2\text{H}_4 + \text{H}_2$	3.010×10^{-12}	1
33	$\text{H} + \text{C}_2\text{H}_6 \rightarrow \text{C}_2\text{H}_5 + \text{H}_2$	$9.190 \times 10^{-22} \cdot T^{3.50} \cdot \exp(-2600/\text{T})$	1
35	$\text{OH} + \text{CO} \rightarrow \text{H} + \text{CO}_2$	$1.050 \times 10^{-17} \cdot T^{1.50} \cdot \exp(259/\text{T})$	1
37	$\text{CH} + \text{CH}_3 \rightarrow \text{H}_2 + \text{C}_2\text{H}_2$	1.000×10^{-11}	1
39	$\text{C}_2 + \text{O} \rightarrow \text{C} + \text{CO}$	1.050×10^{-12}	1
41	$\text{CH}_2 + \text{CH}_2 \rightarrow \text{C}_2\text{H}_2 + \text{H} + \text{H}$	$1.800 \times 10^{-10} \cdot \exp(-400/\text{T})$	1
43	$\text{CH}_2 + \text{CH}_2 \rightarrow \text{CH} + \text{CH}_3$	$3.980 \times 10^{-10} \cdot \exp(-5000/\text{T})$	1
45	$\text{CH}_2 + \text{CH}_2 \rightarrow \text{H} + \text{C}_2\text{H}_3$	3.320×10^{-11}	1
47	$\text{CH}_2 + \text{CH}_4 \rightarrow \text{CH}_3 + \text{CH}_3$	$4.090 \times 10^{-18} \cdot T^{2.00} \cdot \exp(-4162/\text{T})$	1
49	$\text{CH}_2 + \text{C}_2\text{H}_5 \rightarrow \text{CH}_3 + \text{C}_2\text{H}_4$	3.010×10^{-11}	1
51	$\text{CH}_3 + \text{OH} \rightarrow \text{CH}_2 + \text{H}_2\text{O}$	$1.850 \times 10^{-21} \cdot T^{3.00} \cdot \exp(-1400/\text{T})$	1
53	$\text{C}_2\text{H} + \text{OH} \rightarrow \text{CH}_2 + \text{CO}$	3.010×10^{-11}	1
55	$\text{C}_2\text{H}_2 + \text{O} \rightarrow \text{CH}_2 + \text{CO}$	$6.780 \times 10^{-16} \cdot T^{1.50} \cdot \exp(-854/\text{T})$	1
57	$\text{CH}_3 + \text{C}_2\text{H} \rightarrow \text{C}_2\text{H}_2 + \text{CH}_2$	1.000×10^{-11}	1
59	$\text{CH}_4 + \text{C}_2\text{H} \rightarrow \text{CH}_3 + \text{C}_2\text{H}_2$	$3.010 \times 10^{-12} \cdot \exp(-250/\text{T})$	1
61	$\text{CH}_3 + \text{C}_2\text{H}_3 \rightarrow \text{CH}_4 + \text{C}_2\text{H}_2$	6.510×10^{-13}	1
63	$\text{CH}_4 + \text{C}_2\text{H}_3 \rightarrow \text{CH}_3 + \text{C}_2\text{H}_4$	$2.130 \times 10^{-24} \cdot T^{4.02} \cdot \exp(-2754/\text{T})$	1
65	$\text{CH}_3 + \text{C}_2\text{H}_5 \rightarrow \text{CH}_4 + \text{C}_2\text{H}_4$	$3.250 \times 10^{-11} \cdot T^{-0.50}$	1
67	$\text{CH}_3 + \text{C}_2\text{H}_6 \rightarrow \text{CH}_4 + \text{C}_2\text{H}_5$	$9.120 \times 10^{-25} \cdot T^{4.00} \cdot \exp(-4170/\text{T})$	1
69	$\text{C}_2\text{H}_2 + \text{OH} \rightarrow \text{CH}_3 + \text{CO}$	$8.040 \times 10^{-28} \cdot T^{4.00} \cdot \exp(1010/\text{T})$	1
71	$\text{C}_2 + \text{H}_2 \rightarrow \text{H} + \text{C}_2\text{H}$	$1.100 \times 10^{-10} \cdot \exp(-4000/\text{T})$	1
73	$\text{C}_2 + \text{CH}_4 \rightarrow \text{CH}_3 + \text{C}_2\text{H}$	$5.050 \times 10^{-11} \cdot \exp(-297/\text{T})$	1
75	$\text{C}_2\text{H} + \text{CH}_2 \rightarrow \text{CH} + \text{C}_2\text{H}_2$	3.010×10^{-11}	1
77	$\text{C}_2\text{H} + \text{C}_2\text{H}_6 \rightarrow \text{C}_2\text{H}_2 + \text{C}_2\text{H}_5$	5.990×10^{-12}	1
79	$\text{C}_2\text{H} + \text{O} \rightarrow \text{CH} + \text{CO}$	1.690×10^{-11}	1
81	$\text{C}_2\text{H} + \text{OH} \rightarrow \text{C}_2\text{H}_2 + \text{O}$	3.010×10^{-11}	1
83	$\text{C}_2\text{H} + \text{H}_2\text{O} \rightarrow \text{C}_2\text{H}_2 + \text{OH}$	$2.200 \times 10^{-21} \cdot T^{3.05} \cdot \exp(-376/\text{T})$	1
85	$\text{C}_2\text{H}_3 + \text{C}_2\text{H}_3 \rightarrow \text{C}_2\text{H}_4 + \text{C}_2\text{H}_2$	1.600×10^{-12}	1
87	$\text{C}_2\text{H}_3 + \text{C}_2\text{H}_5 \rightarrow \text{C}_2\text{H}_4 + \text{C}_2\text{H}_4$	8.000×10^{-13}	1
89	$\text{C}_2\text{H}_3 + \text{C}_2\text{H}_5 \rightarrow \text{C}_2\text{H}_6 + \text{C}_2\text{H}_2$	8.000×10^{-13}	1
91	$\text{C}_2\text{H}_4 + \text{OH} \rightarrow \text{C}_2\text{H}_3 + \text{H}_2\text{O}$	$2.600 \times 10^{-20} \cdot T^{2.75} \cdot \exp(-2100/\text{T})$	1

Rxn #	Reaction	Rate	Notes
93	$\text{C}_2\text{H}_5 + \text{C}_2\text{H}_5 \rightarrow \text{C}_2\text{H}_4 + \text{C}_2\text{H}_6$	2.310×10^{-12}	1
95	$\text{C}_2\text{H}_5 + \text{C}_2\text{H}_4 \rightarrow \text{C}_2\text{H}_3 + \text{C}_2\text{H}_6$	$1.050 \times 10^{-21} \cdot T^{3.13} \cdot \exp(-9060/T)$	1
97	$\text{C}_2\text{H}_6 + \text{OH} \rightarrow \text{C}_2\text{H}_5 + \text{H}_2\text{O}$	$1.470 \times 10^{-14} \cdot T^{1.04} \cdot \exp(-913/T)$	1
99	$\text{CH} + \text{O} \rightarrow \text{OH} + \text{C}$	$2.520 \times 10^{-11} \cdot \exp(-2381/T)$	1
101	$\text{O} + \text{CH} \rightarrow \text{H} + \text{CO}$	6.590×10^{-11}	1
103	$\text{O} + \text{CH}_3 \rightarrow \text{CH}_2 + \text{OH}$	$1.000 \times 10^{-11} \cdot \exp(-3970/T)$	1
105	$\text{CH}_3 + \text{OH} \rightarrow \text{O} + \text{CH}_4$	$1.160 \times 10^{-19} \cdot T^{2.20} \cdot \exp(-2240/T)$	1
107	$\text{O} + \text{C}_2\text{H}_6 \rightarrow \text{OH} + \text{C}_2\text{H}_5$	$2.000 \times 10^{-12} \cdot T^{0.60} \cdot \exp(-3680/T)$	1
109	$\text{OH} + \text{C} \rightarrow \text{CO} + \text{H}$	$1.050 \times 10^{-12} \cdot T^{0.50}$	1
111	$\text{OH} + \text{CH}_2 \rightarrow \text{H}_2\text{O} + \text{CH}$	$1.430 \times 10^{-18} \cdot T^{2.02} \cdot \exp(-3410/T)$	1
113	$\text{OH} + \text{CH}_4 \rightarrow \text{H}_2\text{O} + \text{CH}_3$	$3.190 \times 10^{-19} \cdot T^{2.40} \cdot \exp(-1060/T)$	1
115	$\text{OH} + \text{C}_2\text{H}_3 \rightarrow \text{H}_2\text{O} + \text{C}_2\text{H}_2$	5.000×10^{-11}	1
117	$\text{OH} + \text{C}_2\text{H}_5 \rightarrow \text{H}_2\text{O} + \text{C}_2\text{H}_4$	4.000×10^{-11}	1
119	$\text{CH}_2\text{OH} + \text{H} \rightarrow \text{OH} + \text{CH}_3$	1.600×10^{-10}	1
121	$\text{H}_2\text{CO} + \text{H} \rightarrow \text{HCO} + \text{H}_2$	$3.640 \times 10^{-16} \cdot T^{1.77} \cdot \exp(-1510/T)$	1
123	$\text{O} + \text{C}_2\text{H}_4 \rightarrow \text{HCO} + \text{CH}_3$	$2.190 \times 10^{-16} \cdot T^{1.55} \cdot \exp(-215/T)$	1
125	$\text{H}_2\text{CO} + \text{CH}_3 \rightarrow \text{CH}_4 + \text{HCO}$	$9.200 \times 10^{-21} \cdot T^{2.81} \cdot \exp(-2950/T)$	1
127	$\text{CH}_3 + \text{CH}_2\text{OH} \rightarrow \text{H}_2\text{CO} + \text{CH}_4$	4.000×10^{-12}	1
129	$\text{HCO} + \text{H} \rightarrow \text{CO} + \text{H}_2$	1.500×10^{-10}	1
131	$\text{HCO} + \text{OH} \rightarrow \text{CO} + \text{H}_2\text{O}$	1.690×10^{-10}	1
133	$\text{CO}_2 + \text{CH} \rightarrow \text{HCO} + \text{CO}$	$5.710 \times 10^{-12} \cdot \exp(-345/T)$	1
135	$\text{CH}_3 + \text{O} \rightarrow \text{H}_2\text{CO} + \text{H}$	1.400×10^{-10}	1
137	$\text{CH}_3\text{O} + \text{O} \rightarrow \text{H}_2\text{CO} + \text{OH}$	1.000×10^{-11}	1
139	$\text{CH}_3\text{O} + \text{OH} \rightarrow \text{H}_2\text{CO} + \text{H}_2\text{O}$	3.010×10^{-11}	1
141	$\text{CH}_3\text{OH} + \text{H} \rightarrow \text{CH}_3\text{O} + \text{H}_2$	$6.820 \times 10^{-20} \cdot T^{2.69} \cdot \exp(-4643/T)$	1
143	$\text{CH}_3\text{OH} + \text{H} \rightarrow \text{CH}_3 + \text{H}_2\text{O}$	$4.910 \times 10^{-19} \cdot T^{2.49} \cdot \exp(-10380/T)$	1
145	$\text{CH}_2 + \text{O} \rightarrow \text{CO} + \text{H} + \text{H}$	1.330×10^{-10}	1
147	$\text{CH}_2 + \text{OH} \rightarrow \text{H}_2\text{CO} + \text{H}$	3.010×10^{-11}	1
149	$\text{CO}_2 + \text{CH}_2 \rightarrow \text{H}_2\text{CO} + \text{CO}$	3.900×10^{-14}	1
151	$\text{CH}_3\text{O} + \text{CO} \rightarrow \text{CH}_3 + \text{CO}_2$	$2.610 \times 10^{-11} \cdot \exp(-5940/T)$	1
153	$\text{CH}_3\text{OH} + \text{H} \rightarrow \text{CH}_2\text{OH} + \text{H}_2$	$1.090 \times 10^{-19} \cdot T^{2.73} \cdot \exp(-2240/T)$	1
155	$\text{HCO} + \text{C}_2\text{H} \rightarrow \text{C}_2\text{H}_2 + \text{CO}$	1.000×10^{-10}	1
157	$\text{CH}_2\text{OH} + \text{C}_2\text{H} \rightarrow \text{H}_2\text{CO} + \text{C}_2\text{H}_2$	5.990×10^{-11}	1
159	$\text{CH}_3\text{O} + \text{C}_2\text{H} \rightarrow \text{H}_2\text{CO} + \text{C}_2\text{H}_2$	4.000×10^{-11}	1
161	$\text{CH}_3\text{OH} + \text{C}_2\text{H} \rightarrow \text{CH}_2\text{OH} + \text{C}_2\text{H}_2$	1.000×10^{-11}	1
163	$\text{CH}_3\text{OH} + \text{C}_2\text{H} \rightarrow \text{CH}_3\text{O} + \text{C}_2\text{H}_2$	2.010×10^{-12}	1
165	$\text{O} + \text{C}_2\text{H}_3 \rightarrow \text{C}_2\text{H}_2 + \text{OH}$	$1.760 \times 10^{-12} \cdot T^{0.20} \cdot \exp(215/T)$	1
167	$\text{CH}_2 + \text{C}_2\text{H}_3 \rightarrow \text{C}_2\text{H}_2 + \text{CH}_3$	3.000×10^{-11}	1
169	$\text{O} + \text{CH}_2 \rightarrow \text{CO} + \text{H}_2$	9.960×10^{-11}	1
171	$\text{O} + \text{C}_2\text{H}_3 \rightarrow \text{HCO} + \text{CH}_2$	2.000×10^{-11}	1
173	$\text{HCO} + \text{CH}_2 \rightarrow \text{CO} + \text{CH}_3$	3.010×10^{-11}	1
175	$\text{O} + \text{C}_2\text{H}_4 \rightarrow \text{H}_2\text{CO} + \text{CH}_2$	$1.350 \times 10^{-17} \cdot T^{1.80} \cdot \exp(-90/T)$	1
177	$\text{CH}_2\text{OH} + \text{CH}_2 \rightarrow \text{OH} + \text{C}_2\text{H}_4$	4.000×10^{-11}	1
179	$\text{CH}_2\text{OH} + \text{CH}_2 \rightarrow \text{H}_2\text{CO} + \text{CH}_3$	2.010×10^{-12}	1
181	$\text{CH}_3\text{O} + \text{CH}_2 \rightarrow \text{H}_2\text{CO} + \text{CH}_3$	3.000×10^{-11}	1
183	$\text{CH}_3\text{OH} + \text{CH}_2 \rightarrow \text{CH}_3\text{O} + \text{CH}_3$	$2.390 \times 10^{-23} \cdot T^{3.10} \cdot \exp(-3490/T)$	1
185	$\text{CH}_3\text{OH} + \text{CH}_2 \rightarrow \text{CH}_2\text{OH} + \text{CH}_3$	$5.290 \times 10^{-23} \cdot T^{3.20} \cdot \exp(-3609/T)$	1
187	$\text{HCO} + \text{CH}_3 \rightarrow \text{CO} + \text{CH}_4$	2.010×10^{-10}	1
189	$\text{CH}_3\text{O} + \text{CH}_3 \rightarrow \text{H}_2\text{CO} + \text{CH}_4$	4.000×10^{-11}	1

Rxn #	Reaction	Rate	Notes
191	$\text{H}_2\text{CO} + \text{CH} \rightarrow \text{CO} + \text{CH}_3$	$8.000 \times 10^{-11} \cdot \exp(260/\text{T})$	1
193	$\text{CH}_3\text{OH} + \text{CH}_3 \rightarrow \text{CH}_3\text{O} + \text{CH}_4$	$2.390 \times 10^{-23} \cdot T^{3.10} \cdot \exp(-3490/\text{T})$	1
195	$\text{CH}_3\text{CO} + \text{H} \rightarrow \text{HCO} + \text{CH}_3$	3.320×10^{-11}	1
197	$\text{CH}_3\text{CO} + \text{CH}_3 \rightarrow \text{CO} + \text{C}_2\text{H}_6$	4.900×10^{-11}	1
199	$\text{O} + \text{OH} \rightarrow \text{O}_2 + \text{H}$	$7.470 \times 10^{-10} \cdot T^{-0.50} \cdot \exp(-30/\text{T})$	1
201	$\text{H} + \text{CH}_3\text{O} \rightarrow \text{H}_2\text{CO} + \text{H}_2$	3.010×10^{-11}	1
203	$\text{H} + \text{CH}_2\text{CO} \rightarrow \text{CO} + \text{CH}_3$	$1.290 \times 10^{-15} \cdot T^{1.45} \cdot \exp(-1399/\text{T})$	1
205	$\text{O} + \text{C}_2\text{H}_3 \rightarrow \text{CH}_2\text{CO} + \text{H}$	1.600×10^{-10}	1
207	$\text{C}_2\text{H}_2 + \text{O} \rightarrow \text{HCCO} + \text{H}$	$1.500 \times 10^{-11} \cdot \exp(-2280/\text{T})$	1
209	$\text{HCCO} + \text{H} \rightarrow \text{CO} + \text{CH}_2$	2.490×10^{-10}	1
211	$\text{O} + \text{H}_2\text{CO} \rightarrow \text{HCO} + \text{OH}$	$6.850 \times 10^{-13} \cdot T^{0.57} \cdot \exp(-1390/\text{T})$	1
213	$\text{HCO} + \text{HCO} \rightarrow \text{H}_2\text{CO} + \text{CO}$	3.010×10^{-11}	1
215	$\text{CH}_2\text{OH} + \text{CH}_3\text{O} \rightarrow \text{H}_2\text{CO} + \text{CH}_3\text{OH}$	4.000×10^{-11}	1
217	$\text{CH}_3\text{O} + \text{CH}_3\text{O} \rightarrow \text{H}_2\text{CO} + \text{CH}_3\text{OH}$	1.000×10^{-10}	1
219	$\text{H} + \text{H} \rightarrow \text{H}_2 + \text{M}$	$k_0 = 2.700 \times 10^{-31} \cdot T^{-0.60}$ $k_\infty = 3.310 \times 10^{-06} \cdot T^{-1.00}$	2
221	$\text{H} + \text{O} \rightarrow \text{OH} + \text{M}$	$k_0 = 1.300 \times 10^{-29} \cdot T^{-1.00}$ $k_\infty = 1.000 \times 10^{-11}$	2
223	$\text{OH} + \text{H} \rightarrow \text{H}_2\text{O} + \text{M}$	$k_0 = 3.890 \times 10^{-25} \cdot T^{-2.00}$ $k_\infty = 4.260 \times 10^{-11} \cdot T^{0.23}$	2
225	$\text{H} + \text{CH} \rightarrow \text{CH}_2 + \text{M}$	$k_0 = 2.760 \times 10^{-29} \cdot T^{-1.00}$ $k_\infty = 1.000 \times 10^{-12}$	2
227	$\text{H} + \text{CH}_3 \rightarrow \text{CH}_4 + \text{M}$	$k_0 = 1.760 \times 10^{-24} \cdot T^{-1.80}$ $k_\infty = 2.060 \times 10^{-10} \cdot T^{-0.40}$	2
229	$\text{H} + \text{C}_2\text{H}_2 \rightarrow \text{C}_2\text{H}_3 + \text{M}$	$k_0 = 1.050 \times 10^{-07} \cdot T^{-7.27} \cdot \exp(-3630/\text{T})$ $k_\infty = 9.130 \times 10^{-12} \cdot \exp(-3630/\text{T})$	2
231	$\text{H} + \text{C}_2\text{H}_3 \rightarrow \text{C}_2\text{H}_4 + \text{M}$	$k_0 = 1.500 \times 10^{-27}$ $k_\infty = 6.400 \times 10^{-11} \cdot T^{0.20}$	2
233	$\text{H} + \text{C}_2\text{H}_4 \rightarrow \text{C}_2\text{H}_5 + \text{M}$	$k_0 = 7.690 \times 10^{-30} \cdot \exp(-380/\text{T})$ $k_\infty = 1.270 \times 10^{-15} \cdot T^{1.49} \cdot \exp(-380/\text{T})$	2
235	$\text{H} + \text{C}_2\text{H}_5 \rightarrow \text{C}_2\text{H}_6 + \text{M}$	$k_0 = 4.000 \times 10^{-19} \cdot T^{-3.00} \cdot \exp(-600/\text{T})$ $k_\infty = 9.040 \times 10^{-11} \cdot T^{0.16} \cdot \exp(-600/\text{T})$	2
237	$\text{H}_2 + \text{C} \rightarrow \text{CH}_2 + \text{M}$	$k_0 = 6.890 \times 10^{-32}$ $k_\infty = 2.060 \times 10^{-11}$	2
239	$\text{CH} + \text{M} \rightarrow \text{C} + \text{H} + \text{M}$	$k_0 = 3.160 \times 10^{-10} \cdot \exp(-33700/\text{T})$ $k_\infty = 1.000 \times 10^{-12} \cdot \exp(-33700/\text{T})$	2
241	$\text{CH}_2 + \text{H} \rightarrow \text{CH}_3 + \text{M}$	$k_0 = 9.000 \times 10^{-32} \cdot \exp(550/\text{T})$ $k_\infty = 8.550 \times 10^{-12} \cdot T^{0.15} \cdot \exp(550/\text{T})$	2
243	$\text{CH} + \text{H}_2 \rightarrow \text{CH}_3 + \text{M}$	$k_0 = 3.400 \times 10^{-31} \cdot \exp(736/\text{T})$ $k_\infty = 7.300 \times 10^{-11} \cdot \exp(736/\text{T})$	2
245	$\text{CH}_3 + \text{CH}_3 \rightarrow \text{C}_2\text{H}_6 + \text{M}$	$k_0 = 3.500 \times 10^{-07} \cdot T^{-7.00} \cdot \exp(-1390/\text{T})$ $k_\infty = 1.580 \times 10^{-09} \cdot T^{-0.54} \cdot \exp(-1390/\text{T})$	2
247	$\text{C}_2\text{H} + \text{H} \rightarrow \text{C}_2\text{H}_2 + \text{M}$	$k_0 = 1.260 \times 10^{-18} \cdot T^{-3.10} \cdot \exp(-721/\text{T})$ $k_\infty = 3.000 \times 10^{-10} \cdot \exp(-721/\text{T})$	2
249	$\text{C}_2\text{H}_4 + \text{M} \rightarrow \text{C}_2\text{H}_2 + \text{H}_2 + \text{M}$	$k_0 = 5.800 \times 10^{-08} \cdot \exp(-36000/\text{T})$ $k_\infty = 7.950 \times 10^{+12} \cdot T^{0.44} \cdot \exp(-36000/\text{T})$	2
251	$\text{C}_2\text{H}_6 + \text{M} \rightarrow \text{C}_2\text{H}_4 + \text{H}_2 + \text{M}$	$k_0 = 3.800 \times 10^{-07} \cdot \exp(-34000/\text{T})$ $k_\infty = 1.320 \times 10^{+15} \cdot \exp(-34000/\text{T})$	2

Rxn #	Reaction	Rate	Notes
253	$\text{CO} + \text{O} \rightarrow \text{CO}_2 + \text{M}$	$\left\{ \begin{array}{l} k_0 = 1.700 \times 10^{-33} \cdot \exp(-1510/\text{T}) \\ k_\infty = 2.660 \times 10^{-14} \cdot \exp(-1510/\text{T}) \end{array} \right.$	2
255	$\text{CH}_2\text{OH} + \text{M} \rightarrow \text{H} + \text{H}_2\text{CO} + \text{M}$		2
257	$\text{H} + \text{CO} \rightarrow \text{HCO} + \text{M}$	$\left\{ \begin{array}{l} k_0 = 5.290 \times 10^{-34} \cdot \exp(-370/\text{T}) \\ k_\infty = 1.960 \times 10^{-13} \cdot \exp(-370/\text{T}) \\ k_0 = 1.000 \times 10^{-31} \\ k_\infty = 9.480 \times 10^{-12} \\ k_0 = 9.000 \times 10^{-11} \cdot \exp(-6790/\text{T}) \\ k_\infty = 1.560 \times 10^{+15} \cdot T^{-0.39} \cdot \exp(-6790/\text{T}) \\ k_0 = 1.200 \times 10^{-16} \cdot T^{-4.65} \cdot \exp(-2557/\text{T}) \\ k_\infty = 2.300 \times 10^{-10} \cdot T^{0.04} \cdot \exp(-2557/\text{T}) \\ k_0 = 4.990 \times 10^{-25} \cdot T^{-2.00} \\ k_\infty = 1.060 \times 10^{-07} \cdot T^{-1.90} \end{array} \right.$	2
259	$\text{H}_2\text{O} + \text{CH} \rightarrow \text{CH}_2\text{OH} + \text{M}$		2
261	$\text{CH}_3\text{O} + \text{M} \rightarrow \text{H} + \text{H}_2\text{CO} + \text{M}$		2
263	$\text{CH}_2\text{OH} + \text{H} \rightarrow \text{CH}_3\text{OH} + \text{M}$		2
265	$\text{OH} + \text{C}_2\text{H}_2 \rightarrow \text{CH}_3\text{CO} + \text{M}$		2
267	$\text{CO} + \text{CH}_3 \rightarrow \text{CH}_3\text{CO} + \text{M}$	$\left\{ \begin{array}{l} k_0 = 3.950 \times 10^{-10} \cdot T^{-7.50} \cdot \exp(-5490/\text{T}) \\ k_\infty = 5.140 \times 10^{-19} \cdot T^{2.20} \cdot \exp(-5490/\text{T}) \\ k_0 = 7.330 \times 10^{-24} \cdot T^{-2.57} \cdot \exp(-215/\text{T}) \\ k_\infty = 7.770 \times 10^{-14} \cdot \exp(-215/\text{T}) \\ k_0 = 2.800 \times 10^{-20} \cdot T^{-3.42} \cdot \exp(-42450/\text{T}) \\ k_\infty = 7.140 \times 10^{-17} \cdot T^{1.50} \cdot \exp(-42450/\text{T}) \\ k_0 = 4.370 \times 10^{-04} \cdot T^{-8.20} \\ k_\infty = 1.000 \times 10^{-10} \\ 4.970 \times 10^{-27} \cdot T^{-1.60} \end{array} \right.$	2
269	$\text{HCO} + \text{H} \rightarrow \text{H}_2\text{CO} + \text{M}$		2
271	$\text{CO} + \text{H}_2 \rightarrow \text{H}_2\text{CO} + \text{M}$		2
273	$\text{OH} + \text{CH}_3 \rightarrow \text{CH}_3\text{OH} + \text{M}$		2
275	$\text{C} + \text{C} \rightarrow \text{C}_2 + \text{M}$		1
277	$\text{C}_2\text{H} + \text{M} \rightarrow \text{C}_2 + \text{H} + \text{M}$	$\left\{ \begin{array}{l} 2.920 \times 10^{+11} \cdot T^{-5.16} \cdot \exp(-57400/\text{T}) \\ 9.100 \times 10^{-22} \cdot T^{-3.10} \cdot \exp(-2114/\text{T}) \\ k_0 = 5.240 \times 10^{-28} \cdot T^{-1.60} \\ k_\infty = 7.500 \times 10^{-11} \\ 7.200 \times 10^{-12} \\ 1.600 \times 10^{-12} \end{array} \right.$	1
279	$\text{O} + \text{C} \rightarrow \text{CO} + \text{M}$		1
281	$\text{H} + \text{O}_2 \rightarrow \text{HO}_2 + \text{M}$		2
283	$\text{H} + \text{HO}_2 \rightarrow \text{H}_2 + \text{O}_2$		1
285	$\text{H} + \text{HO}_2 \rightarrow \text{H}_2\text{O} + \text{O}$		1
287	$\text{H} + \text{HO}_2 \rightarrow \text{OH} + \text{OH}$	$\left\{ \begin{array}{l} 7.120 \times 10^{-11} \\ 4.800 \times 10^{-11} \cdot \exp(-250/\text{T}) \\ 1.600 \times 10^{-12} \cdot \exp(940/\text{T}) \\ 3.000 \times 10^{-11} \cdot \exp(-200/\text{T}) \\ 2.900 \times 10^{-12} \cdot \exp(160/\text{T}) \end{array} \right.$	1*
289	$\text{OH} + \text{HO}_2 \rightarrow \text{H}_2\text{O} + \text{O}_2$		1*
291	$\text{OH} + \text{O}_3 \rightarrow \text{HO}_2 + \text{O}_2$		1*
293	$\text{HO}_2 + \text{O} \rightarrow \text{OH} + \text{O}_2$		1*
295	$\text{H}_2\text{O}_2 + \text{OH} \rightarrow \text{HO}_2 + \text{H}_2\text{O}$		1*
297	$\text{HCO} + \text{O}_2 \rightarrow \text{HO}_2 + \text{CO}$	$\left\{ \begin{array}{l} 5.200 \times 10^{-12} \\ 1.400 \times 10^{-12} \cdot \exp(2000/\text{T}) \\ 5.400 \times 10^{-12} \cdot \exp(2200/\text{T}) \\ 7.200 \times 10^{-14} \cdot \exp(1080/\text{T}) \\ k_0 = 2.070 \times 10^{-28} \cdot T^{-1.0} \\ k_\infty = 2.600 \times 10^{-11} \end{array} \right.$	1*
299	$\text{H}_2\text{O}_2 + \text{O} \rightarrow \text{OH} + \text{HO}_2$		1*
301	$\text{CH}_3 + \text{O}_3 \rightarrow \text{H}_2\text{CO} + \text{HO}_2$		1*
303	$\text{CH}_3\text{O} + \text{O}_2 \rightarrow \text{H}_2\text{CO} + \text{HO}_2$		1*
305	$\text{OH} + \text{OH} \rightarrow \text{H}_2\text{O}_2 + \text{M}$		2*
307	$\text{H} + \text{O}_3 \rightarrow \text{OH} + \text{O}_2$	$\left\{ \begin{array}{l} 1.400 \times 10^{-10} \cdot \exp(470/\text{T}) \\ k_0 = 5.290 \times 10^{-28} \cdot T^{-2.4} \\ k_\infty = 3.000 \times 10^{-11} \\ 8.000 \times 10^{-12} \cdot \exp(2060/\text{T}) \\ 5.400 \times 10^{-12} \cdot \exp(220/\text{T}) \\ 3.600 \times 10^{-11} \end{array} \right.$	1*
309	$\text{O} + \text{O}_2 \rightarrow \text{O}_3 + \text{M}$		2*
311	$\text{O} + \text{O}_3 \rightarrow \text{O}_2 + \text{O}_2$		1*
313	$\text{CH}_3 + \text{O}_3 \rightarrow \text{CH}_3\text{O} + \text{O}_2$		1*
315	$^1\text{CH}_2 + \text{CH}_4 \rightarrow \text{CH}_3 + \text{CH}_3$		1*
316	$^1\text{CH}_2 + \text{O}_2 \rightarrow \text{HCO} + \text{OH}$	3.000×10^{-11}	1*
317	$^1\text{CH}_2 + \text{M} \rightarrow ^3\text{CH}_2 + \text{M}$	8.800×10^{-12}	1*

Rxn #	Reaction	Rate	Notes
318	$^1\text{CH}_2 + \text{H}_2 \rightarrow \text{CH}_3 + \text{H}$	5.000×10^{-15}	1*
319	$^1\text{CH}_2 + \text{CO}_2 \rightarrow \text{H}_2\text{CO} + \text{CO}$	1.000×10^{-12}	1*
320	$\text{CH} + \text{H}_2 \rightarrow ^3\text{CH}_2 + \text{H}$	$2.380 \times 10^{-10} \cdot \exp(1760/\text{T})$	1*
321	$\text{C}_2\text{H}_2 + \text{O} \rightarrow ^3\text{CH}_2 + \text{CO}$	$2.900 \times 10^{-11} \cdot \exp(1600/\text{T})$	1*
322	$^3\text{CH}_2 + \text{H}_2 \rightarrow \text{CH}_3 + \text{H}$	5.000×10^{-14}	1*
323	$^3\text{CH}_2 + \text{CH}_4 \rightarrow \text{CH}_3 + \text{CH}_3$	$7.100 \times 10^{-12} \cdot \exp(5051/\text{T})$	1*
324	$^3\text{CH}_2 + \text{O}_2 \rightarrow \text{HCO} + \text{OH}$	$4.100 \times 10^{-11} \cdot \exp(750/\text{T})$	1*
325	$^3\text{CH}_2 + \text{O} \rightarrow \text{HCO} + \text{H}$	1.000×10^{-11}	1*
326	$^3\text{CH}_2 + \text{O} \rightarrow \text{CH} + \text{OH}$	8.000×10^{-12}	1*
327	$^3\text{CH}_2 + \text{O} \rightarrow \text{CO} + \text{H} + \text{H}$	8.300×10^{-11}	1*
328	$^3\text{CH}_2 + \text{CO}_2 \rightarrow \text{H}_2\text{CO} + \text{CO}$	1.000×10^{-14}	1*
329	$^3\text{CH}_2 + \text{H} \rightarrow \text{CH} + \text{H}_2$	$4.700 \times 10^{-10} \cdot \exp(370/\text{T})$	1*
330	$^3\text{CH}_2 + ^3\text{CH}_2 \rightarrow \text{C}_2\text{H}_2 + \text{H}_2$	5.300×10^{-11}	1*
331	$^3\text{CH}_2 + \text{CH}_3 \rightarrow \text{C}_2\text{H}_4 + \text{H}$	7.000×10^{-11}	1*
332	$^3\text{CH}_2 + \text{C}_2\text{H}_3 \rightarrow \text{CH}_3 + \text{C}_2\text{H}_2$	3.000×10^{-11}	1*
333	$^3\text{CH}_2 + \text{C}_2\text{H}_5 \rightarrow \text{CH}_3 + \text{C}_2\text{H}_4$	3.000×10^{-11}	1*
334	$\text{H}_2\text{O} + \text{O}(^1\text{D}) \rightarrow \text{OH} + \text{OH}$	2.200×10^{-10}	1*
335	$\text{H}_2 + \text{O}(^1\text{D}) \rightarrow \text{OH} + \text{H}$	1.100×10^{-10}	1*
336	$\text{O}(^1\text{D}) + \text{M} \rightarrow \text{O} + \text{M}$	$1.800 \times 10^{-11} \cdot \exp(-110/\text{T})$	1*
337	$\text{O}(^1\text{D}) + \text{O}_2 \rightarrow \text{O} + \text{O}_2$	$3.200 \times 10^{-11} \cdot \exp(-70/\text{T})$	1*
338	$\text{CH}_4 + \text{O}(^1\text{D}) \rightarrow \text{CH}_3 + \text{OH}$	1.125×10^{-10}	1*
339	$\text{CH}_4 + \text{O}(^1\text{D}) \rightarrow \text{H}_2\text{CO} + \text{H}_2$	7.500×10^{-12}	1*
340	$\text{CH}_4 + \text{O}(^1\text{D}) \rightarrow \text{CH}_3\text{O} + \text{H}$	3.000×10^{-11}	1*
341	$\text{C}_2\text{H}_6 + \text{O}(^1\text{D}) \rightarrow \text{C}_2\text{H}_5 + \text{OH}$	6.200×10^{-10}	1*
342	$\text{CO} + \text{O}(^1\text{D}) \rightarrow \text{CO} + \text{O}$	7.000×10^{-11}	1*
343	$\text{O}_2 + h\nu \rightarrow \text{O} + \text{O}(^1\text{D})$	2.18×10^{-6}	3*
344	$\text{O}_2 + h\nu \rightarrow \text{O} + \text{O}$	5×10^{-8}	3*
345	$\text{H}_2\text{O} + h\nu \rightarrow \text{H} + \text{OH}$	8.16×10^{-6}	3
346	$\text{OH} + h\nu \rightarrow \text{O}(^1\text{D}) + \text{H}$	4.9×10^{-6}	3
347	$\text{O}_3 + h\nu \rightarrow \text{O}_2 + \text{O}(^1\text{D})$	9.98×10^{-3}	3*
348	$\text{O}_3 + h\nu \rightarrow \text{O}_2 + \text{O}$	1.92×10^{-3}	3*
349	$\text{H}_2\text{O}_2 + h\nu \rightarrow \text{OH} + \text{OH}$	1.27×10^{-4}	3
350	$\text{CO}_2 + h\nu \rightarrow \text{CO} + \text{O}$	2.31×10^{-9}	3
351	$\text{CO}_2 + h\nu \rightarrow \text{CO} + \text{O}(^1\text{D})$	2.51×10^{-7}	3
352	$\text{CO} + h\nu \rightarrow \text{C} + \text{O}$	1.54×10^{-6}	3
353	$\text{H}_2\text{CO} + h\nu \rightarrow \text{H}_2 + \text{CO}$	1.15×10^{-4}	3
354	$\text{H}_2\text{CO} + h\nu \rightarrow \text{HCO} + \text{H}$	1.32×10^{-4}	3
355	$\text{HO}_2 + h\nu \rightarrow \text{OH} + \text{O}$	6.13×10^{-4}	3
356	$\text{CH} + h\nu \rightarrow \text{C} + \text{H}$	4.25×10^{-5}	3
357	$\text{CH}_3 + h\nu \rightarrow ^1\text{CH}_2 + \text{H}$	0.	3
358	$\text{CH}_4 + h\nu \rightarrow ^1\text{CH}_2 + \text{H}_2$	1.78×10^{-6}	3
359	$\text{CH}_4 + h\nu \rightarrow \text{CH}_3 + \text{H}$	3.41×10^{-6}	3
360	$\text{CH}_4 + h\nu \rightarrow ^3\text{CH}_2 + \text{H} + \text{H}$	1.67×10^{-6}	3
361	$\text{C}_2\text{H}_2 + h\nu \rightarrow \text{C}_2\text{H} + \text{H}$	1.14×10^{-6}	3
362	$\text{C}_2\text{H}_2 + h\nu \rightarrow \text{C}_2 + \text{H}_2$	6.55×10^{-7}	3
363	$\text{C}_2\text{H}_3 + h\nu \rightarrow \text{C}_2\text{H}_2 + \text{H}$	2.94×10^{-4}	3
364	$\text{C}_2\text{H}_4 + h\nu \rightarrow \text{C}_2\text{H}_2 + \text{H}_2$	2.08×10^{-5}	3
365	$\text{C}_2\text{H}_4 + h\nu \rightarrow \text{C}_2\text{H}_2 + \text{H} + \text{H}$	2.17×10^{-5}	3
366	$\text{C}_2\text{H}_6 + h\nu \rightarrow ^3\text{CH}_2 + ^3\text{CH}_2 + \text{H}_2$	$4. \times 10^{-6}$	3

Rxn #	Reaction	Rate	Notes
367	$\text{C}_2\text{H}_6 + h\nu \rightarrow \text{CH}_4 + {}^1\text{CH}_2$	$1. \times 10^{-6}$	3
368	$\text{CH}_2\text{CO} + h\nu \rightarrow {}^3\text{CH}_2 + \text{CO}$	7.03×10^{-4}	3
369	${}^1\text{CH}_2 + \text{H}_2 \rightarrow {}^3\text{CH}_2 + \text{H}_2$	1.260×10^{-11}	1

The reaction list is largely composed of forward reactions that are then used to calculate the reverse reactions, based on the thermodynamic properties of the species involved in the reaction. However, some reactions do not have reversed reactions, including a) the ones where a molecule in an excited state relaxes into the ground state (e.g., reaction 369), and b) photolysis reactions (such as reaction 368). The majority of these reactions are detailed in [Tsai et al. \(2017\)](#) as the reduced C-H-O system, to which we have added reactions for oxidizing species (denoted by the asterisk*: #287–342; #343–344; #347–348).

1: $\text{cm}^3 \text{ molecules}^{-2} \text{ s}^{-1}$

2: These reaction rates take the form: $k(\text{M}, T) = k_0(T)[M]/[1 + k_0(T)[m]/k_\infty(T)] \cdot 0.6^{[1 + [\log_{10}[k_0(T)[M]/k_\infty(T)]]^2]^{-1}}$, where $k_0(T)$ has units of $\text{cm}^6 \text{ molecules}^{-2} \text{ s}^{-1}$ and $k_\infty(T)$ has units of $\text{cm}^3 \text{ molecules}^{-2} \text{ s}^{-1}$.

3: The photolysis rates (in /s) presented here are taken from the uppermost layer in the model. Caution: the rates in the upper atmosphere are not good indicators for rates in the lower atmosphere.

C. COMPOSITION

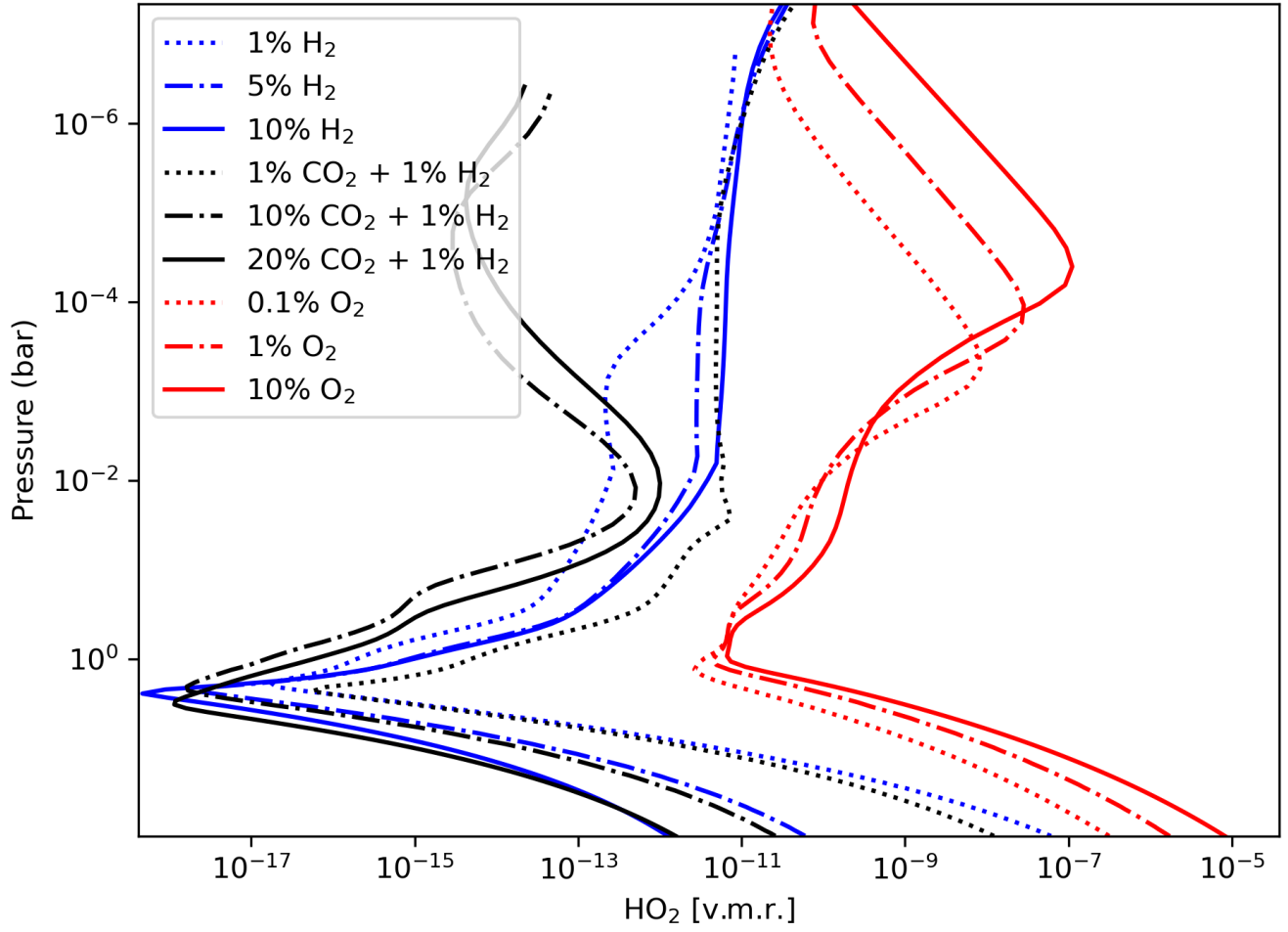


Figure 11. HO_2 profiles for the cases seen in Fig. 5, and sharing the same color palette.

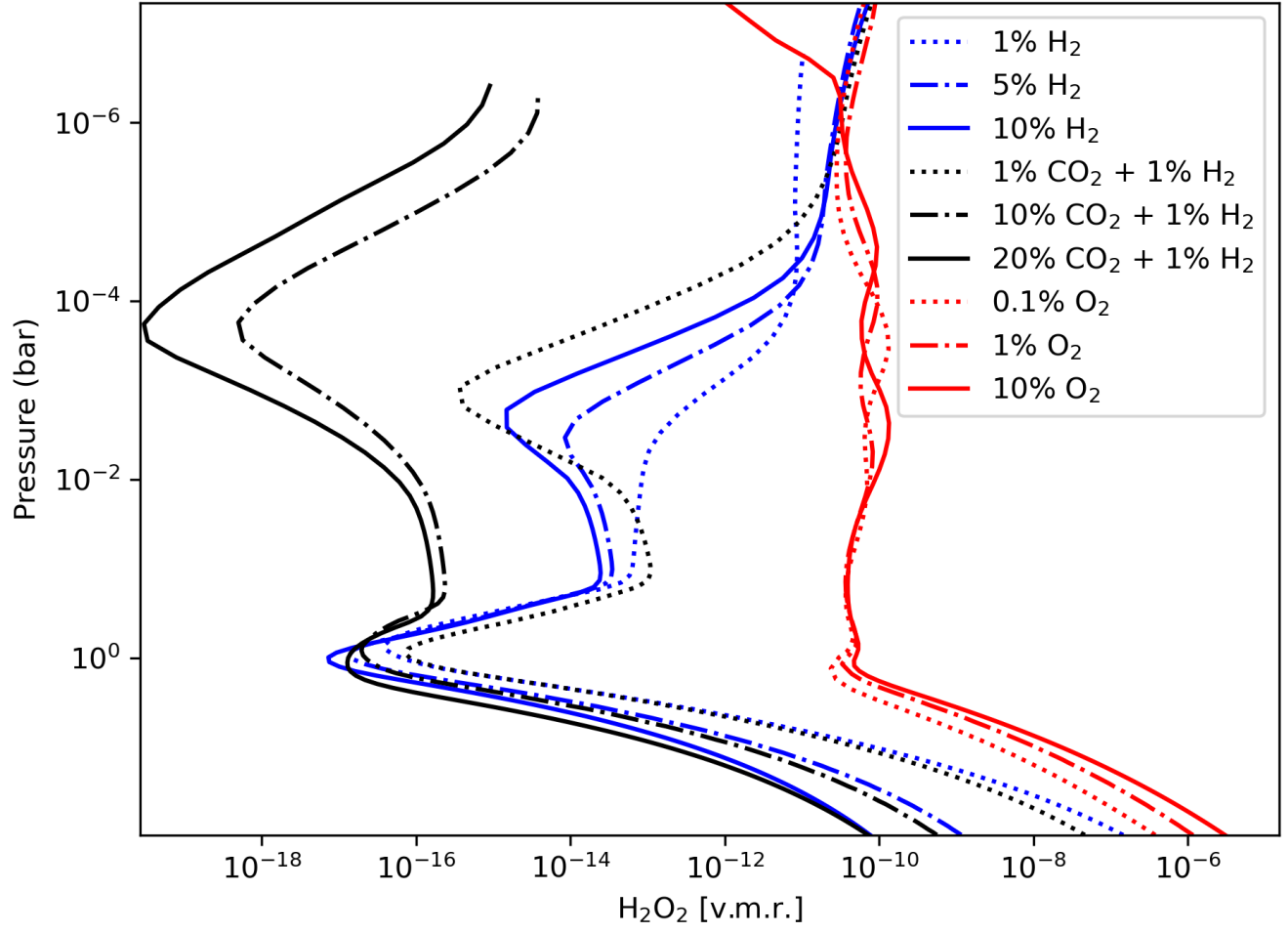


Figure 12. H_2O_2 profiles for the cases seen in Fig. 5, and sharing the same color palette.

D. SECONDARY ANALYSES

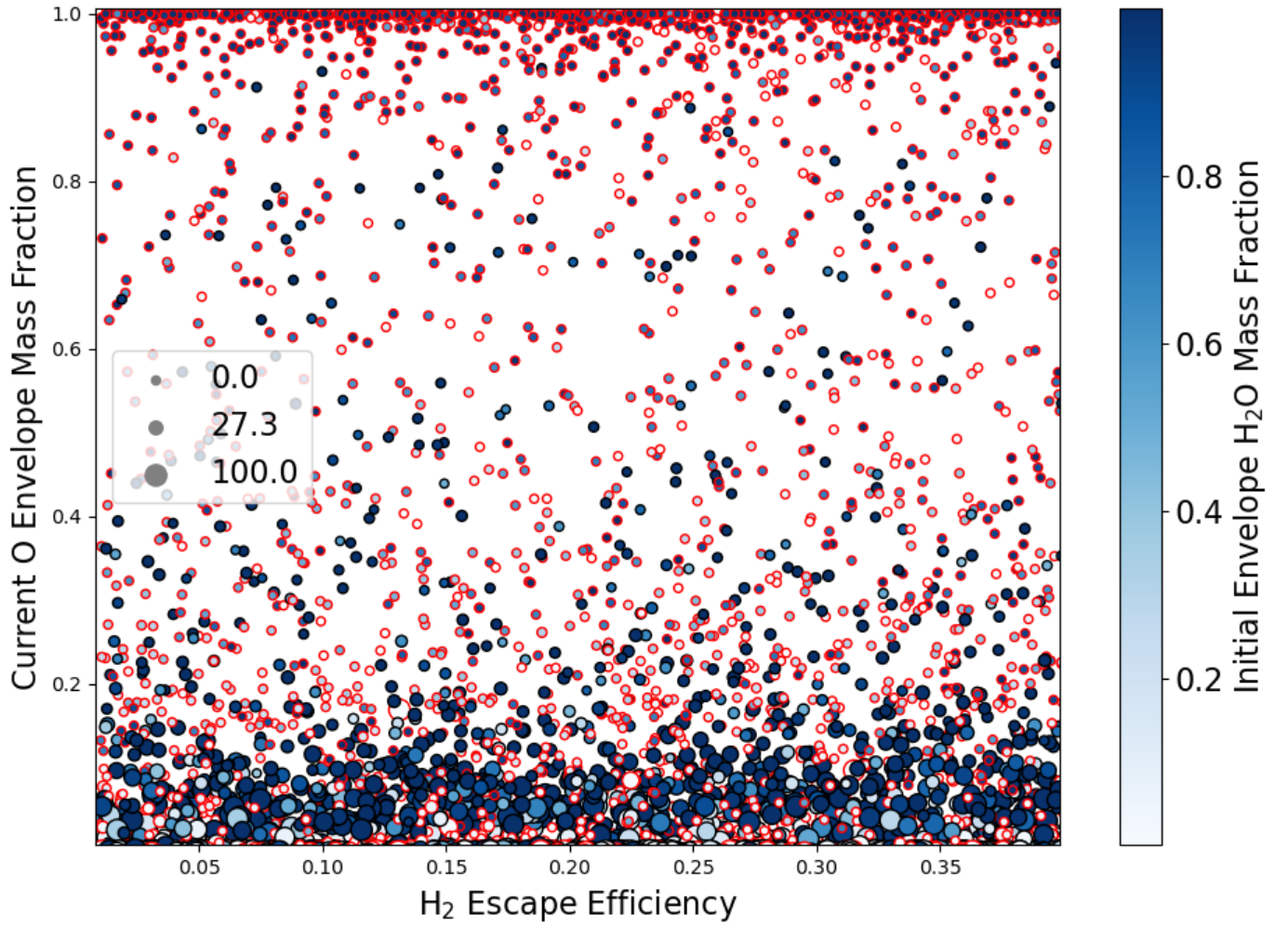


Figure 13. The water inventory for planets in our Monte Carlo atmospheric escape ensemble as a function of the assumed H₂ escape efficiency. The circle size indicates the initial envelope mass as a fraction of the total planet mass. A red edge color for a given symbol denotes a scenario with less than 1 Earth ocean at present day, which would likely be short-lived (Kasting & Pollack 1983).

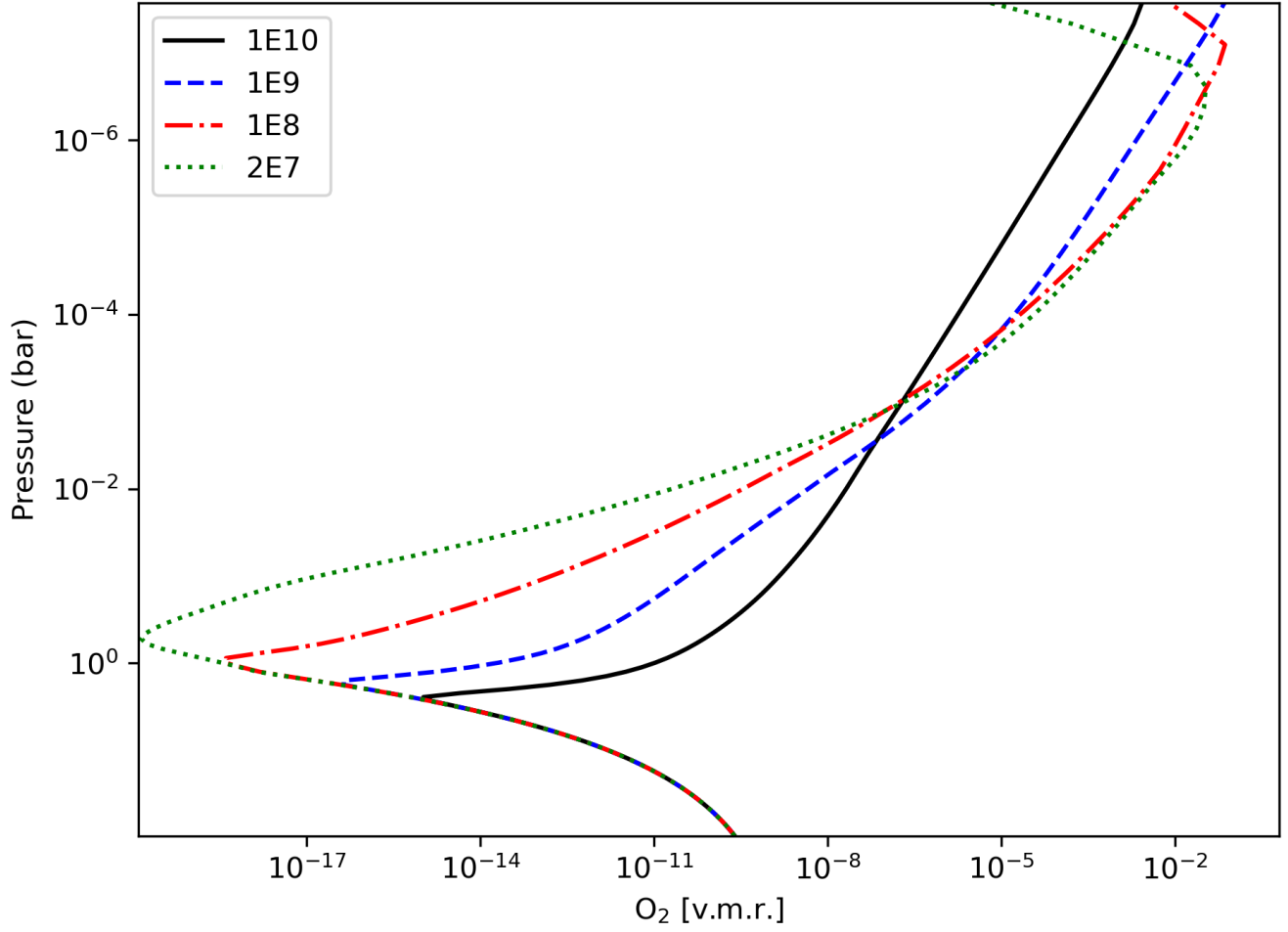


Figure 14. Molecular oxygen response to changing eddy diffusion profile strengths (values indicated in the key, with units of cm^2/s) for the 10% H_2 scenario. Smaller values of K_{zz} prevent photochemically-produced O_2 from being mixed down into the middle atmosphere, resulting in larger upper atmospheric concentrations at the expense of lower atmospheric concentrations.

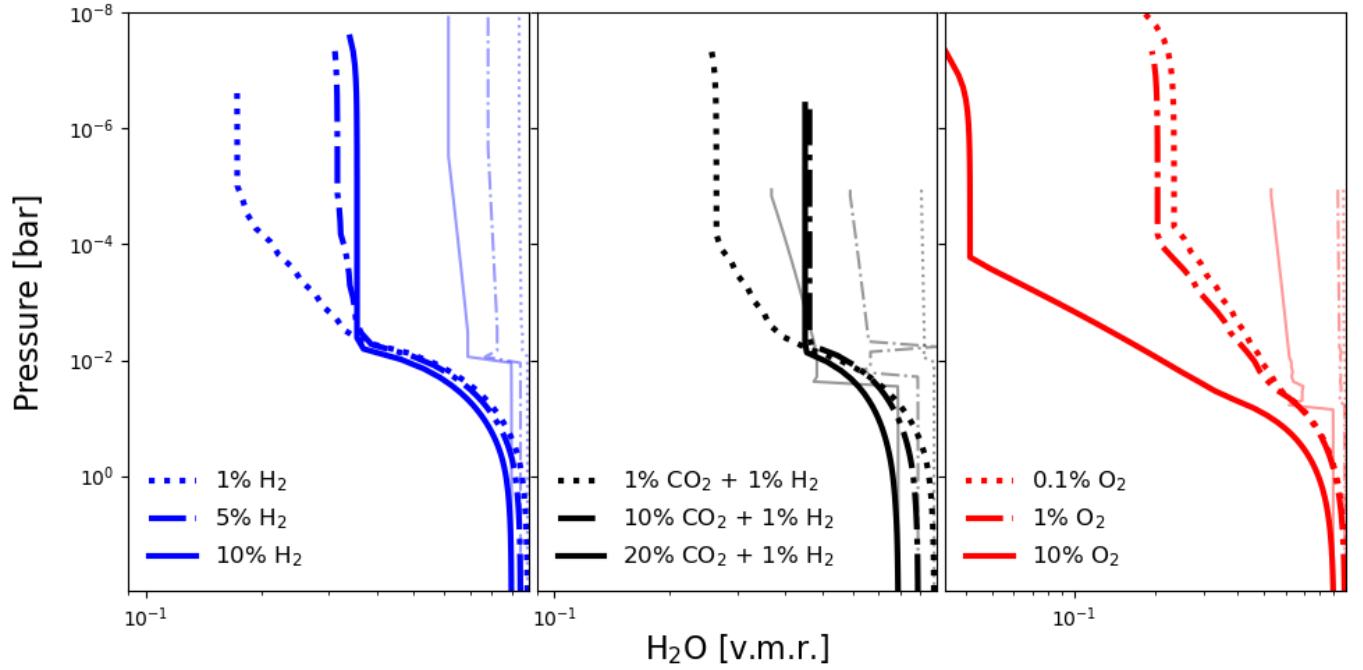


Figure 15. The water vapor profiles for the scenarios outlined in the main text from the photochemical model (heavy lines) compared with the water profiles produced by the radiative-convective model (light, pale lines). Differences between the two profiles are confined to the upper atmosphere (above ~ 10 mbar) and do not produce more than a ~ 5 ppm change in the resulting transmission spectra.

REFERENCES

- Aguichine, A., Mousis, O., Deleuil, M., & Marcq, E. 2021, Mass-radius relationships for irradiated ocean planets. <https://arxiv.org/abs/2105.01102>
- Ali-Dib, M., Mousis, O., Petit, J.-M., & Lunine, J. I. 2014, *The Astrophysical Journal*, 793, 9
- Ardaseva, A., Rimmer, P. B., Waldmann, I., et al. 2017, *Monthly Notices of the Royal Astronomical Society*, 470, 187
- Armstrong, D. J., Lopez, T. A., Adibekyan, V., et al. 2020, *Nature*, 583, 39
- Arney, G. N., Meadows, V. S., Domagal-Goldman, S. D., et al. 2017, *The Astrophysical Journal*, 836, 49
- Atri, D., & Mogan, S. R. C. 2021, *Monthly Notices of the Royal Astronomical Society: Letters*, 500, L1
- Bailey, E., & Stevenson, D. J. 2019, AGUFM, 2019, P11A
- Bakos, G., Noyes, R., Kovács, G., et al. 2004, *Publications of the Astronomical Society of the Pacific*, 116, 266
- Banks, P. M., & Kockarts, G. 1973, *Aeronomy* (Academic Press)
- Baraffe, I., Homeier, D., Allard, F., & Chabrier, G. 2015, *Astronomy & Astrophysics*, 577, A42
- Barclay, T., Pepper, J., & Quintana, E. V. 2018, *The Astrophysical Journal Supplement Series*, 239, 2
- Barclay, T., Burke, C. J., Howell, S. B., et al. 2013, *The Astrophysical Journal*, 768, 101
- Barnes, R., Luger, R., Deitrick, R., et al. 2020, *Publications of the Astronomical Society of the Pacific*, 132, 024502
- Batalha, N. E., Kempton, E. M.-R., & Mbarek, R. 2017a, *The Astrophysical Journal Letters*, 836, L5
- Batalha, N. E., Mandell, A., Pontoppidan, K., et al. 2017b, *Publications of the Astronomical Society of the Pacific*, 129, 064501
- Batalha, N. M. 2014, *Proceedings of the National Academy of Sciences*, 111, 12647
- Bean, J. L., Raymond, S. N., & Owen, J. E. 2021, *Journal of Geophysical Research: Planets*, 126, e2020JE006639
- Benneke, B., Knutson, H. A., Lothringer, J., et al. 2019, *Nature Astronomy*, 3, 813
- Bixel, A., & Apai, D. 2020, *The Astrophysical Journal*, 896, 131
- Bolmont, E., Selsis, F., Owen, J. E., et al. 2017, *Monthly Notices of the Royal Astronomical Society*, 464, 3728
- Borucki, W. J., Koch, D., Basri, G., et al. 2010, *Science*, 327, 977
- Bouhrel, M. A., Hwang, J. T., Bartoli, N., et al. 2019, *Advances in Engineering Software*, 102662, doi: <https://doi.org/10.1016/j.advengsoft.2019.03.005>
- Brugger, B., Mousis, O., Deleuil, M., & Deschamps, F. 2017, *The Astrophysical Journal*, 850, 93
- Burke, C. J., Christiansen, J. L., Mullally, F., et al. 2015, *The Astrophysical Journal*, 809, 8
- Burrows, A., & Sharp, C. 1999, *The Astrophysical Journal*, 512, 843
- Cavalié, T., Venot, O., Selsis, F., et al. 2017, *Icarus*, 291, 1
- Charnay, B., Blain, D., Bézard, B., et al. 2020, arXiv preprint arXiv:2011.11553
- Chau, R., Hamel, S., & Nellis, W. J. 2011, *Nature communications*, 2, 1
- Chen, H., & Rogers, L. A. 2016, *The Astrophysical Journal*, 831, 180
- Chen, H., Wolf, E. T., Zhan, Z., & Horton, D. E. 2019, *The Astrophysical Journal*, 886, 16
- Chouqar, J., Benkhaldoun, Z., Jabiri, A., et al. 2020, *Monthly Notices of the Royal Astronomical Society*, 495, 962
- Cohen, O., Ma, Y., Drake, J. J., et al. 2015, *The Astrophysical Journal*, 806, 41
- Cranmer, S. R. 2004, *American Journal of Physics*, 72, 1397
- Cuntz, M., & Wang, Z. 2018, *Research Notes of the AAS*, 2, 19, doi: [10.3847/2515-5172/aaaa67](https://doi.org/10.3847/2515-5172/aaaa67)
- Dai, F., Masuda, K., Winn, J. N., & Zeng, L. 2019, *The Astrophysical Journal*, 883, 79
- Delrez, L., Gillon, M., Queloz, D., et al. 2018, in *Ground-based and Airborne Telescopes VII*, Vol. 10700, International Society for Optics and Photonics, 107001I
- Demory, B. O., Pozuelos, F. J., Gomez Maqueo Chew, Y., et al. 2020, arXiv e-prints, arXiv:2009.04317. <https://arxiv.org/abs/2009.04317>
- Deschamps, F., & Sotin, C. 2001, *Journal of Geophysical Research: Planets*, 106, 5107
- Dodson-Robinson, S. E., & Bodenheimer, P. 2010, *Icarus*, 207, 491
- Dorn, C., Khan, A., Heng, K., et al. 2015, *Astronomy & Astrophysics*, 577, A83
- Dragomir, D., Matthews, J. M., Kuschnig, R., et al. 2012, *The Astrophysical Journal*, 759, 2
- Dressing, C. D., & Charbonneau, D. 2013, *The Astrophysical Journal*, 767, 95
- Driscoll, P., & Bercovici, D. 2013, *Icarus*, 226, 1447
- Ercolano, B., & Clarke, C. 2010, *Monthly Notices of the Royal Astronomical Society*, 402, 2735
- Erkaev, N., Kulikov, Y. N., Lammer, H., et al. 2007, *Astronomy & Astrophysics*, 472, 329
- Estrela, R., Swain, M. R., Gupta, A., Sotin, C., & Valio, A. 2020, *The Astrophysical Journal*, 898, 104
- Faucher, T. J., Turbet, M., Villanueva, G. L., et al. 2019, *ApJ*, 887, 194, doi: [10.3847/1538-4357/ab5862](https://doi.org/10.3847/1538-4357/ab5862)

- Faucher, T. J., Villanueva, G. L., Schwieterman, E. W., et al. 2020, *Nature Astronomy*, 4, 372
- Fortney, J. J., Dawson, R. I., & Komacek, T. D. 2021, *Journal of Geophysical Research: Planets*, 126, e2020JE006629, doi: <https://doi.org/10.1029/2020JE006629>
- Fortney, J. J., Marley, M. S., & Barnes, J. W. 2007, *The Astrophysical Journal*, 659, 1661
- France, K., Loyd, R. P., Youngblood, A., et al. 2016, *The Astrophysical Journal*, 820, 89
- France, K., Duvvuri, G., Egan, H., et al. 2020, *The Astronomical Journal*, 160, 237
- Fu, R., O'Connell, R. J., & Sasselov, D. D. 2009, *The Astrophysical Journal*, 708, 1326
- Fulton, B. J., & Petigura, E. A. 2018, *The Astronomical Journal*, 156, 264
- Fulton, B. J., Petigura, E. A., Howard, A. W., et al. 2017, *The Astronomical Journal*, 154, 109
- Gaia Collaboration, Brown, A. G. A., Vallenari, A., et al. 2018, *A&A*, 616, A1, doi: [10.1051/0004-6361/201833051](https://doi.org/10.1051/0004-6361/201833051)
- Gando, A., Dwyer, D., McKeown, R., Zhang, C., & the KamLAND Collaboration. 2011, *Nature Geoscience*, 4, 647
- Gao, P., Marley, M. S., & Ackerman, A. S. 2018, *The Astrophysical Journal*, 855, 86
- Gao, P., Marley, M. S., Zahnle, K., Robinson, T. D., & Lewis, N. K. 2017, *The Astronomical Journal*, 153, 139
- Gillon, M., Triaud, A. H., Demory, B.-O., et al. 2017, *Nature*, 542, 456
- Ginzburg, S., Schlichting, H. E., & Sari, R. 2018, *Monthly Notices of the Royal Astronomical Society*, 476, 759
- Greene, T. P., Line, M. R., Montero, C., et al. 2016, *The Astrophysical Journal*, 817, 17
- Gronoff, G., Arras, P., Baraka, S., et al. 2020, *Journal of Geophysical Research: Space Physics*, e2019JA027639
- Gupta, A., & Schlichting, H. E. 2020, *Monthly Notices of the Royal Astronomical Society*, 493, 792
- Haar, L., Gallagher, J., & Kell, G. 1984, *NBS/NRC Steam Tables: Thermodynamic and Transport Properties and Computer Programs for Vapor and Liquid States of Water in SI Units* (Hemisphere Publishing Corporation, Washington)
- Hamano, K., Abe, Y., & Genda, H. 2013, *Nature*, 497, 607
- Hardegree-Ullman, K. K., Cushing, M. C., Muirhead, P. S., & Christiansen, J. L. 2019, *The Astronomical Journal*, 158, 75
- He, C., Hörst, S. M., Lewis, N. K., et al. 2018, *The Astronomical Journal*, 156, 38
- . 2020a, *The Planetary Science Journal*, 1, 51
- . 2020b, *Nature Astronomy*, 1
- Helled, R., Anderson, J. D., Podolak, M., & Schubert, G. 2010, *The Astrophysical Journal*, 726, 15
- Hellier, C., Anderson, D., Collier Cameron, A., et al. 2012, *Monthly Notices of the Royal Astronomical Society*, 426, 739
- Hidalgo, S. L., Pietrinferni, A., Cassisi, S., et al. 2018, *The Astrophysical Journal*, 856, 125
- Hörst, S. M., He, C., Ugelow, M. S., et al. 2018, *The Astrophysical Journal*, 858, 119
- Hu, R., & Seager, S. 2014, *The Astrophysical Journal*, 784, 63
- Hubbard, W. B. 1981, *Science*, 214, 145
- Hunten, D. M. 1973, *Journal of Atmospheric Sciences*, 30, 1481
- Hunten, D. M., Pepin, R. O., & Walker, J. C. 1987, *Icarus*, 69, 532
- Jehin, E., Gillon, M., Queloz, D., et al. 2011, *Msngr*, 145, 2
- Jin, R., Chen, W., & Sudjianto, A. 2003, in *International Design Engineering Technical Conferences and Computers and Information in Engineering Conference*, Vol. 37009, 545–554
- Johnstone, C., Güdel, M., Brott, I., & Lüftinger, T. 2015a, *Astronomy & Astrophysics*, 577, A28
- Johnstone, C., Güdel, M., Stökl, A., et al. 2015b, *The Astrophysical Journal Letters*, 815, L12
- Johnstone, C. P. 2020, *The Astrophysical Journal*, 890, 79
- Kane, S. R., Barclay, T., & Gelino, D. M. 2013, *The Astrophysical Journal Letters*, 770, L20
- Kane, S. R., Ceja, A. Y., Way, M. J., & Quintana, E. V. 2018, *The Astrophysical Journal*, 869, 46
- Kane, S. R., Roettenbacher, R. M., Unterborn, C. T., Foley, B. J., & Hill, M. L. 2020, *A Volatile-Poor Formation of LHS 3844b based on its Lack of Significant Atmosphere*. <https://arxiv.org/abs/2007.14493>
- Kasting, J. F. 1988, *Icarus*, 74, 472
- Kasting, J. F., & Pollack, J. B. 1983, *Icarus*, 53, 479
- Kasting, J. F., Whitmire, D. P., & Reynolds, R. T. 1993, *Icarus*, 101, 108, doi: [10.1006/icar.1993.1010](https://doi.org/10.1006/icar.1993.1010)
- Katyal, N., Nikolaou, A., Godolt, M., et al. 2019, *The Astrophysical Journal*, 875, 31
- Kawabata, K., Coffeen, D., Hansen, J., et al. 1980, *Journal of Geophysical Research: Space Physics*, 85, 8129
- Kawashima, Y., & Rugheimer, S. 2019, *The Astronomical Journal*, 157, 213
- Kempton, E. M.-R., Bean, J. L., & Parmentier, V. 2017, *The Astrophysical Journal Letters*, 845, L20
- King, G. W., & Wheatley, P. J. 2020, *arXiv e-prints*, arXiv:2007.13731. <https://arxiv.org/abs/2007.13731>
- Kislyakova, K. G., Lammer, H., Holmström, M., et al. 2013, *Astrobiology*, 13, 1030

- Kite, E. S., & Barnett, M. N. 2020, *Proceedings of the National Academy of Sciences*, 117, 18264
- Kite, E. S., Fegley Jr, B., Schaefer, L., & Ford, E. B. 2020, *The Astrophysical Journal*, 891, 111
- Kite, E. S., Manga, M., & Gaidos, E. 2009, *The Astrophysical Journal*, 700, 1732
- Kite, E. S., & Schaefer, L. 2021, *Water on Hot Rocky Exoplanets*. <https://arxiv.org/abs/2103.07753>
- Knudson, M. D., Desjarlais, M. P., Lemke, R., et al. 2012, *Physical Review Letters*, 108, 091102
- Kopparapu, R., Arney, G., Haqq-Misra, J., Lustig-Yaeger, J., & Villanueva, G. 2021, *The Astrophysical Journal*, 908, 164
- Kopparapu, R. K., Ramirez, R. M., SchottelKotte, J., et al. 2014, *ApJL*, 787, L29, doi: [10.1088/2041-8205/787/2/L29](https://doi.org/10.1088/2041-8205/787/2/L29)
- Kopparapu, R. K., Ramirez, R., Kasting, J. F., et al. 2013, *ApJ*, 765, 131, doi: [10.1088/0004-637X/765/2/131](https://doi.org/10.1088/0004-637X/765/2/131)
- Korolev, A. V., & Mazin, I. P. 2003, *Journal of the atmospheric sciences*, 60, 2957
- Koskinen, T. T., Aylward, A. D., & Miller, S. 2007, *Nature*, 450, 845
- Koskinen, T. T., Lavvas, P., Harris, M. J., & Yelle, R. V. 2014, *Philosophical Transactions of the Royal Society A: Mathematical, Physical and Engineering Sciences*, 372, 20130089
- Kral, Q., Davoult, J., & Charnay, B. 2020, *Nature Astronomy*, 4, 769
- Krämer, M., Schiller, C., Afchine, A., et al. 2009, *Atmospheric Chemistry and Physics*, 9, 3505
- Krasnopolsky, V., & Pollack, J. 1994, *Icarus*, 109, 58
- Kreidberg, L., Koll, D. D., Morley, C., et al. 2019, *Nature*, 573, 87
- Kuramoto, K., Umemoto, T., & Ishiwatari, M. 2013, *Earth and Planetary Science Letters*, 375, 312
- Kutner, M. L. 2003, *Astronomy: A physical perspective* (Cambridge University Press)
- Lavvas, P., Koskinen, T., Steinrueck, M. E., Muñoz, A. G., & Showman, A. P. 2019, *The Astrophysical Journal*, 878, 118
- Lee, E. J., & Chiang, E. 2016, *The Astrophysical Journal*, 817, 90
- Lee, E. J., Chiang, E., & Ormel, C. W. 2014, *The Astrophysical Journal*, 797, 95
- Lehmer, O. R., Catling, D. C., & Krissansen-Totton, J. 2020, *Nature communications*, 11, 1
- Lincowski, A. P., Meadows, V. S., Crisp, D., et al. 2018, *The Astrophysical Journal*, 867, 76
- Lissauer, J. J. 2007, *The Astrophysical Journal Letters*, 660, L149
- Liu, B., Lambrechts, M., Johansen, A., & Liu, F. 2019, *Astronomy & Astrophysics*, 632, A7
- Lodders, K., & Fegley Jr, B. 1994, *Icarus*, 112, 368
- . 2002, *Icarus*, 155, 393
- Lopez, E. D. 2017, *Monthly Notices of the Royal Astronomical Society*, 472, 245
- Lopez, E. D., & Fortney, J. J. 2014, *The Astrophysical Journal*, 792, 1
- Loyd, R. P., Shkolnik, E. L., Schneider, A. C., et al. 2020, *The Astrophysical Journal*, 890, 23
- Loyd, R. P., France, K., Youngblood, A., et al. 2016, *The Astrophysical Journal*, 824, 102
- Luger, R., & Barnes, R. 2015, *Astrobiology*, 15, 119
- Luger, R., Barnes, R., Lopez, E., et al. 2015, *Astrobiology*, 15, 57
- Lustig-Yaeger, J., Meadows, V. S., & Lincowski, A. P. 2019a, *The Astronomical Journal*, 158, 27
- . 2019b, *The Astrophysical Journal Letters*, 887, L11
- Madhusudhan, N., Agúndez, M., Moses, J. I., & Hu, Y. 2016, *Space science reviews*, 205, 285
- Mahadevan, S., Ramsey, L., Bender, C., et al. 2012, in *Ground-based and Airborne Instrumentation for Astronomy IV*, Vol. 8446, International Society for Optics and Photonics, 84461S
- Mahadevan, S., Ramsey, L. W., Terrien, R., et al. 2014, in *Ground-based and Airborne Instrumentation for Astronomy V*, Vol. 9147, International Society for Optics and Photonics, 91471G
- Marcus, R. A., Sasselov, D., Hernquist, L., & Stewart, S. T. 2010, *The Astrophysical Journal Letters*, 712, L73
- Meadows, V. S., Reinhard, C. T., Arney, G. N., et al. 2018, *Astrobiology*, 18, 630
- Meyer, C. A., McClintock, R. B., Silvestri, G. J., & Spencer, R. C. 1983, *ASME Steam Tables: Thermodynamic and Transport Properties of Steam* (American Society of Mechanical Engineers, Fifth Edition)
- Mikal-Evans, T., Crossfield, I. J., Benneke, B., et al. 2020, *The Astronomical Journal*, 161, 18
- Millot, M., Hamel, S., Rygg, J. R., et al. 2018, *Nature Physics*, 14, 297
- Misener, W., & Schlichting, H. E. 2021, *arXiv preprint arXiv:2103.09212*
- Misra, A., Meadows, V., Claire, M., & Crisp, D. 2014, *Astrobiology*, 14, 67
- Moore, K., & Cowan, N. B. 2020, *arXiv preprint arXiv:2006.08514*
- Moran, S. E., Hörst, S. M., Batalha, N. E., Lewis, N. K., & Wakeford, H. R. 2018, *The Astronomical Journal*, 156, 252

- Moran, S. E., Hörst, S. M., Vuitton, V., et al. 2020, *The Planetary Science Journal*, 1, 17
- Mordasini, C., Alibert, Y., & Benz, W. 2009, *Astronomy & Astrophysics*, 501, 1139
- Moses, J., Cavalié, T., Fletcher, L., & Roman, M. 2020, *Philosophical Transactions of the Royal Society A*, 378, 20190477
- Mousis, O., Aguichine, A., Atkinson, D. H., et al. 2020a, *Space Science Reviews*, 216, 1
- Mousis, O., Deleuil, M., Aguichine, A., et al. 2020b, arXiv preprint arXiv:2002.05243
- Mueller-Wodarg, I., Strobel, D., Moses, J., et al. 2008, *Space science reviews*, 139, 191
- Murray-Clay, R. A., Chiang, E. I., & Murray, N. 2009, *The Astrophysical Journal*, 693, 23
- Nettelmann, N., Wang, K., Fortney, J. J., et al. 2016, *Icarus*, 275, 107
- Nikolaou, A., Katyal, N., Tosi, N., et al. 2019, *The Astrophysical Journal*, 875, 11
- Noack, L., Höning, D., Rivoldini, A., et al. 2016, *Icarus*, 277, 215
- Owen, J. E., & Alvarez, M. A. 2016, *The Astrophysical Journal*, 816, 34
- Owen, J. E., & Campos Estrada, B. 2020, *Monthly Notices of the Royal Astronomical Society*, 491, 5287
- Owen, J. E., & Jackson, A. P. 2012, *Monthly Notices of the Royal Astronomical Society*, 425, 2931
- Owen, J. E., & Wu, Y. 2013, *The Astrophysical Journal*, 775, 105
- . 2016, *The Astrophysical Journal*, 817, 107
- . 2017, *The Astrophysical Journal*, 847, 29
- Peacock, S., Barman, T., Shkolnik, E. L., et al. 2020, *The Astrophysical Journal*, 895, 5
- Pearl, J., & Conrath, B. 1991, *Journal of Geophysical Research: Space Physics*, 96, 18921
- Pidhorodetska, D., Moran, S. E., Schwieterman, E. W., et al. 2021, L 98-59: a Benchmark System of Small Planets for Future Atmospheric Characterization. <https://arxiv.org/abs/2106.00685>
- Piette, A. A., & Madhusudhan, N. 2020, arXiv preprint arXiv:2009.11290
- Pollacco, D. L., Skillen, I., Cameron, A. C., et al. 2006, *Publications of the Astronomical Society of the Pacific*, 118, 1407
- Poppenhaeger, K., Ketzner, L., & Mallonn, M. 2020, *Monthly Notices of the Royal Astronomical Society*
- Rafikov, R. R. 2006, *The Astrophysical Journal*, 648, 666
- . 2011, *The Astrophysical Journal*, 727, 86
- Ramirez, R. M., & Kaltenegger, L. 2014, *The Astrophysical Journal Letters*, 797, L25
- Ranjan, S., Schwieterman, E. W., Harman, C., et al. 2020, arXiv preprint arXiv:2004.04185
- Redmer, R., Mattsson, T. R., Nettelmann, N., & French, M. 2011, *Icarus*, 211, 798
- Reed, N. W., Browne, E. C., & Tolbert, M. A. 2020, *ACS Earth and Space Chemistry*, 4, 897
- Ricker, G. R., Winn, J. N., Vanderspek, R., et al. 2014, *Journal of Astronomical Telescopes, Instruments, and Systems*, 1, 014003
- Rogers, L., & Seager, S. 2010, *The Astrophysical Journal*, 712, 974
- Rogers, L. A. 2015, *The Astrophysical Journal*, 801, 41
- Rugheimer, S., & Kaltenegger, L. 2018, *The Astrophysical Journal*, 854, 19
- Rugheimer, S., Kaltenegger, L., Zsom, A., Segura, A., & Sasselov, D. 2013, *Astrobiology*, 13, 251
- Rushby, A. J., Claire, M. W., Osborn, H., & Watson, A. J. 2013, *Astrobiology*, 13, 833
- Sanz-Forcada, J., Micela, G., Ribas, I., et al. 2011, *Astronomy & Astrophysics*, 532, A6
- Schaefer, L., & Fegley Jr, B. 2010, *Icarus*, 208, 438
- . 2011, *The Astrophysical Journal*, 729, 6
- Schaefer, L., Wordsworth, R. D., Berta-Thompson, Z., & Sasselov, D. 2016, *The Astrophysical Journal*, 829, 63
- Schubert, G., & Soderlund, K. M. 2011, *Physics of the Earth and Planetary Interiors*, 187, 92
- Schwieterman, E. W., Reinhard, C. T., Olson, S. L., et al. 2019, *The Astrophysical Journal*, 874, 9
- Seager, S., Kuchner, M., Hier-Majumder, C., & Militzer, B. 2007, *The Astrophysical Journal*, 669, 1279
- Segura, A., Kasting, J. F., Meadows, V., et al. 2005, *Astrobiology*, 5, 706
- Segura, A., Krelow, K., Kasting, J. F., et al. 2003, *Astrobiology*, 3, 689
- Selsis, F., Kasting, J. F., Levrard, B., et al. 2007, *Astronomy & Astrophysics*, 476, 1373
- Soubiran, F., & Militzer, B. 2015, *The Astrophysical Journal*, 806, 228
- Stefansson, G., Kopparapu, R., Lin, A., et al. 2020, arXiv e-prints, arXiv:2006.11180. <https://arxiv.org/abs/2006.11180>
- Stelzer, B., Marino, A., Micela, G., López-Santiago, J., & Liefke, C. 2013, *Monthly Notices of the Royal Astronomical Society*, 431, 2063
- Tian, B. Y., & Stanley, S. 2013, *The Astrophysical Journal*, 768, 156
- Tian, F. 2009, *The Astrophysical Journal*, 703, 905
- . 2015, *Earth and Planetary Science Letters*, 432, 126
- Tilley, M. A., Segura, A., Meadows, V., Hawley, S., & Davenport, J. 2019, *Astrobiology*, 19, 64

- Toon, O. B., McKay, C. P., Ackerman, T. P., & Santhanam, K. 1989, *J. Geophys. Res.*, 94, 16287, doi: [10.1029/JD094iD13p16287](https://doi.org/10.1029/JD094iD13p16287)
- Tsai, S.-M., Lyons, J. R., Grosheintz, L., et al. 2017, *The Astrophysical Journal Supplement Series*, 228, 20
- Tsang, C. C., Wilson, C. F., Barstow, J. K., et al. 2010, *Geophysical research letters*, 37
- Turbet, M., Bolmont, E., Ehrenreich, D., et al. 2020, *Astronomy & Astrophysics*, 638, A41
- Twicken, J. D., Jenkins, J. M., Seader, S. E., et al. 2016, *The Astronomical Journal*, 152, 158
- Unterborn, C. T., Dismukes, E. E., & Panero, W. R. 2016, *The Astrophysical Journal*, 819, 32
- Valencia, D., Guillot, T., Parmentier, V., & Freedman, R. S. 2013, *The Astrophysical Journal*, 775, 10
- Venot, O., Agúndez, M., Selsis, F., Tessenyi, M., & Iro, N. 2014, *Astronomy & Astrophysics*, 562, A51
- Venturini, J., & Helled, R. 2017, *The Astrophysical Journal*, 848, 95
- Villanueva, G. L., Smith, M. D., Protopapa, S., Faggi, S., & Mandell, A. M. 2018, *JQSRT*, 217, 86, doi: [10.1016/j.jqsrt.2018.05.023](https://doi.org/10.1016/j.jqsrt.2018.05.023)
- Villanueva, G. L., Smith, M. D., Protopapa, S., Faggi, S., & Mandell, A. M. 2018, *Journal of Quantitative Spectroscopy and Radiative Transfer*, 217, 86
- Visscher, C., & Moses, J. I. 2011, *The Astrophysical Journal*, 738, 72
- Visscher, C., Moses, J. I., & Saslow, S. A. 2010, *Icarus*, 209, 602
- Vuitton, V., Moran, S. E., He, C., et al. 2021, *The Planetary Science Journal*, 2, 2
- Walker, J. C. 1975, *Journal of the Atmospheric Sciences*, 32, 1248
- Wallace, J. M., & Hobbs, P. V. 2006, *Atmospheric science: an introductory survey*, Vol. 92 (Elsevier)
- Wang, Y., Tian, F., Li, T., & Hu, Y. 2016, *Icarus*, 266, 15
- Way, M., & Del Genio, A. D. 2020, *Journal of Geophysical Research: Planets*, 125, e2019JE006276
- Way, M. J., Del Genio, A. D., Kiang, N. Y., et al. 2016, *Geophysical research letters*, 43, 8376
- Weiss, L. M., Marcy, G. W., Petigura, E. A., et al. 2018, *The Astronomical Journal*, 155, 48
- Welbanks, L., & Madhusudhan, N. 2019, *The Astronomical Journal*, 157, 206
- Wilson, H. F., & Militzer, B. 2011, *The Astrophysical Journal*, 745, 54
- Wolfgang, A., & Lopez, E. 2015, *The Astrophysical Journal*, 806, 183
- Youngblood, A., France, K., Loyd, R. P., et al. 2016, *The Astrophysical Journal*, 824, 101
- Yu, X., Moses, J. I., Fortney, J. J., & Zhang, X. 2021, How to identify exoplanet surfaces using atmospheric trace species in hydrogen-dominated atmospheres. <https://arxiv.org/abs/2104.09843>
- Yung, Y. L., Liang, M., Jiang, X., et al. 2009, *Journal of Geophysical Research: Planets*, 114
- Zahnle, K., Marley, M., Freedman, R. S., Lodders, K., & Fortney, J. 2009, *The Astrophysical Journal Letters*, 701, L20
- Zahnle, K., Marley, M. S., Morley, C. V., & Moses, J. I. 2016, *The Astrophysical Journal*, 824, 137
- Zahnle, K. J., & Kasting, J. F. 1986, *Icarus*, 68, 462
- Zahnle, K. J., Kasting, J. F., & Pollack, J. B. 1988, *Icarus*, 74, 62
- Zeng, L., Jacobsen, S. B., Sasselov, D. D., et al. 2019, *Proceedings of the National Academy of Sciences*, 116, 9723